MONTAN
UNIVERSITÄT
LEOBEN

Chair of Physical Chemistry

Doctoral Thesis

Influence of fundamental material properties on the oxygen exchange kinetics of the rare earth nickelate $La_2NiO_{4+\delta}$ for use as oxygen electrode in solid oxide electrolysis cells

Dipl.-Ing. Sarah Eisbacher-Lubensky, BSc

August 2024

MONTANUNIVERSITÄT LEOBEN
www.unileoben.ac.at

EIDESSTATTLICHE ERKLÄRUNG

Ich erkläre an Eides statt, dass ich diese Arbeit selbstständig verfasst, andere als die angegebenen Quellen und Hilfsmittel nicht benutzt, den Einsatz von generativen Methoden und Modellen der künstlichen Intelligenz vollständig und wahrheitsgetreu ausgewiesen habe, und mich auch sonst keiner unerlaubten Hilfsmittel bedient habe.

Ich erkläre, dass ich den Satzungsteil „Gute wissenschaftliche Praxis“ der Montanuniversität Leoben gelesen, verstanden und befolgt habe.

Weiters erkläre ich, dass die elektronische und gedruckte Version der eingereichten wissenschaftlichen Abschlussarbeit formal und inhaltlich identisch sind.

Datum 06.08.2024

Unterschrift Verfasser/in
Sarah Laura Eisbacher-Lubensky

ACKNOWLEDGMENTS

First of all, I would like to thank Prof. Dr. Edith Bucher for the opportunity to write my PhD-thesis at the Chair of Physical Chemistry at Montanuniversitaet Leoben. I would like to thank her for many helpful suggestions and advice.

In particular, I would like to thank Andreas Egger, who taught me everything from preparative work to measurement methodology. I would also like to take this opportunity to thank him for countless pieces of advice and for supporting me with his excellent knowledge.

I am grateful to Florian Schrenk for his support in carrying out the XPS-measurements.

I would like to thank my colleagues at the Chair of Physical Chemistry for support and assistance in my research, as well as for many discussions outside of research.

Finally, I would like to express my gratitude to my parents and my sister for tireless support and to Jan for always encouraging me and putting up with my moods, especially at times when progress was slow.

ABSTRACT

This thesis deals with the rare earth nickelate $La_2NiO_{4+\delta}$ (LNO) in terms of its fundamental material properties, with a particular focus on oxygen exchange kinetics and electrochemical characterization relevant for potential application as oxygen electrode in solid oxide electrolysis cells (SOECs). The impact of partial substitution of nickel with 10 % cobalt is evaluated, as well as the effect of surface modification by acid etching with HNO_3. The electronic conductivity and the chemical surface exchange coefficients are determined by dc-conductivity relaxation measurements on a bar-shaped sample. The substitution of nickel with cobalt in $La_2Ni_{0.9}Co_{0.1}O_{4+\delta}$ (LNCO291) leads to significantly higher surface exchange coefficients and a lower activation energy of the surface exchange reaction compared to LNO, while the electronic conductivity experiences a slight reduction. The conductivity relaxation measurements on the etched sample yield noteworthy results. The surface exchange coefficients of oxygen are increased and a further reduction in the activation energy compared to the unetched LNO and LNCO291 is achieved. It is observed that acid etching has no effect on the electrical conductivity. X-ray photoelectron spectroscopy (XPS) is employed to obtain comprehensive data on the surface chemistry. The findings indicate the formation of a nickel-depleted phase on the surface of the etched sample. Consequently, it can be inferred that La_2O_3 is the predominant phase on the surface.

Furthermore, the electrochemical properties of LNCO291 are examined through the use of current density-voltage (*I*-*V*) curves on an electrolyte-supported cell. The substitution of nickel with 10 % cobalt results in a slight enhancement in cell performance, thereby indicating that LNCO291 shows promising properties for use as an oxygen electrode material in SOECs. The impact of nickel and lanthanum oxide infiltration on symmetrical cells is examined using electrochemical impedance spectroscopy (EIS). The results suggest that nickel infiltration enhances the cell performance, whereas lanthanum infiltration shows the opposite effect. Post-test analyses using scanning electron microscopy (SEM) are carried out to confirm the porous microstructure of the electrodes and to characterize the cross-sections of the electrode-electrolyte interfaces of the cells, which confirm good adhesion between the layers.

KURZFASSUNG

In dieser Arbeit wird das Seltenerdnickelat $La_2NiO_{4+\delta}$ (LNO) in Hinblick auf grundlegende Materialeigenschaften untersucht, wobei der Schwerpunkt auf der Sauerstoffaustauschkinetik und der elektrochemischen Charakterisierung liegt, die für eine potenzielle Anwendung als Sauerstoffelektrode in Festoxidelektrolysezellen (SOECs) relevant sind. Die Auswirkung der teilweisen Substitution von Nickel durch Kobalt sowie die Auswirkung der Oberflächenbehandlung mit Säure (HNO_3) werden bewertet. Die elektronische Leitfähigkeit sowie der chemische Oberflächenaustauschkoeffizient von Sauerstoff werden durch Gleichstrom-Leitfähigkeitsrelaxationsmessungen an einer dichten Probe bestimmt. Die Ergebnisse zeigen, dass die Substitution von Nickel durch 10 % Kobalt in $La_2Ni_{0.9}Co_{0.1}O_{4+\delta}$ (LNCO291) im Vergleich zu LNO zu deutlich höheren Oberflächenaustauschkoeffizienten und einer niedrigeren Aktivierungsenergie der Oberflächenaustauschreaktion führt. Gleichzeitig lässt sich eine leichte Abnahme der elektronischen Leitfähigkeit feststellen. Die Leitfähigkeitsrelaxationsmessungen an der geätzten Probe liefern bemerkenswerte Ergebnisse. So wird eine Erhöhung der Oberflächenaustauschkoeffizienten für Sauerstoff beobachtet, während die Aktivierungsenergie der Oberflächenaustauschreaktion im Vergleich zur geätzten LNO-Probe und zu LNCO291 noch weiter gesenkt wird. Ein Einfluss des Ätzens mit Säure auf die elektrische Leitfähigkeit ist nicht festzustellen. Mittels Röntgen-Photoelektronenpektroskopie (XPS) wurden umfassende Daten zur Oberflächenchemie gewonnen. Die Ergebnisse deuten auf die Bildung einer nickelarmen Phase auf der Oberfläche der geätzten Probe hin. Daraus kann geschlossen werden, dass La_2O_3 die vorherrschende Phase auf der Oberfläche ist.

Des Weiteren werden die elektrochemischen Eigenschaften von LNCO291 anhand von Stromdichte-Spannungs-Kurven (*I*-*V*) in einer elektrolytgestützten Zelle untersucht. Die Substitution von Nickel durch 10 % Kobalt führt zu einer leichten Verbesserung der Zellleistung, was darauf hindeutet, dass LNCO291 vielversprechende Eigenschaften für den Einsatz als Sauerstoffelektrode in SOECs aufweist. Die Auswirkungen der Infiltration mit Nickel- bzw. Lanthanoxid auf symmetrische Zellen werden mittels elektrochemischer Impedanzspektroskopie (EIS) untersucht. Die Ergebnisse deuten darauf hin, dass die Nickelinfiltration die Zellleistung verbessert, während die Lanthaninfiltration den gegenteiligen Effekt zeigt. Post-Test-Analysen mittels Rasterelektronenmikroskopie (REM) werden durchgeführt, um die poröse Mikrostruktur der Elektroden zu bestätigen und die Querschnitte der Elektroden-Elektrolyt-Grenzflächen der Zellen zu charakterisieren. Auf diese Weise lässt sich eine gute Haftung zwischen den Schichten nachweisen.

Table of contents

1 SCOPE OF THE THESIS

The aim of this thesis is the development of novel oxygen electrode materials for solid oxide cells. The objective is to enhance the oxygen exchange kinetics of the rare earth nickelate $La_2NiO_{4+\delta}$ and to gain a profound comprehension of the mass and charge transport properties, in addition to the surface chemistry and electrochemical performance of this compound. *Chapter 2* introduces the working principle of solid oxide electrolysis cells and provides a detailed description of cell function and state-of-the-art materials. *Chapter 3* presents the theoretical background of the methods applied for the kinetic and electrochemical characterization of samples at the material and cell level. Finally, the structure and properties of $Ln_2NiO_{4+\delta}$ - type rare earth nickelates are described in this chapter. The procedures used for sample preparation, electrochemical characterization and post-test analysis are described in detail in *Chapter 4*. The results are then presented and discussed in *Chapter 5*. The first part deals with the research question:

I. How does the partial substitution of nickel with cobalt affect the oxygen exchange kinetics?

Cobalt is found only in a few regions of the world and is often mined under very problematic circumstances - environmentally harmful, dangerous, with child labor. Environmentalists and human rights activists criticize cobalt mining in the Democratic Republic of Congo, where the largest deposits of the rare raw material are located[1]. In light of these considerations, it became evident that a more comprehensive understanding of the potential alternatives to the substitution of A- and B-sites is necessary in order to enhance the oxygen exchange kinetics. The following research question is therefore posed:

II. Is it possible to improve the oxygen exchange kinetics without partial substitution - but with surface modification?

This is further analyzed in the section *5.2*. In the third sub-chapter, the electrochemical properties of the materials are investigated in order to test their suitability for use as oxygen electrodes in SOECs. A summary of the results and main conclusions of the studies are carried out and the answers to the research questions are presented in *Chapter 6*.

---

[1] https://www.amnesty.org/en/latest/news/2023/09/drc-cobalt-and-copper-mining-for-batteries-leading-to-human-rights-abuses/ in May 2024.

2 INTRODUCTION

Increasing energy consumption as a result of population growth in combination with limited supplies of fossil fuels (e.g. oil and gas) has led to an increase in the use of renewable energy sources. Much of the growing energy demand can be met by sustainable sources such as solar and wind power, but most of these are volatile, making storage necessary but also difficult. Electricity from renewable sources can rarely respond immediately to demand because, as mentioned above, these sources do not provide a regular supply that can be easily adjusted to meet consumption needs [1]. Therefore, flexible and highly efficient energy storage and conversion technologies are needed. In this respect, solid oxide cells (SOCs) could play an important role, as they are efficient chemical-to-electrical energy converters that can provide a useful link between energy production and demand. Hydrogen is considered as a potential fuel and energy carrier for these future energy technologies. One of the most efficient and sustainable technologies for converting electrical energy into hydrogen is based on high-temperature solid oxide electrolysis cells (SOEC) [2–5]. Unlike other electrolysis technologies, such as alkaline electrolysis, SOEC systems are not yet widespread. However, it should be noted that the successful establishment of these devices offers the possibility of storing electrical energy not only in the form of hydrogen, but also in the form of synthesis gas (i.e., a mixture of hydrogen and carbon monoxide), which in turn can be converted into lower hydrocarbons that could be distributed via the existing infrastructure.

The following sections provide a short overview of the function and materials used in solid oxide electrolysis cells.

2.1 Solid oxide electrolysis cell

Solid oxide electrolysis cells (SOECs) use electricity to split water vapor into hydrogen and oxygen. The water splitting reaction does not occur spontaneously and is a highly endothermic reaction. Therefore, it is advantageous to perform the electrolysis reaction at higher temperatures to reduce overvoltage. The typical operating temperature lies between 650 and 900 °C. The working principle of an SOEC is illustrated in *Figure 1*. However, SOECs not only convert water vapor into hydrogen, but can also operate on mixtures of water (H_2O) and carbon dioxide (CO_2), resulting in synthesis gas (H_2 + CO). This is particularly advantageous when waste water vapor and waste heat are available, as is the case in some high-temperature processes - such as the production of steel or cement, which are currently unavoidable sources of CO_2. Due to favorable reaction kinetics and thermodynamics, technical efficiencies close to 100 % can be achieved in SOEC mode [5–7].

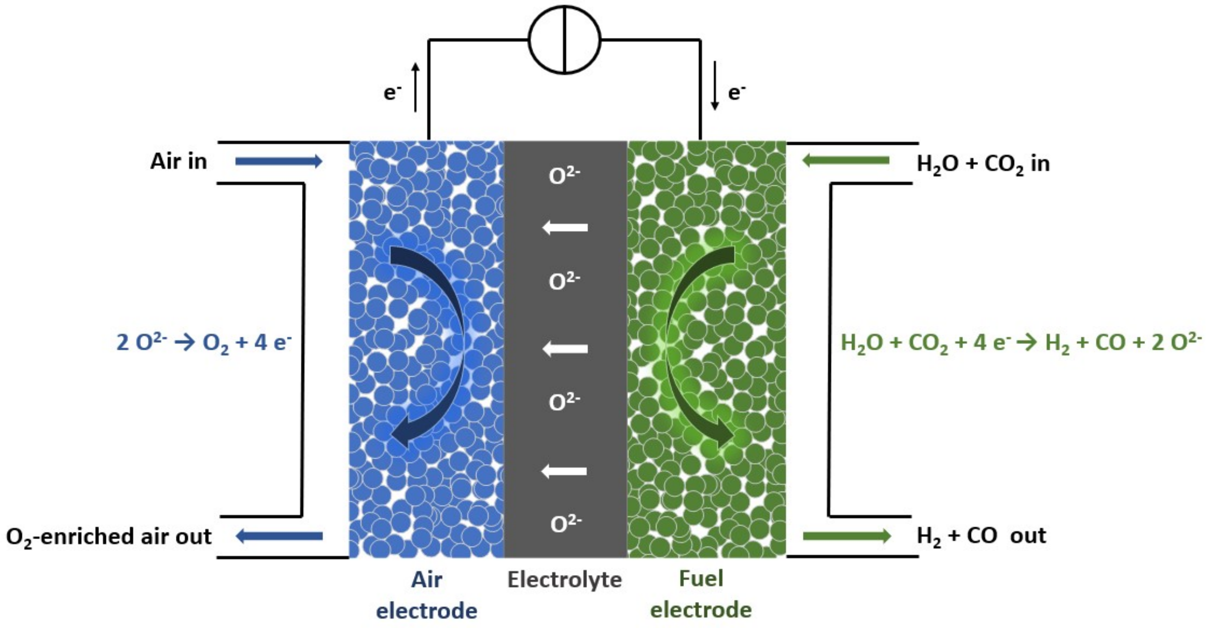

Figure 1 Working principle of a solid oxide electrolysis cell for a feed gas mixture of CO_2 and H_2O.

The chemical reactions occurring during H_2O- and CO_2- electrolysis are given below.

Fuel electrode	$H_2O + 2\,e^- \rightarrow H_2 + O^{2-}$	2.1
	$CO_2 + 2\,e^- \rightarrow CO + O^{2-}$	2.2
Oxygen electrode	$O^{2-} \rightarrow \frac{1}{2}O_2 + 2\,e^-$	2.3
Overall reactions	$H_2O \rightarrow H_2 + \frac{1}{2}O_2$	2.4
	$CO_2 \rightarrow CO + \frac{1}{2}O_2$	2.5

Two main cell configurations are used in solid oxide cells: the planar and the tubular type. Both configurations consist of the same main components, a dense ionically conducting electrolyte and two porous electrodes: air and fuel electrode. Tubular cells have high mechanical stability and good thermal cyclability. However, their use in SOECs is still in the development stage. Therefore, industrial applications have focused on planar cells as they achieve high power densities and are easier to manufacture, which in turn increases cost efficiency [6,8]. The cell design of planar cells depends on the supporting layer (self-supporting cells), which provides the required mechanical stability, as it is usually the thickest layer in the cell structure. The cells are therefore referred to as fuel electrode-, oxygen electrode-, and electrolyte-supported cells, as displayed in *Figure 2*. Alternatively, another support can also be used, such as metal-supported cells, which appear promising in terms of robustness and power density.

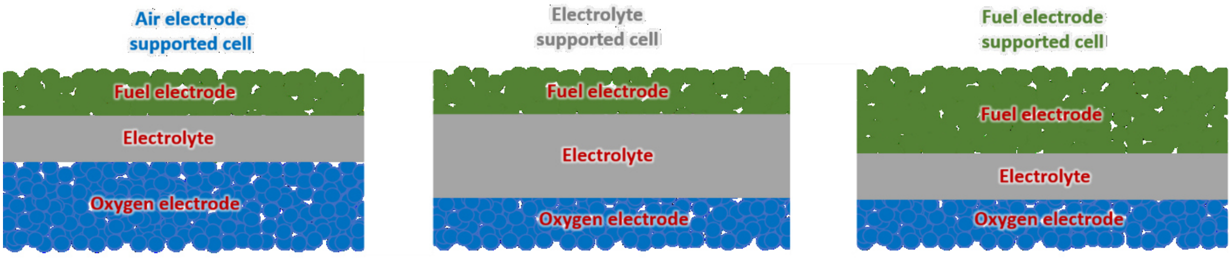

Figure 2 Design options of self-supported cells. The individual layer thicknesses are for schematic purposes only and do not represent actual thickness ratios.

Electrolyte-supported cells (ESCs) are particularly mechanically stable due to the dense electrolyte layer, which has a thickness of approximately 50 - 250 µm [9]. However, the thick electrolyte layer also results in high ohmic resistance, which in turn leads to lower power density and the requirement of high operating temperatures (above 800 °C) [6].

The mechanical stability of electrode-supported cells is ensured by the thick, porous electrode layer. Electrode-supported cells are divided into two types: fuel electrode-supported cells (FESCs) and oxygen electrode-supported cells (OESCs). The thickness of the electrode depends on the type of electrode-supported cell. FESCs have an active layer of 5 - 20 µm, while the active layer of OESCs ranges from 15 to 80 µm [9]. As a result, the electrolyte layer is much thinner (2 - 20 µm), which results in lower ohmic resistance and the ability to reduce the operating temperatures [9]. Due to high power densities - especially at lower temperatures - FESCs are often used nowadays [8]. Electrode-supported cells generally are known to exhibit a lower stability regarding re-oxidation, leading to a higher susceptibility to damage caused by redox cycling [6,10,11].

2.2 Materials for solid oxide electrolysis cells

Compared to other electrolysis technologies, the SOEC technology is not yet fully developed. One of the biggest challenges is the development of suitable materials, especially for the oxygen electrode. The state-of-the-art materials used in SOECs are described below.

2.2.1 Electrolyte

Since the electrolyte is the separator between the electrodes, it must be gas-tight and chemically stable with respect to reduction and oxidation processes. The performance of the electrolyte material clearly depends on temperature and layer thickness. In general, the electrolyte should have high oxide ion conductivity with negligible electronic conductivity to avoid potential leakage currents [6,12]. The electrolyte material - especially in electrolyte-supported cells - influences the thermal expansion of the entire cell and thermal expansion mismatch with the electrodes should therefore be avoided to prevent delamination [13]. The most commonly used electrolyte is yttria-stabilized zirconia. It is mainly used with 8 mol% Y_2O_3 (8YSZ) due to its good ionic conductivity and good mechanical properties. The use of less yttria makes the electrolyte more robust, but results in lower ionic conductivity [4,14]. The substitution of zirconia by yttria leads to an increase in oxygen vacancy concentration. This is shown in equation 1.6 in Kröger-Vink notation [15].

$$Y_2O_3 \xrightarrow{ZrO_2} 2\,Y_{Zr}' + 3\,O_O^{\times} + V_O^{\bullet\bullet} \qquad 2.6$$

Another electrolyte material with high ionic conductivity is doped ceria. The disadvantage of this material is that it can only be used at temperatures below 600 °C, because at higher temperatures and lower oxygen partial pressures, Ce^{4+} cations are reduced to Ce^{3+} cations, resulting in a partial electronic conductivity that is no longer negligible [16]. The substitution of ceria by gadolinia (CGO) as a dopant again leads to an increase in the concentration of oxygen vacancies. The reaction in Kröger-Vink notation is presented in equation 2.7.

$$Gd_2O_3 \xrightarrow{CeO_2} 2\,Gd'_{Ce} + 3\,O_O^{\times} + V_O^{\bullet\bullet} \qquad 2.7$$

Samarium-doped ceria (SDC) is also a good electrolyte, but again the partial electronic conductivity of cerium oxide leads to internal short circuits under the strongly reducing conditions of solid oxide electrolysis, so that this material appears unsuitable for use under typical SOEC operating conditions [17].

2.2.2 Fuel electrode

Fuel electrode materials provide reaction sites for the reduction reaction in an SOEC. In addition to good electronic and ionic conductivity, this task also requires sufficient porosity to ensure the transport of reactants and products to and from the active site of the electrode [16]. The materials must be thermally and mechanically stable and, with regard to chemical stability, the fuel electrodes must also be resistant to carbon deposits and reaction with sulfur impurities [16,18].

The selection of an appropriate fuel electrode depends on the fuel used in the SOEC. Metallic nickel has a high electrocatalytic activity for CO_2- and water vapor-electrolysis. However, it is only electronically conductive. If pure hydrogen is used as fuel, the electrode material Ni-YSZ, which is produced from NiO and YSZ particles, is used [4]. Here, nickel oxide is first reduced with hydrogen to Ni-metal, which leads to the formation of the necessary porosity. Nickel is then responsible for the electronic conductivity, but is also important as a catalyst for the oxidation of hydrogen [4,18]. In this composite, YSZ serves as a structural support and provides the necessary oxygen ion conductivity to ensure oxygen transport within the fuel electrode. Moreover, YSZ inhibits nickel grain growth, as otherwise the Ni particles would agglomerate, especially at higher temperatures [19]. In terms of mechanical stability, YSZ is responsible for good adhesion to the electrolyte [18]. However, Ni-YSZ fuel electrodes are not suitable for SOECs using carbon-containing fuels with relatively high oxygen partial pressures because nickel oxidizes when exposed to high concentrations of steam or CO_2 at higher operating temperatures. Nickel is also highly susceptible to carbon deposition, which has to be avoided, because the deposited carbon blocks the catalytically active sites of the fuel electrode [4]. To avoid the problem of carbon deposits, there are alternative fuel electrodes, such as lanthanum-substituted strontium vanadate (LSV) or lanthanum manganite substituted with strontium on the A-site and chromium on the B-site (LSCM). The latter one doped with 0.5 % Pd has already been successfully used in CO_2-electrolysis [4,20].

2.2.3 Oxygen electrode

Oxygen electrode materials provide the reaction sites for the oxidation in the SOEC. Oxygen electrodes should have high chemical, thermal and mechanical stability, as well as high oxygen ion conductivity and good electronic conductivity [2]. As with the fuel electrode, it is important to ensure that the coefficient of thermal expansion of the electrolyte material is similar to that of the oxygen electrode to prevent delamination [16]. The material should also be stable against impurities such as sulfur dioxide, chromium or silicon that come into contact with the material from other system components. These impurities reduce the long-term stability and oxygen surface exchange activity.

The standard oxygen electrode material $La_{1-x}Sr_xMnO_{3\pm\delta}$ (LSM) belongs to the family of perovskites. However, due to its low oxygen ion conductivity at temperatures below 800 °C, the material is too inactive for the oxygen reduction and is therefore only used as a composite electrode in conjunction with a good ion conductor such as YSZ [21]. This increases the triple phase boundary (TPB), where the oxygen electrode, electrolyte and gas phase meet [21,22]. For SOECs operating at low or intermediate temperatures (below 800 °C), it is crucial to have a long TPB since the reaction activity of the TPB significantly decreases with decreasing temperature [22]. Therefore, the use of materials with both ionic and electronic conductivity that effectively extend the TPB to the entire surface of the cathode is advantageous. Mixed ionic-electronic conductors (MIECs), such as $La_{1-x}Sr_xCoO_{3-\delta}$ (LSC), are considered as potential oxygen electrodes for the use in intermediate-temperature solid oxide electrolysis cells (IT-SOECs) [23,24]. The substitution of La^{3+} with Sr^{2+} in LSC leads to an improved oxygen ion- and electronic conductivity due to the formation of electron holes and oxygen vacancies [24]. However, LSC exhibits a large mismatch in thermal expansion coefficient (TEC) with most common electrolyte materials, which leads to delamination of the oxygen electrode [24]. Another potential oxygen electrode material is $La_{1-x}Sr_xFeO_{3-\delta}$ (LSF) [25,26], which has been proposed as a chemically more stable but less active alternative to LSC. Sr-substitution results in acceptor states that are compensated by oxygen vacancies or Fe^{4+} ions, which, similar to LSC, results in an increase in electronic and ionic conductivity [27]. A major advantage of LSF over LSC is a better TEC matching and a significantly lower reactivity with ZrO_2 [27]. Nevertheless, it should be noted that LSF incorporates Zr^{4+} ions into the B-site of the perovskite structure, resulting in an A-site deficient composition, which in turn has a lower electronic conductivity [27,28]. The A- and B-site substituted $La_{1-x}Sr_xCo_{1-y}Fe_yO_{3-\delta}$ (LSCF) has also been extensively investigated. This compound exhibits a lower TEC than LSC and shows lower reactivity with YSZ [16,29]. However, the B-site substitution of Co by Fe leads to a lower electronic conductivity, and the ionic conductivity decreases with increasing Fe-content [6,29].

At the present time, the state-of-the-art materials for oxygen electrodes are the MIEC oxides of the perovskite type. Many compounds with various compositions and A- and B-site substituents have been studied extensively [3,4,23,30,31].

Various studies [32–39] indicate that MIECs of the rare earth nickelate series $Ln_2NiO_{4+\delta}$ (Ln = La, Pr, Nd) exhibit fast oxygen exchange kinetics and reasonable electronic conductivity, making them a promising alternative to perovskites for use as oxygen electrodes in SOCs. Rare earth nickelates have a significant advantage over other materials due to the absence of alkaline earth substituents - such as strontium. These substituents cause long-term stability issues in perovskite-type oxygen electrodes due to surface segregation and reactions with critical impurities [38,40–44]. *Chapter 3.2* of this thesis provides a detailed description of the structure and properties of rare earth nickelates in relation to their application as oxygen electrodes in SOECs.

3 THEORETICAL BACKGROUND

This chapter discusses key aspects of the theoretical background relevant to the research in this thesis.

3.1 Electrical, kinetic and electrochemical characterization of oxygen electrode materials

3.1.1 Electrical conductivity measurements

Electrical dc-conductivity measurements in four-point geometry were used to investigate the electrical and kinetic properties of the dense bar-shaped samples, see *Figure 3*.

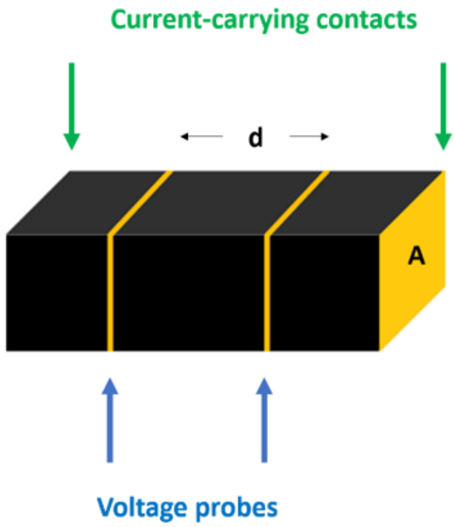

Figure 3 Linear four-point geometry of a dense bar-shaped sample, where d represents the distance between the voltage probes and A stands for the area of the current-carrying contacts.

The two outer contacts are used to apply a constant current, while the other two contacts serve as current-less voltage probes. In the present thesis, the contacts are made from Au wires and Au paste, as gold is inactive in the oxygen exchange reaction.

For the linear four-point technique, the dense ceramic sample must be prepared in the form of a rectangular rod, as shown in *Figure 3*. The current-carrying contacts are attached to the front faces, while the voltage probes are placed between them at a sufficient distance from the current-carrying contacts around the circumference of the sample. This is particularly important to minimize errors due to compositional inhomogeneities that can be caused by direct currents in mixed ionic-electronic conductors when using purely electronic contacts, also known as polarization. In addition, care must be taken to maintain a sufficiently large distance between the voltage probes in order to obtain a measurable voltage signal. In order to fulfill both requirements, Dudley and Steele [45] established the rule of placing the voltage probes symmetrically at one third of the bar length.

The electrical conductivity can be determined from the relation:

$$\sigma_\mathrm{e} = \frac{1}{R}\frac{d}{A} \tag{3.1}$$

R corresponds to the measured resistance, *d* is the distance of the voltage probes and *A* represents the cross section of the bar-shaped sample (see *Figure 3*). The resistance is obtained by measuring several voltages at various currents and *R* is calculated from the slope of the regression line to the *V* - *I* data points according to Ohm's law:

$$R = \frac{V}{I} \tag{3.2}$$

with *V* being the potential difference measured between the voltage probes and *I* being the applied current.

3.1.2 Electrical conductivity relaxation measurements

In this work, the in-situ dc-conductivity relaxation method is used to determine the oxygen exchange kinetics in dense ceramic samples. The method was first described by Dünwald and Wagner [46]. For this purpose, the samples are equilibrated in a quartz glass reactor with the surrounding atmosphere at a specific oxygen partial pressure and defined temperature. During the measurement, the electrical conductivity is recorded as a function of time according to the linear four-point geometry. The oxygen partial pressure is changed abruptly once the conductivity has reached an equilibrium state. This leads to oxygen incorporation or release into or from the material, depending on the direction of the oxygen partial pressure change in the gas flow (oxidation or reduction reaction). The electronic conductivity of the sample is a function of the oxygen content, so that the process leads to a relaxation towards the new equilibrium state. Comparing the abrupt change in the oxygen partial pressure with the change in conductivity, it can be seen that there is a delay while the sample relaxes towards equilibrium. *Figure 4* shows an oxidative pO_2-step (left) and the corresponding normalized conductivity response (right).

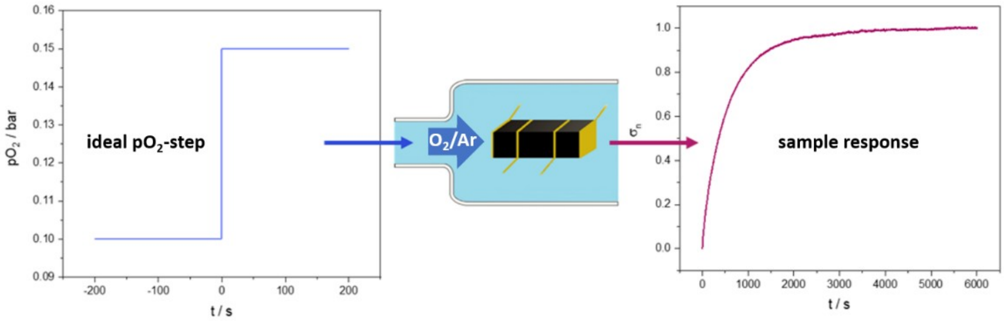

Figure 4 Schematic representation of the dc-conductivity relaxation method. The ideal change in oxygen partial pressure around an equilibrated sample (left) is considered as system input while the sample response (right) corresponds to the normalized change in electrical conductivity.

According to the following formula the conductivity response can be normalized:

$$\sigma_n = \frac{\sigma(t) - \sigma_0}{\sigma_\infty - \sigma_0} \qquad 3.3$$

where σ_0 corresponds to the measured conductivity before the relaxation reaction and σ_∞ represents the measured conductivity after the relaxation reaction.

The kinetic parameters, chemical surface exchange coefficient (k_{chem}) and chemical diffusion coefficient (D_{chem}) of oxygen, are obtained by nonlinear least-squares fitting of a suitable solution of the diffusion equation to the normalized conductivity transients. The solution of the diffusion equation depends on the sample geometry. In the linear four-point geometry, the oxygen can diffuse through the sample in two directions, as the two end faces of the bar-shaped samples are completely covered by gold sheets, which block the oxygen diffusion in this direction (see *Figure 5*).

Compared to other sample geometries, the bar-shaped sample is easy to prepare and allows the simultaneous determination of k_{chem} and D_{chem} under certain conditions.

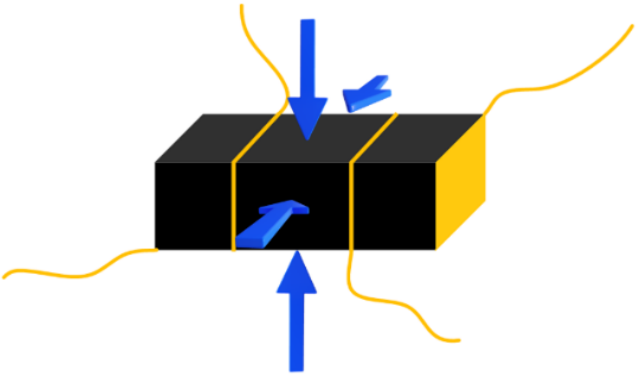

Figure 5 Oxygen diffusion pathways (blue arrows) through a bar-shaped sample with electrical contacts (gold).

Oxygen incorporation from the gas phase into the dense ceramic sample (and *vice versa* oxygen release) proceed by two serially connected processes: (a) the oxygen exchange between the gas phase and the sample surface (surface exchange) and (b) the diffusion of oxygen ions within the sample (chemical diffusion). In case of chemical diffusion, it can be described by Fick's first law for 1-dimensional diffusion:

$$J = -D_{\mathrm{chem}} \frac{\partial c}{\partial x} \qquad 3.4$$

where J corresponds to the oxygen flux density and $\frac{\partial c}{\partial x}$ to the concentration gradient of the oxygen ions.

Fick's second law of diffusion is obtained by inserting *Equation 3.4* into the continuity equation, whereby D_{chem} is regarded as constant.

$$\frac{\partial c}{\partial t} = D_{\mathrm{chem}} \frac{\partial^2 c}{\partial x^2} \qquad 3.5$$

Mosleh et al. [47] describe several elementary steps of the oxygen exchange process, such as the adsorption of molecular oxygen from the gas phase on the sample surface, dissociation, as well as reduction and incorporation into the material. These mechanisms are less well known than those for diffusion, as is the rate-determining step, which can differ from material to material and is also dependent on oxygen partial pressure and temperature [48].

Therefore, the surface exchange process is represented by a linear rate law:

$$J = k_{\mathrm{chem}} \left(c_s(t) - c_\infty \right) \tag{3.6}$$

Here c_s corresponds to the time-dependent oxygen concentration and c_∞ is the equilibrium concentration of oxygen after the relaxation process. *Equation 3.6* only holds true for small changes in the oxygen partial pressure.

As both processes (surface exchange and diffusion) are occurring in series, limited kinetics of one process result in this process dominating the overall kinetics - it becomes rate-determining. This means that no further information about the faster step can be obtained from the measurement. The entire relaxation process can therefore be divided into three different regimes, referred to as surface-controlled, diffusion-controlled and mixed-controlled. In order to distinguish between diffusion, surface and mixed-controlled kinetics, Bouwmeester et al. [49] introduced a characteristic thickness L_c for a steady-state oxygen flow through ceramics:

$$L_c = \frac{D}{k} \tag{3.7}$$

where D and k represent the self-diffusion coefficient and the surface exchange coefficient of oxygen, respectively. This characteristic parameter was transferred to oxygen relaxation measurements using the chemical surface exchange and diffusion coefficient by den Otter et al. [50]:

$$L_c = \frac{D_{\mathrm{chem}}}{k_{\mathrm{chem}}} \tag{3.8}$$

Quantitative criteria for the transition between the different regimes can be derived from the following relationship:

$$\frac{a}{L_c} = \frac{k_{\mathrm{chem}}\, a}{D_{\mathrm{chem}}} \tag{3.9}$$

with a as the total sample thickness L or half the sample thickness $L/2$. This depends on whether the oxygen exchange takes place from one side of the sample or via the two opposite sides.

Den Otter et al. [50] provides guidelines that indicate the dominant process. With a/L_c between 0.03 and 30, the oxygen kinetics are subject to mixed control, below 0.03 the kinetics are dominated by the surface exchange, and above 30 the kinetics are in the diffusion-controlled regime.

3.1.3 Current-voltage measurements

The cell performance of SOECs can be described via the current-voltage (*I*-*V*) curves. Frequently, the current or current density is plotted in the negative x-direction of the graphs because current is supplied to the cell during electrolysis. The cell performance is evaluated based on the deviation from the theoretical Nernst potential and can be increased by increasing the current density. A reduced cell potential increases the efficiency of the electrolysis process [51]. The following figure shows a schematic representation of an *I-V* curve of an SOEC.

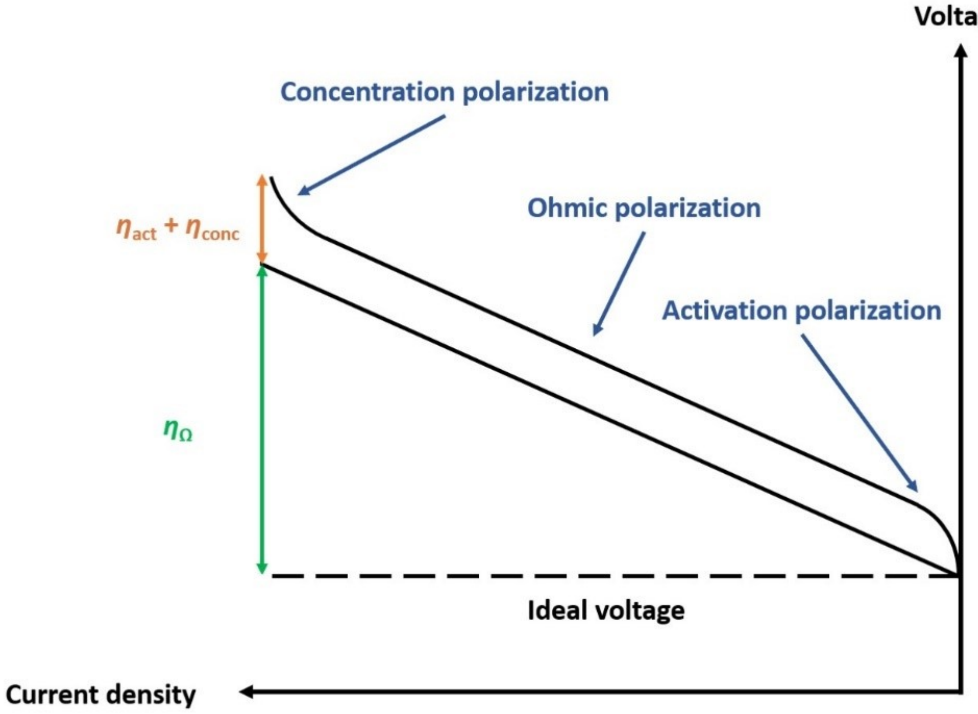

Figure 6 Schematics of I-V-curve of an SOEC.

The deviations from the ideal potential are due to polarization losses. The *I-V* curve can be described as follows [52]:

$$V = E^0 + \eta_{\Omega} + \eta_{\mathrm{act,oe}} + \eta_{\mathrm{conc,oe}} + \eta_{\mathrm{act,fe}} + \eta_{\mathrm{conc,fe}} \qquad 3.10$$

where E^0 represents the theoretical Nernst potential and V the measured voltage. η_{act}, η_{conc} and η_{Ω} are activation, concentration and ohmic losses of the oxygen and fuel electrode as well as the electrolyte.

3.1.3.1 Activation polarization

To enable the flow of ions and electrons, energetic barriers must be overcome, which are due to the inertia of the electrode kinetics. The activation polarization is therefore influenced by the kinetics of the electrochemical reactions at both electrodes. The term is derived from the activation energy that must be overcome by the reactants at the electrodes for the electrochemical reactions to take place. The slowest process, which takes place at the oxygen electrode or at the fuel electrode, determines the speed of the overall kinetics [53,54].

3.1.3.2 Concentration polarization

Concentration polarization is also referred to as gas transport loss, as the gaseous reactants supplied during the electrochemical reaction are consumed at the electrodes, resulting in a concentration gradient and a loss of potential. Concentration polarization can also occur if the gaseous products cannot diffuse away quickly enough [53].

3.1.3.3 Ohmic polarization

Ohmic resistances occur due to restrictions in the flow of electrons and ions at the electrolyte, the electrodes and at various interfaces of the cell. On the stack level, other components such as the current collectors also contribute to the ohmic resistance of an SOEC. Ohmic polarization dominates in the medium current density range and is mainly due to the limited ionic conductivity of the electrolyte [51,53].

3.1.4 Electrochemical impedance spectroscopy

Electrochemical impedance spectroscopy (EIS) is a characterization tool that enables the investigation of electrode processes and transport properties of materials [55]. This method makes it possible to separate the influences of different processes in the overall resistance in a solid oxide cell.

3.1.4.1 Definition of impedance

The equations in this chapter concerning the EIS are taken from reference [56]. The resistance R of a system results when a current I, which is applied to obtain a certain voltage V, is conducted through the system. This process is described using Ohm's law (see *Equation 3.2*). This law is only valid if voltage and current are in phase, as it is the case with an ideal resistor. By considering the geometry of the sample, the resistance can be defined as follows:

$$R = \rho \, \frac{d}{A} \tag{3.11}$$

where ρ represents the resistivity, d is the thickness and A the area of the sample. The specific conductivity σ is in turn defined as the reciprocal of the resistivity. The impedance Z represents the relationship between voltage and current for alternating currents (ac), also capturing the phase shift between the input voltage and the resulting current. Experimentally, an ac-voltage with a certain amplitude is applied at different frequencies when measuring impedance spectra. The voltage signal $V(t)$ is time-dependent and is represented mathematically as follows:

$$V(t) = V_a \sin(\omega \, t) \tag{3.12}$$

with V_a as voltage amplitude, t as time and ω as the angular frequency, which is related to the frequency f by:

$$\omega = 2 \, \pi \, f \tag{3.13}$$

For linear systems, the resulting current output I(t) is also sinusoidal at the same frequency with amplitude I_a, but now includes a phase shift φ:

$$I(t) = I_a \sin(\omega \, t - \varphi) \tag{3.14}$$

Both the applied voltage and the current output are illustrated in *Figure 7*.

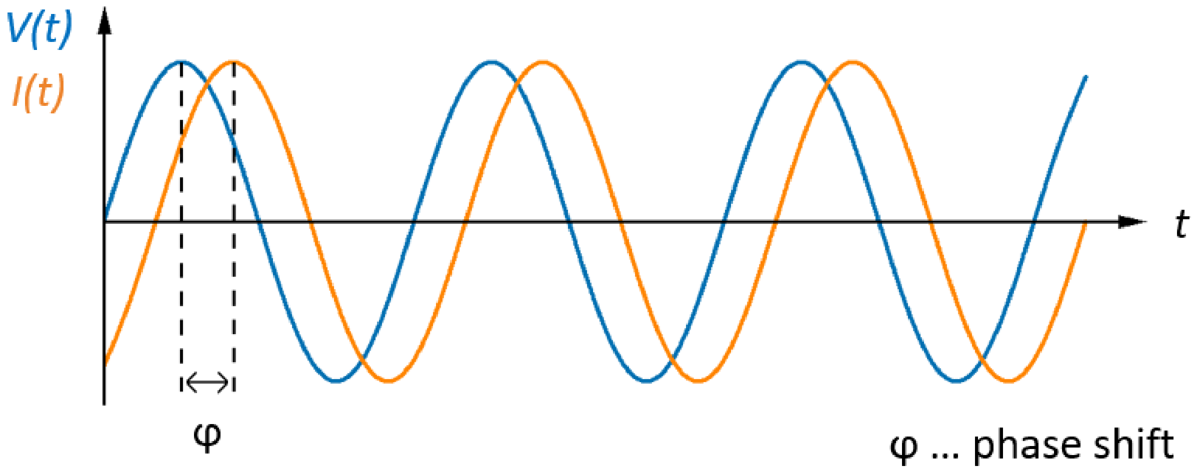

Figure 7 Representation of the phase shift φ in EIS. The blue curve illustrates the applied voltage V(t) and the orange curve the current output I(t).

The combination of Ohm's law and *Equations 2.13* and *2.15* leads to the expression of the impedance *Z*:

$$Z = \frac{V(t)}{I(t)} = \frac{V_a \sin(\omega t)}{I_a \sin(\omega t - \varphi)} \tag{3.15}$$

For a simpler treatment of time-dependent sinusoids, it is advantageous for the further mathematical description of the ac resistance to switch to the complex number plane by using Euler's relationship:

$$e^{j\varphi} = \cos\varphi + j\sin\varphi \tag{3.16}$$

and write:

$$Z = \frac{V(t)}{I(t)} = \frac{V_a\, e^{j\omega t}}{I_a\, e^{j(\omega t - \varphi)}} = Z_a e^{j\varphi} \tag{3.17}$$

with *Z* = *Z'* + *j Z''*, where Z' is the real part and Z'' denotes the imaginary part of the complex impedance. The real part represents the resistance to a Faradaic current flowing through a circuit, and the imaginary part describes the ability to store electrical energy capacitively or inductively.

3.1.4.2 Interpretation of impedance spectra

In order to interpret the electrochemical characteristics of SOECs, impedance measurements are carried out in the frequency range *f* from MHz to mHz. *Figure 8* illustrates the Nyquist plot that represents the impedance data in the complex plane. More precisely, the impedance *Z* is shown as a vector in the complex plane with *Z'* and *Z''* as Cartesian coordinates or, alternatively, in polar coordinates with the magnitude Z_a and the phase angle φ according to:

$$Z_a = \sqrt{Z'^2 + Z''^2} \qquad \varphi = \arctan\frac{Z''}{Z'} \qquad 3.18$$

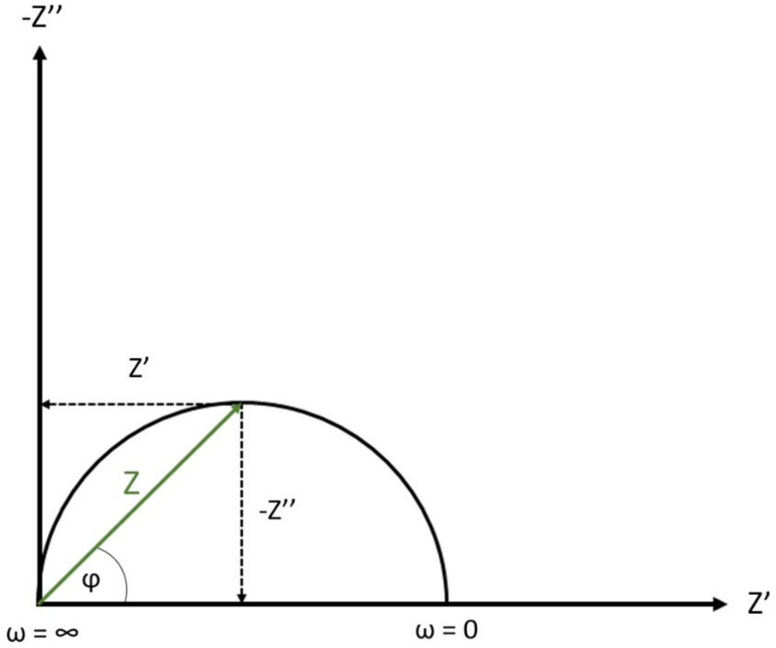

Figure 8 Nyquist plot of impedance data with Z in a complex plane with Z' and Z'' as coordinates, the phase angle φ and the angular frequency range ω.

Electrochemical impedance spectra are often interpreted using models based on equivalent electrical circuits. These consist of the main passive elements' resistor, capacitor and inductor as well as various other elements describing different electrochemical situations and processes (*CPE*, Warburg, Gerischer etc.). It is necessary to choose the elements carefully so that the best possible agreement with the measured data can be achieved, while representing physically meaningful processes that take place in the analyzed system. The following equations (*Equation 3.19* to *Equation 3.21*) state the explicit impedances of RCL elements:

$$Z_R = R \tag{3.19}$$

$$Z_C = \frac{1}{j\,\omega\,C} = -\,\frac{j}{\omega\,C} \tag{3.20}$$

$$Z_L = j\,\omega\,L \tag{3.21}$$

where *R* is the resistance, *C* is the capacitance and *L* the inductance.

3.2 K_2NiF_4 - type rare earth nickelates

The structure and composition of $Ln_2NiO_{4+\delta}$ - type rare earth nickelates are described in more detail in the following two subsections.

3.2.1 Crystal structure and defect chemistry

Rare earth nickelates belong to the Ruddlesden-Popper (RP) series, comprising perovskite-related layered compounds with the general formula $A_{n+1}B_nO_{3n+1}$ [57,58]. The A-site is generally occupied by lanthanide or alkaline earth ions. The B-site is occupied by a (3d) transition metal ion. The perovskite layers in the crystal structure of rare earth nickelates are stacked along the crystallographic c-axis. In order to prevent coulombic repulsion between ions with the same charge, the perovskite layers are shifted in-plane along the a- and b-direction. This means that the cations and anions of two neighboring layers face each other. The arrangement of the ions between two consecutive perovskite layers corresponds to the rock salt structure. While perovskite structures are characterized by their dense packing and therefore offer relatively little space for oxygen on interstitial sites, rock salt layers are less densely packed and can more easily incorporate interstitial oxygen [54]. The stacked layers can not only consist of single perovskite layers, but also of double and triple layers. These members of the Ruddlesden-Popper series are distinguished by the number (n) of perovskite layers that make up the perovskite blocks of the structure, which are presented in *Figure 9*.

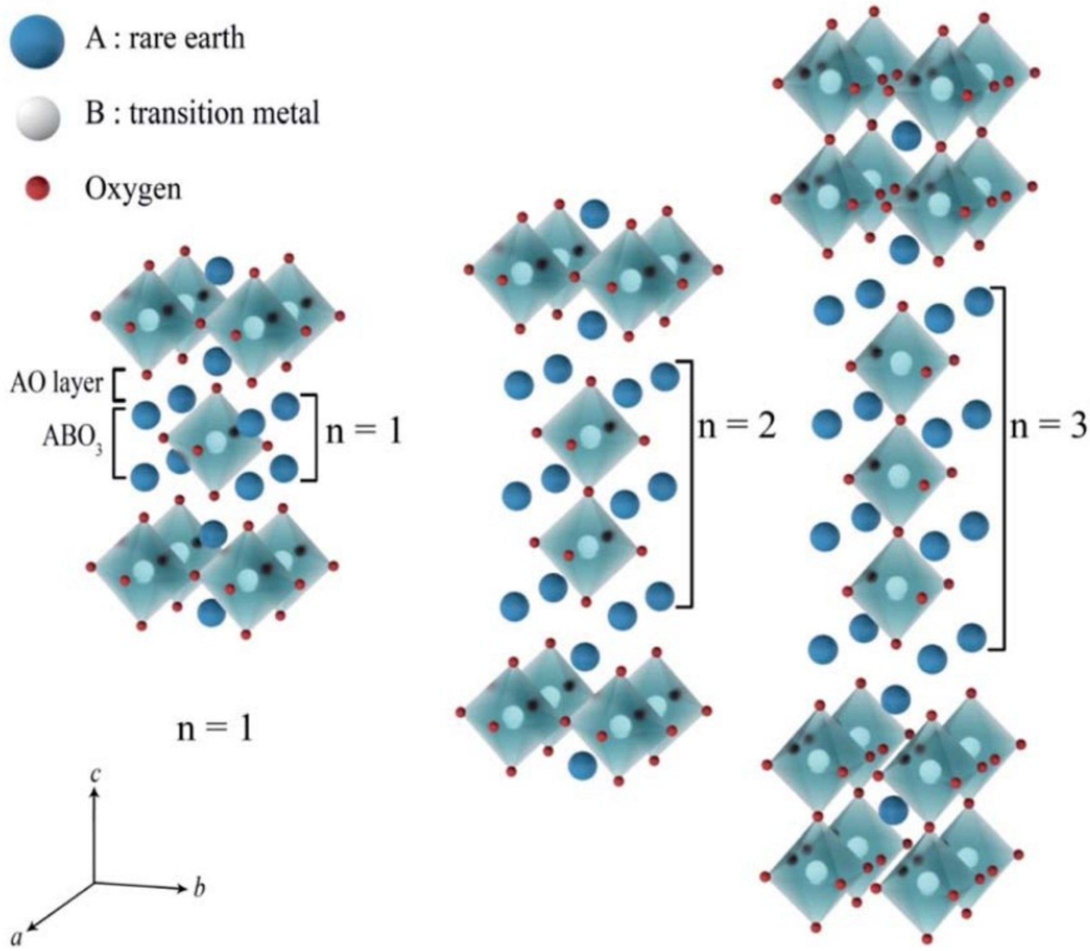

Figure 9 Representation of crystal structures of the first-order (n=1), second-order (n=2) and third-order (n=3) Ruddlesden-Popper phases [59].

The first member of the RP-series crystallizes in the K_2NiF_4-type structure [18,59,60]. The second and third members of the higher RP homologues were discovered in the Sr titanate system by Ruddlesden and Popper and published as crystal structures of $Sr_3Ti_2O_7$ (n = 2) and $Sr_4Ti_3O_{10}$ (n = 3) [57,61].

Rare earth nickelates have different oxygen content in the crystal lattice. This oxygen non-stoichiometry is denoted as δ in the chemical formula $La_2NiO_{4+\delta}$. The absolute value of δ depends on the order of the RP phase and its chemical composition, as well as on the temperature and the oxygen partial pressure. $La_2NiO_{4+\delta}$, $Pr_2NiO_{4+\delta}$ and $Nd_2NiO_{4+\delta}$ are hyperstoichiometric compounds in which δ-values in the range of $0 \leq \delta \leq 0.25$-0.30 are tolerated. The oxygen excess is generated by oxygen incorporation on the interstitial sites of the loosely packed rock salt layers [54,59]. The stability of the A_2BO_4 - phases between the perovskite and rock salt layers can be determined from the ionic radii using the Goldschmidt tolerance factor *t*

$$t = \frac{r_{Ln} + r_O}{\sqrt{2}\,(r_{Ni} + r_O)} \tag{3.22}$$

where r_{Ln}, r_{Ni} and r_O are the ionic radii of Ln^{3+}, Ni^{2+} and O^{2-} - ions, respectively [59]. For the ideal tetragonal structure $t = 1$, but tetragonal K_2NiF_4-type structures in the range $0.85 < t < 1$ are generally considered stable. The tolerance factor of the stoichiometric compound $La_2NiO_{4+\delta}$ ranges between 0.87 and 0.89, which shows that the La-O bonds in the compound are under tensile stress and the Ni-O bonds are under compressive stress [59,62]. Due to the lanthanide contraction only cations of the early rare earth elements lanthanum, praseodymium and neodymium can form undoped Ruddlesden-Popper-type nickelates. Tamura et al. [63] report that $La_2NiO_{4+\delta}$ has a tetragonal crystal structure with space group *I*4/*mmm* at elevated temperatures and oxygen interstitials are located at the $(\frac{1}{4}, \frac{1}{4}, \frac{1}{4})$ sites of the crystal lattice (see *Figure 10*) [59,64].

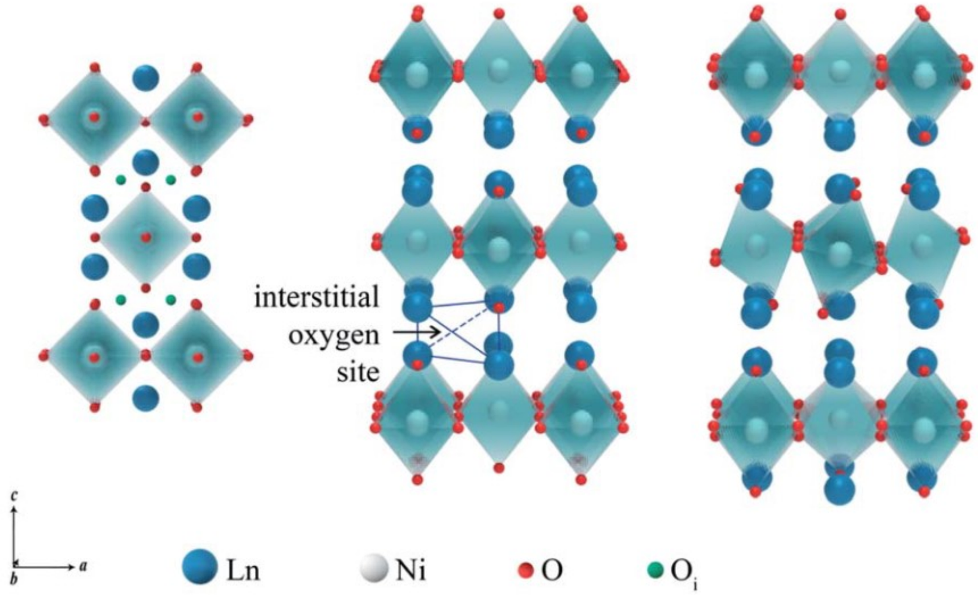

Figure 10 Crystal structures of $Ln_2NiO_{4+\delta}$ (Ln = La, Pr and Nd) phases with orthorhombic (right) and tetragonal (center) lattice symmetry. The a-c projection of the tetragonal lattice on the left illustrates the positions of the interstitial oxygen ions (green colored) [59].

Among others, Aspera et al. [65] describe that a phase transition from tetragonal to orthorhombic can also take place and consider the increase in the concentration of interstitial oxygen in LnO-layers of the rock salt type as an important factor for the structural change. The tilting of the octahedra is caused by interstitial oxygen ions repelling neighboring apical oxygen ions in the perovskite layers. The difference in size of the ionic radii of possible A-site cations for nickelates (La > Pr > Nd) leads to an increase in oxygen excess. As a result, stresses in the structures are equalized and a possible transition from an orthorhombic to a tetragonal structure is shifted towards higher temperatures [59,66].

In addition to oxide ions on interstitial sites, oxygen vacancies in the perovskite layers of Ruddlesden-Popper phases also influence the oxygen transport [59]. Oxygen vacancies are formed as a consequence of modifications in the composition of the cations in RP-phases or in the form of Frenkel defects, as illustrated in *Equation 3.23* in Kröger-Vink notation [15,59].

$$O_O^{\times} \rightleftharpoons V_O^{\bullet\bullet} + O_i'' \tag{3.23}$$

3.2.2 A- and B-site substitution

Since the crystal structure of Ruddlesden-Popper-type compounds A_2BO_4 is – within certain limits – flexible in terms of chemical stability, substitutions can be made in both sublattices A and B. The partial substitution of Ln (A-site) and/or Ni (B-site) by alkaline earth or transition metals, respectively, can strongly influence the structural properties as well as the ionic and electronic conductivity, but also the electrocatalytic activity and the oxygen non-stoichiometry [59].

As already mentioned above, the A-site can tolerate a certain amount of cation vacancies, the early Ln-elements (La, Pr and Nd) can be substituted with each other (e.g. $La_{2-x}Pr_xNiO_{4+\delta}$) or be replaced by alkaline earth metal ions (e.g. $Ln_{2-x}A_xNiO_{4+\delta}$ with A = Ca, Sr and/or Ba). In particular, the substitution on the B-site with cations of the 3d transition metals Co, Cu, Fe, Mn and others has already been investigated [37,39,54,59,67–69]. In the context of this work, the substitution of nickel on the B-site by cobalt was carried out, and therefore only this will be discussed in more detail here.

It is interesting to note that doping perovskites with Co results in higher electronic conductivity and higher catalytic activity, but perovskites exhibit an increase in TEC associated with Co doping, which is disadvantageous in terms of application. In the case of rare earth nickelates, however, partial substitution of Ni with Co sometimes has the opposite effect. For example, the electronic conductivity decreases with Co substitution, although the oxygen over-stoichiometry increases [67,68]. This is explained in the literature [54] as follows: Co-doping in nickelates leads to a decrease in the mobility of the electron holes with a simultaneous increase in their concentration towards higher oxygen over-stoichiometries. This could lead to significant differences in the relationship between conductivity and temperature, since both - the mobility of the charge carriers as well as the oxygen content - are temperature-dependent. The catalytic activity for the reduction or oxidation of oxygen also increases with increasing Co-content. For example, we observed in our previous study [39] an increase in the oxygen surface exchange coefficient accompanied by halving its activation energy when doping $La_2NiO_{4+\delta}$ with 10 % Co. In general, transition metal ions often form higher oxidation states in oxide compounds under oxidizing conditions. As a result, they exhibit limited solubility in the nickelate lattice in $La_2NiO_{4+\delta}$. For example, for cobalt in $La_2Ni_{1-y}Co_yO_{4+\delta}$, Amow et al. [70] determined a maximum solubility of y = 0.2. The electroneutrality condition for the substitution of nickel by cobalt can be described by the following formula in Kröger-Vink notation [59]:

$$[Ni_{Ni}^{\bullet}] + [Co_{Ni}^{\bullet}] = 2\,[O_i''] \tag{3.24}$$

3.2.3 Surface chemistry

The mechanisms of ionic conduction and oxygen bulk diffusion in $Ln_2NiO_{4+\delta}$ - type rare earth nickelates are well understood [71–73]. However, the surface crystal structure and its chemistry are still not explored in detail. The surface structure has a major influence on the surface exchange of oxygen, which subsequently influences the overall rate of oxygen incorporation and migration. Investigations of similar RP-materials, including $La_2NiO_{4+\delta}$, $La_{2-x}Sr_xNiO_{4+\delta}$ and $La_{2-x}Pr_xNiO_{4+\delta}$, have shown that these surfaces are terminated by A-site cations, with no nickel observed on the surface [74–76]. Surface characterizations of $La_2NiO_{4+\delta}$, therefore, indicate that the conventional mechanism of oxygen reduction, which requires the adsorption of oxygen atoms at the Ni sites of the surface, may not be possible. It is hypothesized that partial decomposition of $La_2NiO_{4+\delta}$ into perovskite-type $LaNiO_3$, and the higher order RP-phases $La_3Ni_2O_7$ and $La_4Ni_3O_{10}$ occurs on the surface when the material is exposed to air. Wu et al. [72] propose that the decomposition process results in a stacking of the following phases between 600 and 800 °C: (La_2O_3)-($La_3Ni_2O_7$/$La_4Ni_3O_{10}$)-(La_2NiO_4), with the stacking occurring from the surface inwards to bulk. It is hypothesized that this stacking could be responsible for the absence of nickel on the surface and the presence of a La-rich surface layer, which shows a high activation energy for diffusion. Furthermore, the literature [77] also states that in $La_2NiO_{4+\delta}$ - thin films La- and O-enrichment at the surface is followed by a Ni-rich subsurface region, see *Figure 11*.

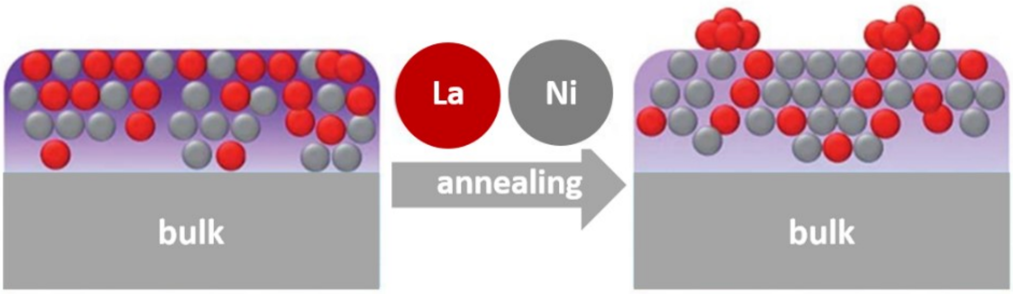

Figure 11 Illustration of the surface composition of a $La_2NiO_{4+\delta}$ *- thin film adapted from reference [77].*

However, the details of the decomposition reaction kinetics remain unclear and need to be studied in more detail. In the context of its use as an oxygen electrode in SOCs, it can be concluded that the La-rich surface should be regarded as the relevant surface for oxygen exchange, rather than the ideal $La_2NiO_{4+\delta}$ surface.

4 EXPERIMENTAL

This chapter provides a detailed description of powder preparation and the process of preparing dense ceramic samples as well as the production of an electrolyte-supported cell (ESC) and symmetrical cells for cell tests. Methods for characterizing the raw materials and the tested samples are also described. Parts of this chapter have already been published in Eisbacher-Lubensky et al. [39].

4.1 Material preparation

The LNO and LNCO291 powders were synthesized using the citric acid-ethylene diaminetetraacetate (EDTA) sol-gel method. Stoichiometric amounts of the metal nitrates $La(NO_3)_3 \cdot 6\,H_2O$, $Ni(NO_3)_2 \cdot 6\,H_2O$ and in case of LNCO291 $Co(NO_3)_2 \cdot 6\,H_2O$ (all chemicals with analytical grade quality purchased from Merck KGaA) were mixed with deionized H_2O in a stainless-steel vessel. After dissolution of the metal nitrates, anhydrous citric acid and EDTA were added. Then, a 25 % aqueous ammonia-solution (NH_3) was used to adjust the pH to 8. Once a clear blue solution was obtained, the temperature was gradually increased to evaporate water and form a gel until self-ignition occurred. The resulting raw ash was crushed in an agate mortar and calcined at 1200 °C for 8 hours in air with heating and cooling rates of 5 K min^{-1}.

4.2 Material characterization

4.2.1 Particle size distribution

The particle size distribution of the LNO and LNCO291 powders was determined using a CILAS 1064 laser diffractometer equipped with a liquid dispersion unit. For this purpose, a suspension of 0.2 g of the powder in 25 ml deionized H_2O was mixed with 0.2 g Na-polyacrylate (NPA 2100, MW = 2100 g mol^{-1}), which acted as a dispersant, and sonicated for 5 minutes with an ultrasonic rod (amplitude: 60 % / cycle: 0.5 s). Approximately 0.5 g of the dispersant were dissolved in deionized H_2O in the liquid dispersing unit and circulated through the measuring cell. A background correction was applied to the resulting solvent dispersion. The measuring was performed using ultrasonic stirring. The mean particle size employed in the production of bar-shaped samples was 3.0 – 4.0 µm, whereas a mean particle size between 0.5 and 0.7 µm was used for the manufacture of screen-printing pastes.

4.2.2 X-ray diffraction

The calcined LNO and LNCO291 powders were analyzed using X-ray diffraction (XRD) at room temperature with a powder diffractometer (model D8 Advance, Bruker AXS) that employed Cu-Kα radiation in the range of 10° ≤ 2θ ≤ 100° with a resolution of 0.020° per step (2θ). The radiation source was operated at 40 kV and 25 mA. During measurement, the powder sample was rotated at 30 rpm. The diffraction pattern was evaluated using the commercial crystallographic PDF-4+ database (ICDD) and the integrated software SIeve+. Structural analysis was conducted using the software package TOPAS (Bruker AXS) through Rietveld refinement [78].

4.2.3 Thermal expansion

The thermal expansion of LNCO291 was measured using a push rod dilatometer (model DIL 402/PC4, Netzsch) with Al_2O_3 as reference material. Measurements were taken in the temperature range from 30 to 1000 °C with heating rates of 1 K min^{-1} and in the oxygen partial pressure range of $0.001 \leq pO_2$ / bar ≤ 0.1. Different atmospheres were obtained using O_2-Ar gas mixtures with mass flow controllers at flow rates of 10 L h^{-1}.

4.3 Conductivity and conductivity relaxation measurements

4.3.1 Preparation of a densely sintered sample

To obtain dense bar-shaped samples of LNO and LNCO291, the powders were isostatically pressed into a cylindrical pellet for 15 minutes at 250 MPa (see *Figure 12*, left). The pellet was then sintered for 10 hours at 1350 °C in air, with a heating and cooling rate of 2 K min^{-1}. The relative density of the sintered cylinders was above 97 % of the theoretical density obtained from Rietveld refinement. In order to achieve the specified relative density, it was necessary not to grind the powder below a d_{50} of 3.0 - 4.0 µm. The bar-shaped samples (see *Figure 12*, right), were cut from the sintered pellet using a diamond wire saw. To facilitate the attachment of voltage probes, two thin grooves were cut along the circumference of the sample, symmetrically positioned with a spacing of approximately one third of the bar length. Gold wires were then inserted into these grooves and fixed with gold paste. The two front faces of the bar-shaped sample were contacted with gold wires and two layers of gold foil, which were also fixed with gold paste.

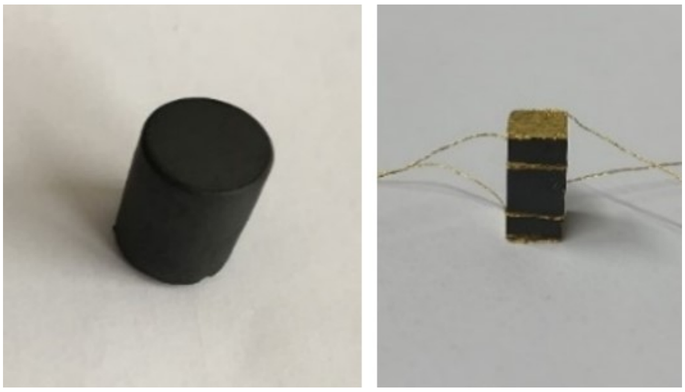

Figure 12 Isostatically pressed cylindrical pellet (left) and bar-shaped sample (approx. 5 × 5 × 11 mm^3) for measurements in linear-four-point geometry (right).

4.3.2 Surface modification by acid etching

The surface of the bar-shaped LNO sample was immersed for 6 minutes in a bath with 1.0 M nitric acid at room temperature and then rinsed with deionized water and cleaned for 10 minutes again in deionized water in an ultrasonic bath to completely remove any acid residues. The treatment in the ultrasonic bath caused the gold contacts to detach from the bar-sample, which were then reapplied as described in section 4.3.1.

4.3.3 Electronic conductivity measurements

The electronic conductivities σ_e of LNO and LNCO291 were measured with a combined current source and voltmeter (model 2400, Keithley) as a function of temperature and oxygen partial pressure in linear four-point geometry. Different oxygen partial pressures were adjusted using pre-mixed O_2-Ar test gases at total gas flow rates of 2 - 10 L h^{-1}. The equilibration time applied after each temperature change was between 8 and 10 hours on average.

4.3.4 Conductivity relaxation measurements

Both the chemical diffusion coefficient D_{chem} and the chemical surface exchange coefficient k_{chem} of oxygen of LNO and LNCO291 were determined by in-situ dc-conductivity relaxation measurements on the previously described dense, bar-shaped sample as a function of oxygen partial pressure and temperature. After equilibration of the sample at a certain temperature, which normally takes 8 to 10 hours, the oxygen partial pressure was abruptly changed by a factor of 1.5. Depending on the direction of the change in oxygen partial pressure, oxygen was either absorbed or released from the material. Since the electronic conductivity of the sample is a function of the oxygen content, this process leads to a temporal relaxation of σ_e towards a new equilibrium state. Kinetic parameters, D_{chem} and k_{chem}, were determined by fitting the appropriate solution of the diffusion model [60] to the relaxation curves.

4.3.5 Measurement setup

To determine the electrical conductivity and conductivity relaxation curves, the sample was mounted on an alumina sample holder and placed in a quartz glass reactor (see *Figure 13*) in a horizontal tube furnace controlled by a PID controller (Eurotherm Mod. 847).

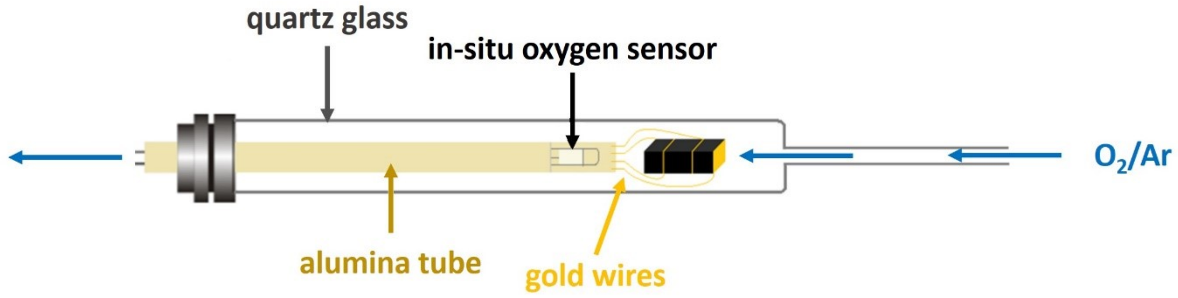

Figure 13 Illustration of the bar-shaped sample in the quartz glass reactor.

Measurements were carried out between 600 and 800 °C with flow rates between 2 and 10 L h^{-1} in various O_2/Ar-gas mixtures supplied by Linde Gas GmbH. The sample temperature was measured using a type S sheathed thermocouple placed close to the sample. Currents of 200 mA were applied to the sample using a current source meter (Keithley 2400). The resulting sample voltage was measured using a nanovoltmeter (Keithley 182).

4.4 Preparation and characterization of electrochemical cells

4.4.1 Preparation of electrolyte substrates for symmetrical cells

Gadolinia-doped ceria - $Ce_{0.9}Gd_{0.1}O_{1.95}$ (CGO) – powder with analytical grade quality purchased from Cerpotech was used as starting material for the preparation of the dense electrolyte substrates. For this, approximately 4.5 g of powder was weighed in a weighing pan, placed in a 2.5 cm diameter press mold and uniaxially pressed for 10 minutes at 40 MPa in a hydraulic press from Specac company. The pellets were then sintered for 10 hours at 1450 °C in air, with a heating rate of 2 K min^{-1} and a cooling rate of 1 K min^{-1}. Afterwards the surface was ground to remove burrs and unevenness from the sintered pellet and to ensure a good adhesion of the screen-printing paste, which is later applied using a screen-printing machine. The “Beta Grinder Polisher”, manufactured by Buehler, was used to grind the substrates. *Figure 14* shows the sequence of grinding steps as well as the grit number and the size of the SiC-sanding papers used.

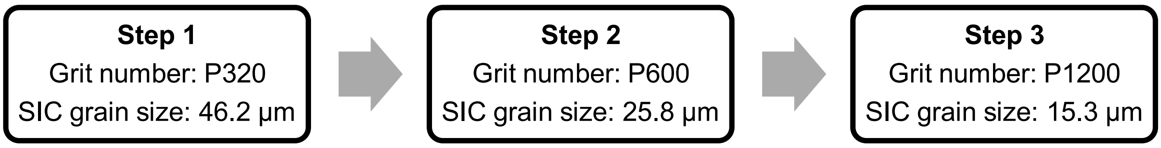

Figure 14 Flow chart of the individual grinding steps.

4.4.2 Preparation of screen-printing paste

In order to prepare the screen-printing paste, the LNO powder was mixed with an ink vehicle consisting of a mixture of terpineol as solvent and polyvinyl butyral (PVB, 16 wt.-%) as binder. For the production of 10 g screen-printing paste with a powder loading of 66 wt.-%, 6.6 g LNO powder and 3.4 g vehicle were utilized. The paste was then homogenized using a three-roller mill with alumina oxide rolls from the company EXAKT. The distance between the rollers was adjusted in the sequence 15-7, 7-3, 3-1 and 1-1, where the double numbers referred to the gap widths (arbitrary units) of the ingoing and outgoing gap. Once the paste passed through the three-roller mill at the narrowest roller distances (i.e. 1-1), it could be assumed that the paste had been sufficiently homogenized for the screen-printing process.

4.4.3 Screen-printing

The porous electrodes of electrochemical cells are manufactured by means of screen-printing process. Using a semi-automatic screen-printing machine (S40, Mechatronic Systems), the LNO paste is printed onto the electrolyte substrate through a screen using a rubber squeegee. In order to achieve the desired geometrical shape for the intended application, the mesh openings of the screen are rendered impermeable through the use of a stencil. A stencil with a circular opening of 13 mm diameter was selected for all electrodes produced within the scope of this work. The distance between the sieve and the electrolyte substrate was approximately 1 mm. After the screen-printing step the electrodes were dried for 30 minutes at 60 °C and sintered for one hour at 1200 °C with a heating rate of 5 K min^{-1} and a cooling rate of 2 K min^{-1}.

4.4.4 Sol-gel wet infiltration

For the infiltration process, two stock solutions were used. The first solution was prepared by dissolving $Ni(NO_3)_2 \cdot 6\,H_2O$ in deionized water, while the second solution was prepared by dissolving $La(NO_3)_3 \cdot 6\,H_2O$ in deionized water (both metal nitrates with analytical grade quality purchased from Merck KGaA). Citric acid was then added to the solution to achieve a molar ratio between metal nitrates and citric acid of 0.75:1.

After dissolving the nickel nitrate with a molarity of 1 M and the citric acid, the solution was mixed with ammonia-solution until pH 5 was reached. A few drops of the wetting agent Triton X-100 were then added to improve the wetting behavior of the precursor solution.

During the preparation of the La-stock solution, the addition of citric acid resulted in the formation of a precipitate of $La(OH)_3$. This was observed even with the addition of small quantities of citric acid. The low pH value of the stock solution resulted in the electrode being etched away. In order to circumvent this issue, a sufficient quantity of EDTA (ethylenediaminetetraacetic acid) was added until the precipitate was fully dissolved. EDTA is a complexing agent that forms chelates with La^{3+} ions, thus enabling free hydroxide ions in the solution. To increase solubility and reduce precipitation, deionized water was added in addition to the EDTA.

For infiltration, a few drops of the respective stock solutions were applied to the LNO electrodes and soaked for five minutes. The excess liquid on top of the electrode was removed with a cloth soaked in ethanol. Subsequently, the cells were subjected to a drying process at 100 °C for a period of ten minutes, followed by annealing at 500 °C for half an hour. *Figure 15* provides an overview of the infiltration process.

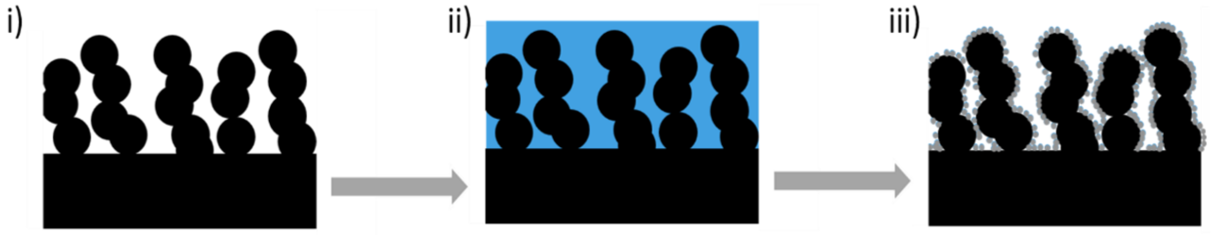

Figure 15 Schematic illustration of sol-gel wet infiltration: i) prepared porous electrode; ii) the nitrate stock solution is soaked in the porous electrode and iii) by thermal annealing oxide grains are formed on the surface of the porous electrode.

Afterwards the samples were weighed in order to monitor the increase in weight associated with each infiltration step. This process was performed thrice until the mass fraction of the infiltrated material in the backbone structure reached a value between 8 and 12 wt.-%.

4.4.5 Electrochemical measurements

For electrochemical measurements, the cells were mounted in the Probostat A-7 with a base unit heating system (NORECS Norwegian Electro Ceramics AS). The flow of the pre-mixed O_2/Ar gas was regulated with a rotameter (Vögtlin V-100). The top part of the Probostat, where the cell was mounted, was placed inside a vertical tube furnace (Elite, UK) with temperature controller (Eurotherm 2216e, UK). All impedance and current-voltage measurements within this work were performed with a frequency response analyzer (Novocontrol Alpha-A, Germany) with potentiostat/galvanostat interface (Novocontrol POT/GAL 15V/10A, Germany). Impedance measurements were carried out in four-wire configuration using the software WinDeta (Novocontrol, Germany). Impedance spectra were scanned under open circuit voltage (OCV) in a frequency range of 1 MHz to 10 mHz with ten measuring points per decade and an excitation voltage of 20 mV (rms). The obtained impedance spectra were evaluated via complex non-linear least squares fits using the software package WinFit (Novocontrol, Germany). *Figure 16* depicts the equivalent circuit diagram which was used to model the impedance spectra. The equivalent circuit comprises an inductance L_0, which is generated by the sample holder, an ohmic resistance R_0 corresponding to the electrolyte and the electrodes, and three $R|CPE$ elements, which correspond to at least three electrode processes.

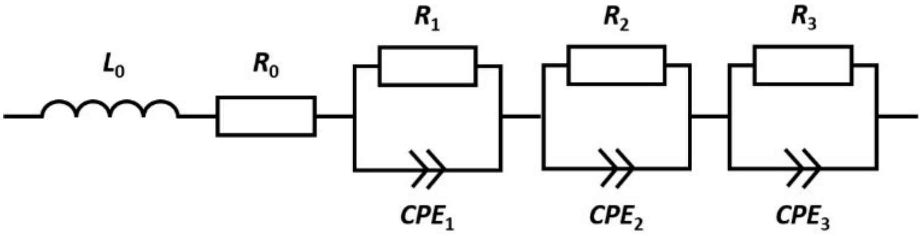

Figure 16 Equivalent circuit used for interpretation of impedance spectra.

The influence of L_0 is discernible in the high-frequency range of the impedance spectra, where it manifests as a tail-like section parallel to the imaginary axis. The horizontal distance of the spectrum from the origin of the diagram is described by the resistance R_0. It is comprised of contributions from the electrolyte, the electrodes and the contacts. The polarization resistance R_{pol} of the electrodes is described by a series of $R|CPE$ elements. Each $R|CPE$ element consists of a resistor R, which is connected in parallel with a constant phase element CPE (i.e. a generalized capacitor). In order to determine the value of R_{pol}, it is necessary to subtract the first term of the fit function, which is equal to L_0+R_0. For the impedance spectra obtained in this work, R_{pol} can be further partitioned into three semicircles by using three $R|CPE$ elements connected in series [79].

4.5 Post-test analysis

4.5.1 Scanning electron microscopy

Scanning electron microscopy (SEM) was used to characterize the microstructure and the electrode-electrolyte interface of electrochemical cells. Images were recorded in secondary electron (SE) mode for topographical contrast as well as in backscattered electron (BSE) mode for material contrast. SEM imaging and energy-dispersive X-ray spectroscopy (EDX) for the fuel electrode-supported cell with LNCO291-oxygen electrode were performed with a field-emission SEM (Clara, Tescan) equipped with an EDXS-detector (Oxford Instruments INCA) at an acceleration voltage of 15 kV. The SEM images and EDX analyses of the symmetrical cells with LNO-electrodes and La- and Ni-infiltrated LNO-electrodes were carried out using a SEM (Vega, Tescan) with an EDXS detector (Oxford Instruments INCA) at an acceleration voltage of 10 and 20 kV. The microstructure of the etched bar-shaped sample was investigated by field emission scanning electron microscopy (FESEM) using a ZEISS 450 GeminiSEM in SE and BSE mode with 5 kV and 3 nA.

For the preparation of cross sections, the symmetrical cells were embedded in epoxy resin and cut in half with a diamond wire saw. In order to obtain a flat surface, the grinding was carried out using a grinder (Beta Grinder Polisher) equipped with a grinding disc (P240). The surface was then polished with a polishing machine (Tegramin-20 from Struers company) using diamond suspensions of different grain sizes (9 µm and 3 µm) and a 0.25 µm SiO_2 suspension for finishing. Details of the grinding/polishing steps are shown in *Table 1*.

Table 1 Grinding and polishing steps for preparation of cross sections for SEM-measurements.

Working step	***Suspension***	***Time / min***
grinding	P240 + H_2O	1
polishing	DiaPro Allegro/Largo 9 µm	5
polishing	DiaPro Allegro/Largo 6 µm	10
polishing	OP-S Nondry 0.25 µm	5

To ensure good sample conductivity for SEM imaging, a thin layer of gold was sputtered onto the polished sample, which was then contacted with silver paste.

4.5.2 X-ray photoelectron spectroscopy

X-ray photoelectron spectroscopy (XPS) was performed with a lab based near ambient pressure XPS (NAP-XPS) system from SEPCS (Berlin, Germany) using a XR 50 microfocus X-ray source providing Al K(alpha) radiation source with a spot size of 350 µm for excitation achieving an energy resolution of around 0.2 eV, a Phobios 150 NAP hemispherical analysator and a custom built sample stage by Huber Scientific (Vienna, Austria). Data were analyzed with CasaXPS software (Casa Software Ltd., Teignmouth, UK). Peaks were fitted after Shirley or linear background subtraction with Gauss-Lorentz sum functions. Peak positions and full width at half-maximum (FWHM) were left unconstrained. Peak positions were referenced either to the valence band signal (Fermi edge) or to the C1s peak corresponding to adventitious carbon (284.7 eV).

5 RESULTS AND DISCUSSION

The results of the research performed are presented and discussed in the following sections. The first section presents the results of Co-substitution on the B-site in $La_2NiO_{4+\delta}$. In the second section, the modification of the surface with acid is discussed and finally, in the third section, the results of cell tests and post-test analyses are presented.

5.1 Effect of partial substitution of Ni with Co

This section provides a comprehensive characterization of cobalt-substituted lanthanum nickelate $La_2Ni_{0.9}Co_{0.1}O_{4+\delta}$ (LNCO291) in terms of its crystal structure, thermal expansion behavior, bulk and charge transport properties, and oxygen non-stoichiometry. In order to gain fundamental insights into the effects of cobalt substitution on the B-site of the A_2BO_4-structure, a comparison is made between LNCO291 and $La_2NiO_{4+\delta}$ (LNO).

The majority of the findings presented in this sub-chapter have already been published in Eisbacher-Lubensky et al. [39].

5.1.1 Crystal structure and phase purity

The phase purity and structure of LNCO291 and LNO were studied at room temperature by means of powder X-ray diffraction analysis combined with Rietveld refinement using the software package Topas [78]. The XRD-patterns of LNCO291 and LNO confirm the K_2NiF_4-type structure with high phase purity and are presented in *Figure 17*. The reflections are consistent with the orthorhombic space group *Fmmm* (SG #69), which is also found for LNO in literature [80]. The structure models of both compounds obtained by Rietveld refinement and depicted via the 3D visualization program VESTA are presented in *Figure 18*.

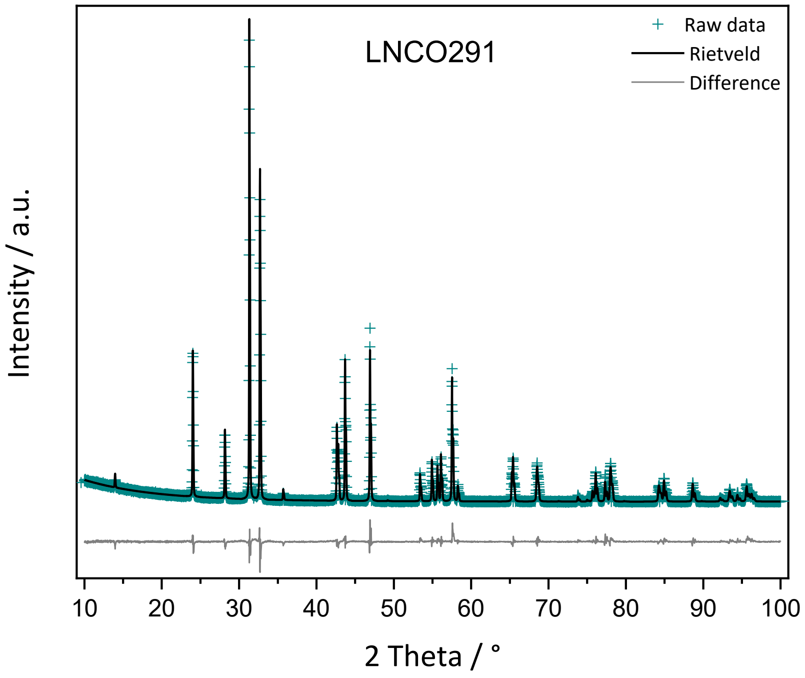

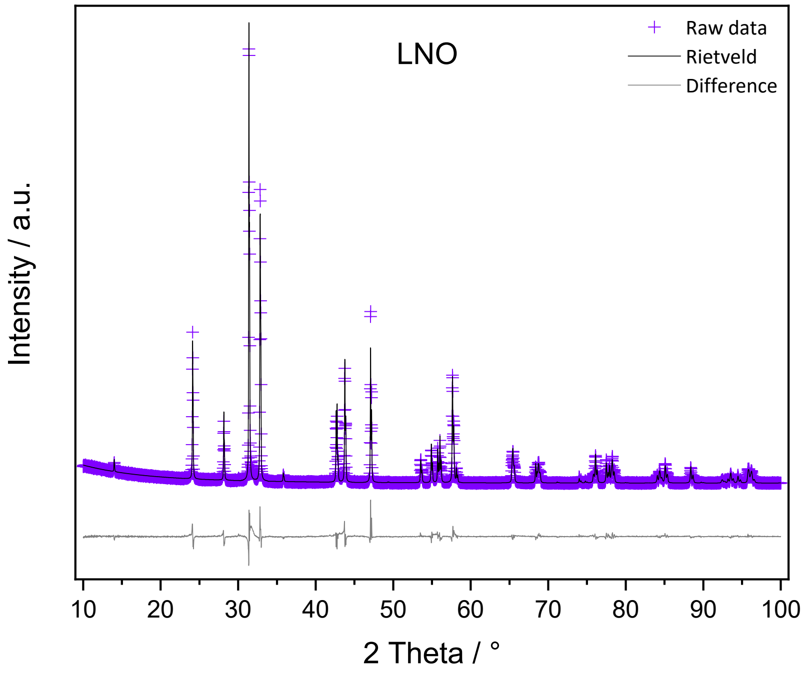

Figure 17 Room temperature powder diffraction patterns (crosses) of LNCO291 [39] (top) and LNO (bottom) and Rietveld refinement (black line).

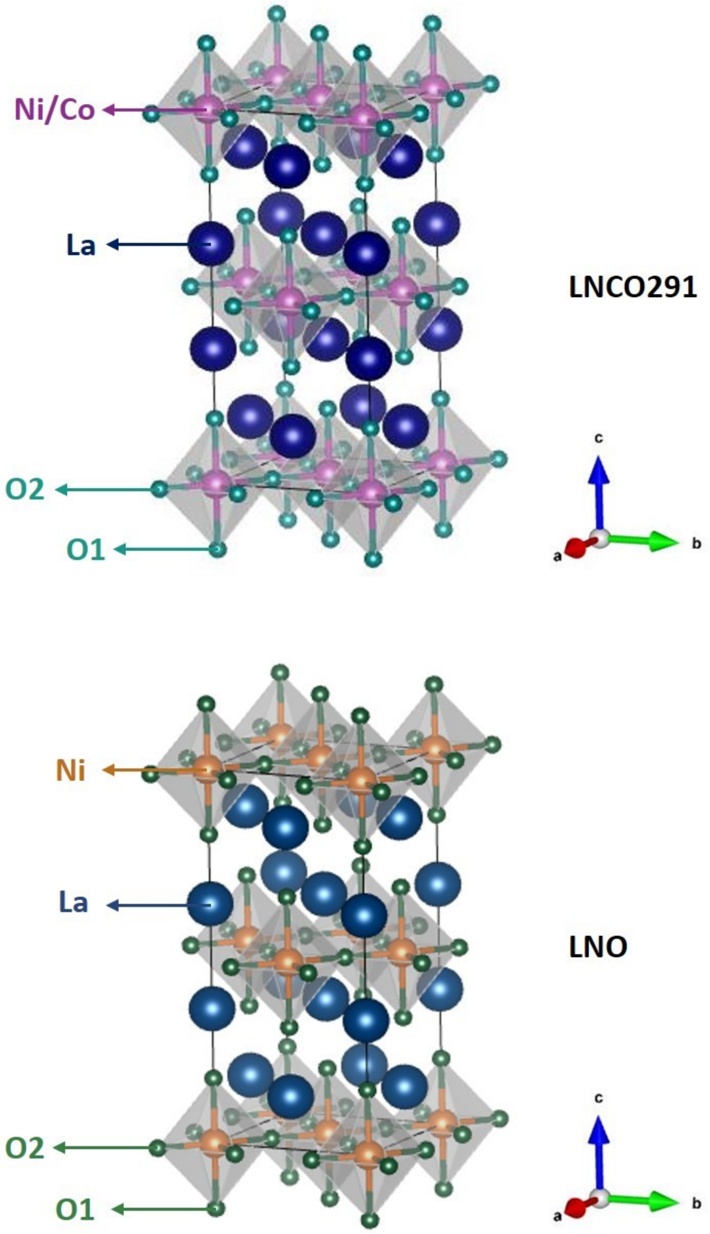

Figure 18 Structure models of LNCO291 [39] (top) and LNO (bottom) as obtained by Rietveld refinement.

In *Table 2* the lattice parameters and the calculated cell volumes of the unit cells of LNCO291 and LNO are compared. *Table 3* shows the atomic positions and bond lengths of the compounds obtained by Rietveld refinement.

Table 2 Lattice parameters and unit cell volumes of LNCO291 [39] and LNO, space group Fmmm (SG #69). Z represents the number of formula units per unit cell.

Material	***a/Å***	***b/Å***	***c/Å***	***V/Å^3***	***Z***
LNCO291	5.4678(3)	5.4713(4)	12.651(7)	378.49	4
LNO	5.4636(4)	5.4583(8)	12.690(8)	378.47	4

The lattice parameters *a* and *b* of LNCO291 are slightly higher than those of LNO, but the opposite is true for the lattice parameter *c*, which extends in the direction perpendicular to the perovskite and rock salt layers. The smaller cell volume of LNCO291 is a consequence of the difference in the parameter *c*. This phenomenon has already been observed by several research groups [68,70,80].

Table 3 Atomic positions in LNCO291 [39] and LNO. As cobalt cannot be distinguished from nickel in X-ray diffraction, it is also assumed in Rietveld refinement that the atomic positions of cobalt correspond to those of nickel.

LNCO291	***x***	***y***	***z***	***Ni/Co-O1/Å***	***Ni/Co-O2/Å***
La	0	0	0.3605(5)	2.212(6)	1.93372
Ni/Co	0	0	0		
O1	0	0	0.1749(5)		
O2	0.25	0.25	0		
LNO	***x***	***y***	***z***	***Ni-O1/Å***	***Ni-O2/Å***
La	0	0	0.3598(3)	2.203(6)	1.93076
Ni	0	0	0		
O1	0	0	0.1746(4)		
O2	0.25	0.25	0		

The lattice parameter *c* is therefore more strongly influenced by Co-substitution than the lattice parameters *a* and *b*. Two different explanations can be proposed for this phenomenon. On the one hand, Co-substitution has the effect of significantly increasing the oxygen over-stoichiometry, which will be discussed below in more detail. It is assumed that a higher oxygen over-stoichiometry will result in an increase in the *c*-parameter in LNO [63,81]. The shrinkage of the unit cell along the *c*-axis in LNCO291 can therefore be attributed to differences in the radii of the transition metal ions. If identical values for δ were assumed in LNO and LNCO, then the c-axis in LNCO291 would still be shorter due to the marginally smaller ionic radius of Co^{2+} (0.65 Å for coordination number 6) compared to Ni^{2+} (0.69 Å for coordination number 6) [62]. Conversely, the literature asserts that a low cobalt content in LNO results in cobalt being present exclusively in the oxidation state 3+ [80]. Consequently, the significantly smaller size of the Co^{3+}-ion (0.55 Å for coordination number 6) leads to a general reduction in the size of the unit cell along the c-axis [62,80].

5.1.2 Thermal expansion

In order to assess the suitability of Co-substituted LNO as an oxygen electrode, it is necessary to evaluate the thermal expansion. It is essential that the coefficient of thermal expansion is closely matching that of the electrolyte in order to prevent delamination. The thermal expansion curves and the thermal expansion coefficients α in different atmospheres are illustrated in *Figure 19*. The α-values, as determined by the slope of a secant line connecting two points on the thermal expansion curves at 100 and 900 °C are also given in *Table 4*.

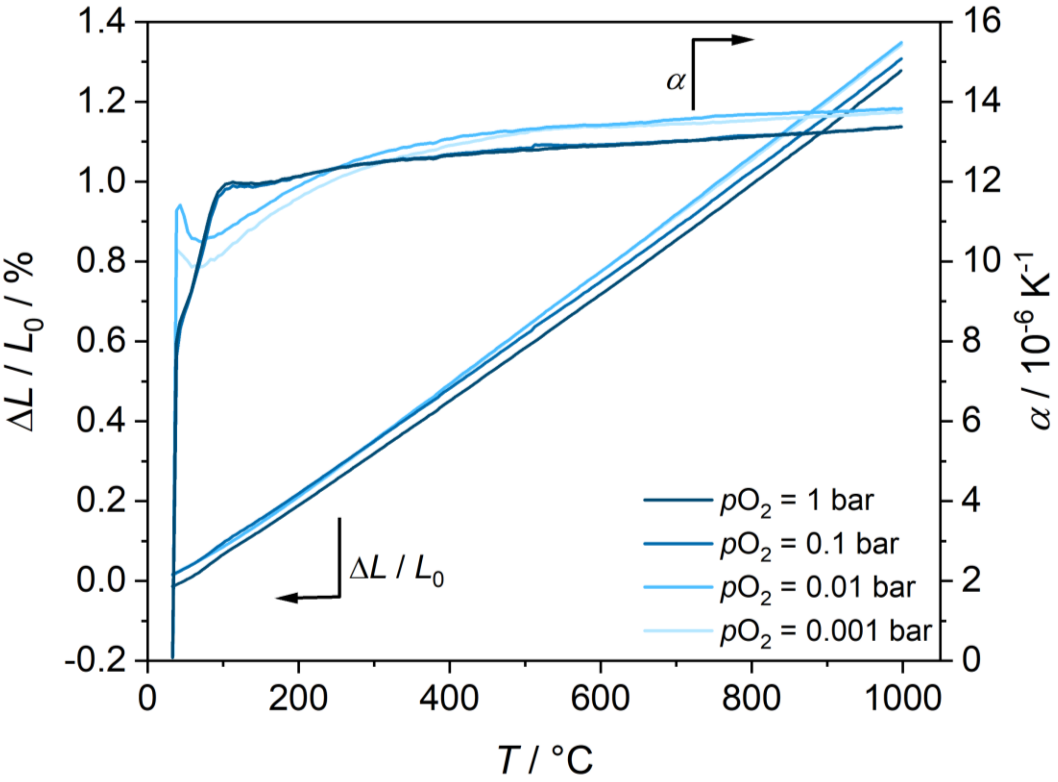

Figure 19 Thermal expansion curves and thermal expansion coefficients of LNCO291 [39] in different O_2/Ar-atmospheres.

Table 4 Thermal expansion coefficients of LNCO291 [39].

pO_2 / bar	α / 10^{-6} K^{-1}
1	13.35
0.1	13.36
0.01	13.99
0.001	13.92

The substitution of Ni with 10 % Co has no influence on the thermal expansion, as the values are in good agreement with those of Co-free LNO, which are between 13.7 × 10^{-6} and 14.8 × 10^{-6} K^{-1} [82,83]. The thermal expansion of LNCO291 appears to exhibit a slight increase at lower pO_2, as illustrated in *Figure 19*. This may be attributed to a slight enhancement of the contribution of chemical expansion to the overall thermal expansion behavior. Kharton et al. [82] also identified this phenomenon. The α-values are promising for use as oxygen electrode material in SOCs, as they are lower compared to the values of the common electrode materials $La_{0.6}Sr_{0.4}CoO_{3-\delta}$ (18.9 × 10^{-6} K^{-1}) and $La_{0.6}Sr_{0.4}Co_{0.8}Fe_{0.2}O_{3-\delta}$ (16.0 × 10^{-6} K^{-1}) [84,85]. The values of LNCO291 and LNO are found to correspond more closely to the those of the solid electrolyte materials used, namely gadolinia-doped ceria and yttria-stabilized zirconia, which exhibit α between 10 × 10^{-6} K^{-1} and 13 × 10^{-6} K^{-1} [86].

5.1.3 Oxygen non-stoichiometry

The mass change of LNCO291 between 20 and 900 °C in dry O_2-Ar mixtures was determined by thermogravimetry, as illustrated in *Figure 20*. The good agreement between the heating and cooling curves indicates that the experimental data represents true equilibrium conditions. As the first thermal cycle contains artefacts related to adsorbed gas species, only the second and third thermal cycles are shown in *Figure 20*. The observed mass increase during the isotherm at 900 °C is attributed to a drift in the instrument's baseline.

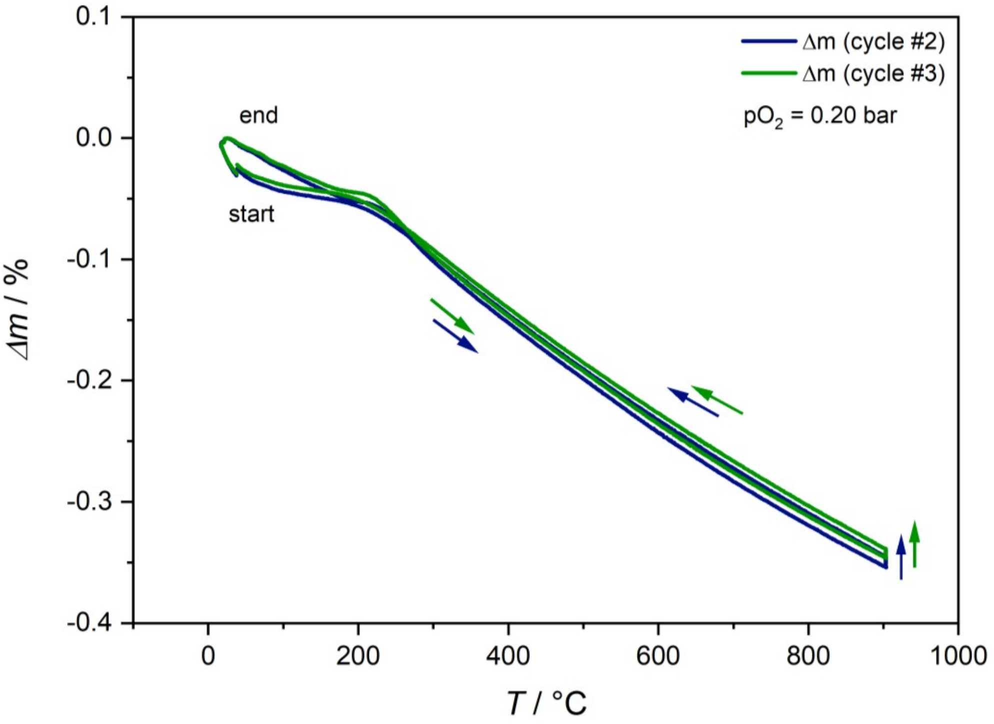

Figure 20 Thermal cycles (#2 and #3) of LNCO291 [39]. Thermogravimetry was conducted between 20 and 900 °C in dry Ar/20 vol% oxygen atmosphere at heating and cooling rates of 5 K min^{-1}.

The changes in oxygen non-stoichiometry $\Delta\delta$ of LNCO291 and LNO were determined from the mass changes of the samples, whereby the data of LNO were taken from reference [60]. The absolute values of δ were determined using reference points from the literature [69,87] at 750 °C. The results of oxygen non-stoichiometry are presented in *Figure 21* as a function of temperature. The data are consistent with results from the same literature sources [69,87] at temperatures between 650 and 850 °C.

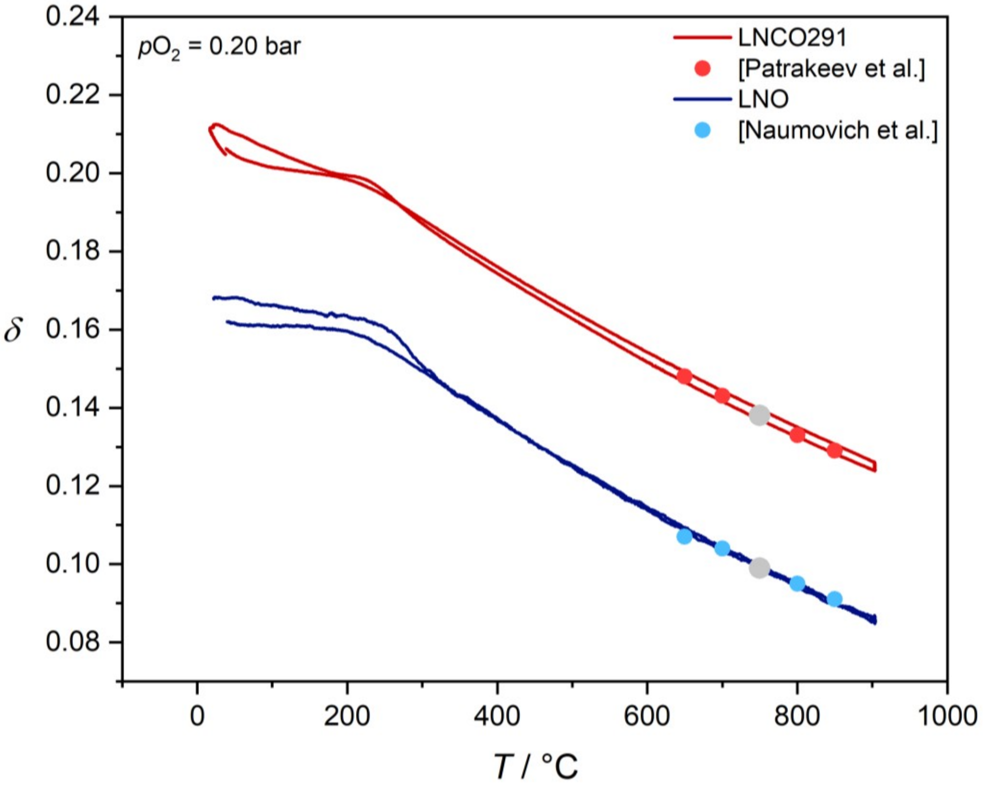

Figure 21 Oxygen non-stoichiometry of LNCO291 (red) and LNO (blue) at 0.20 bar pO_2 as a function of temperature [39]. The absolute non-stoichiometry values were fixed by reference points (solid grey) at 750 °C obtained from references [69,87].

The incorporation of oxygen into the compound is exothermic, which can be observed in the decrease in oxygen non-stoichiometry with increasing temperature of LNCO291 and LNO. In literature [88], the over-stoichiometry of LNO is ranging between 0 and 0.16 at 20 – 900 °C and 0.20 bar pO_2. The values determined in this work (see *Table 5*) fall within this range.

Using the pO_2-dependence of oxygen non-stoichiometry from literature [69,87], the thermodynamic factor at constant temperature can be calculated according to:

$$\gamma_O = \frac{1}{2}\left(\frac{\partial \ln pO_2}{\partial \ln c_O}\right)_T = \frac{1}{2}\left(\frac{\partial \ln pO_2}{\partial \ln(4+\delta)}\right)_T \qquad 5.1$$

where a linear regression analysis of pO_2 vs. $4+\delta$ in a double-logarithmic representation was conducted. The thermodynamic factors of oxygen for LNCO291 (*Table 5*) were found to range between

520 and 440 (650 - 850 °C) at 0.10 bar pO_2. Jeon et al. [89] provide thermodynamic factors between 543 and 455 for LNO in the temperature range from 800 to 1000 °C.

Table 5 Oxygen non-stoichiometry δ and thermodynamic factor γ_O of LNCO291 at 0.10 bar pO_2 and different temperatures [39].

T / °C	**δ**	**γ_O**
650	0.148	519
700	0.143	495
750	0.138	476
800	0.133	455
850	0.129	439

5.1.4 Electronic conductivity

The electronic conductivity σ_e of LNCO291 was investigated in linear-four-point geometry as a function of temperature at different oxygen partial pressures (*Figure 22*). Within the measured temperature range (600 - 850 °C) and the specified oxygen partial pressures ($0.001 \leq pO_2/\text{bar} \leq 0.1$), σ_e ranges between 45 and 70 S cm^{-1}.

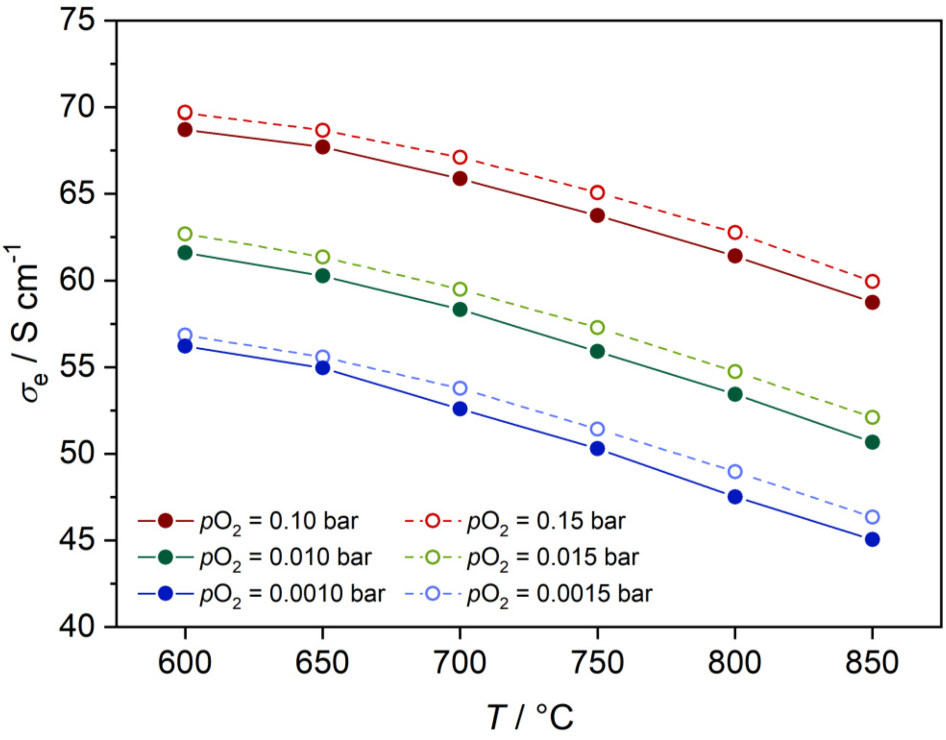

Figure 22 Electronic conductivity σ_e of LNCO291 as a function of temperature and oxygen partial pressure [39]. Lines serve as visual guides for the eye.

Two effects are discernible. Firstly, the electronic conductivity decreases with increasing temperature. Secondly, σ_e decreases with decreasing oxygen partial pressure, which is also illustrated in *Figure 23*. The second observation shows that the electronic conductivity of LNCO291 is subject to a p-type conduction mechanism, which has already been confirmed several times in the literature for this material class [59,90]. This is due to the release of oxygen from the lattice and an associated decrease in the electron hole concentration [59]. In *Figure 22* it can also be observed that the pO_2-dependence of the electronic conductivity of LNCO291 is at any temperature at 0.15, 0.015 or 0.0015 bar pO_2 (dashed lines) σ_e slightly higher than at 0.10, 0.010 or 0.0010 bar pO_2 (solid lines) as expected for a p-type semiconductor. This behavior serves as the foundation for conductivity relaxation measurements, which will be discussed in the next section.

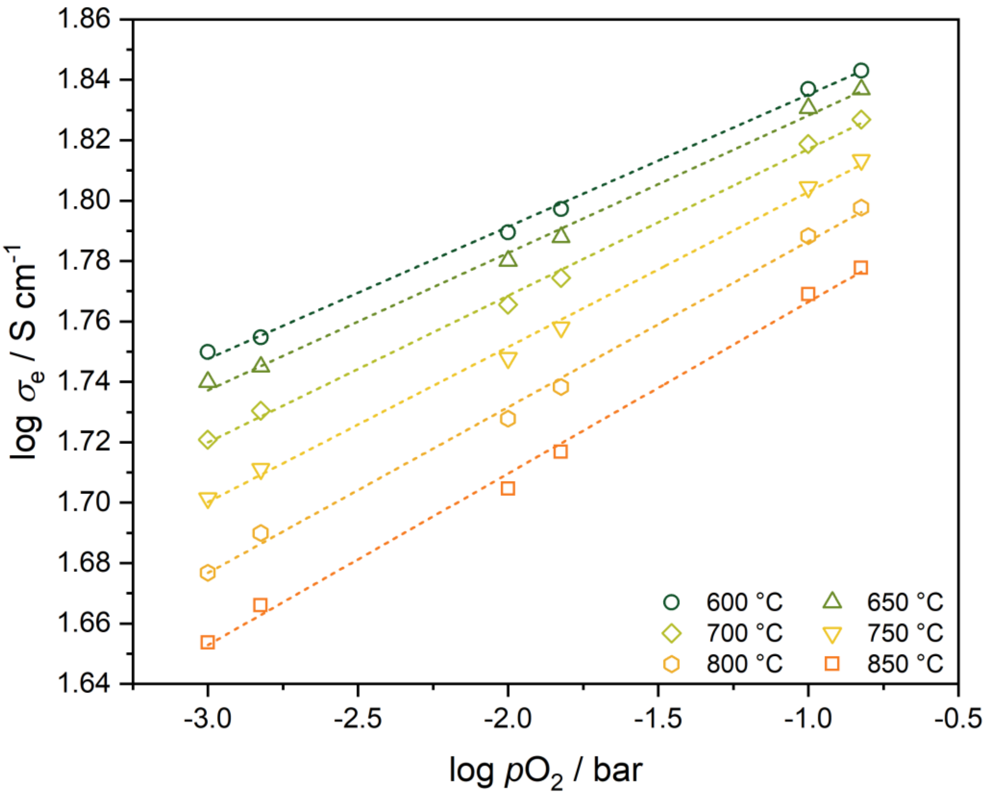

Figure 23 Oxygen partial pressure dependencies of the electronic conductivity σ_e *of LNCO291 between 600 and 850 °C [39]. Lines serve as visual guides for the eye.*

The substitution of nickel with cobalt does not result in an improvement in the electronic conductivity, as shown in *Figure 24*. This is an unexpected outcome, given that the oxygen over-stoichiometry is significantly increased by Co-doping, as presented in the previous sub-chapter, which in turn results in an increase in the concentration of electron holes. One explanation for this phenomenon is that cobalt reduces the mobility of holes, likely by localizing defect electrons and thus trapping electronic charge carriers by forming stable Co^{3+}-states [59,69,87].

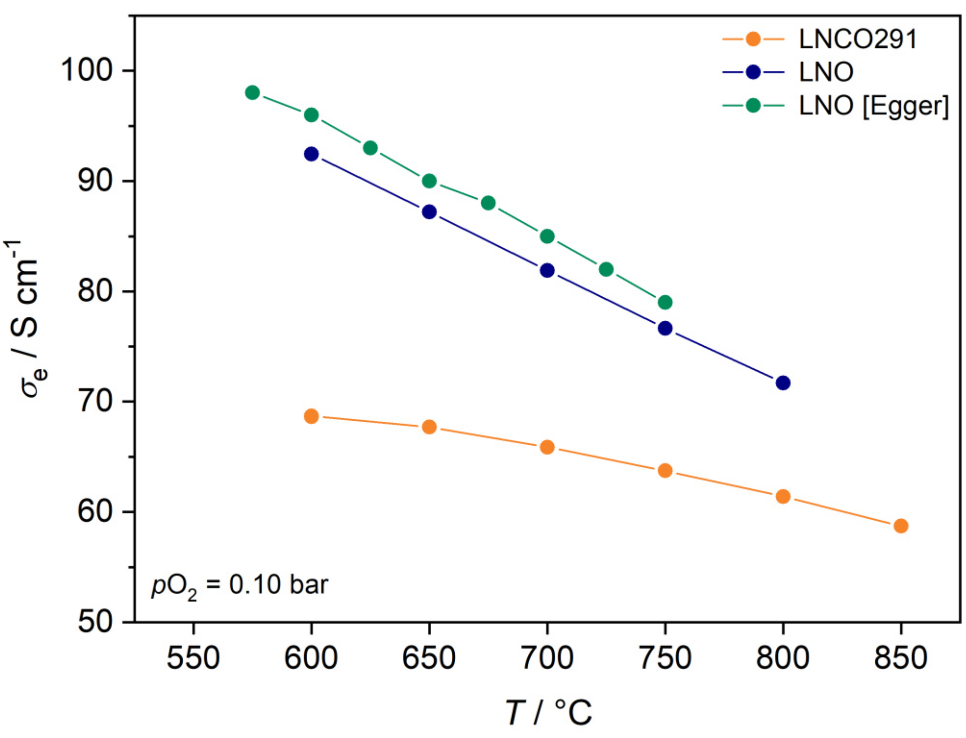

Figure 24 Electronic conductivity σ_e of LNCO291 [39] and LNO from this work and literature [60] as a function of temperature at pO_2 = 0.10 bar. Lines serve as visual guides for the eye.

The differences between the LNO values from this work and those from the literature [60] are within the measurement uncertainty of the measurement method. Nevertheless, the observation that Co-substitution does not enhance the electronic conductivity in nickelates has been corroborated by other research groups [38,59,82]. Vibhu et al. [38] investigated the influence of Co-substitution in $La_2Ni_{1-x}Co_xO_{4+\delta}$ with x = 0-0.2 with respect to the maximum of σ_e versus temperature and showed that the maximum shifts to higher temperatures with increasing Co-content.

5.1.5 Oxygen exchange kinetics

The chemical surface exchange coefficients k_{chem} and the chemical diffusion coefficients D_{chem} of oxygen of LNCO291 and LNO are discussed below. The activation energies were calculated by linear regression analysis of the data in Arrhenius representation and are summarized in *Table 6* and *Table 7*. The conductivity relaxation measurements were conducted by abruptly changing the oxygen partial pressure around the sample, as described in *Chapter 4.3.4*. The respective direction - oxidation and reduction - is labelled "ox" and "red" in the diagrams.

Figure 25 illustrates the Arrhenius plot of the surface exchange coefficient k_{chem} of LNCO291 and LNO at different oxygen partial pressures. k_{chem} increases with increasing temperature and increasing oxygen partial pressure. The comparison with data of the Co-free material LNO from reference [91] (grey line) and this work (red and orange lines) demonstrate that the substitution of nickel with cobalt on the B-site results in a significant increase in the surface exchange coefficients of oxygen of up to a factor of 30 compared to the values from literature and up to a factor of 8 from compared to values of this work at 600 °C. Despite using the same measurement method, the literature and this work give different values for LNO. This is due to a different setup and the fact that Egger and Sitte [91] applied a silver layer on the surface of the bar-sample.

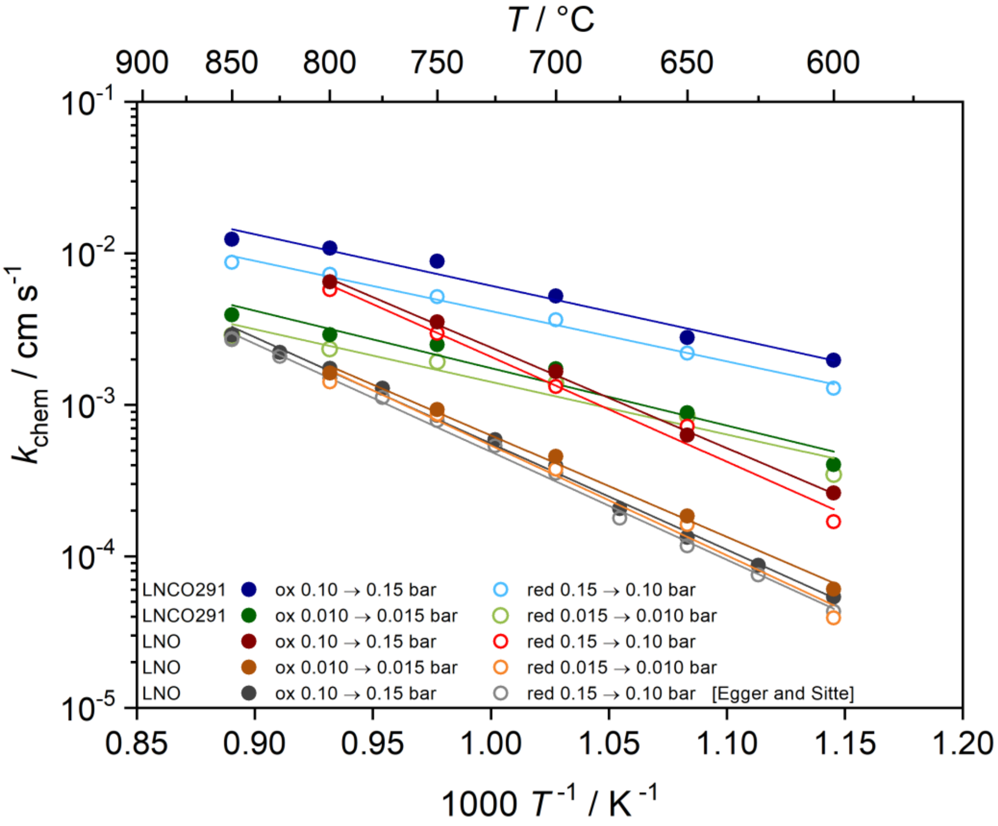

Figure 25 Arrhenius representation of chemical oxygen surface exchange coefficients k_{chem} of LNCO291 [39] and LNO from this work and from literature [91] at different oxygen partial pressures.

Table 6 Activation energies of LNCO291 and LNO calculated by linear regression analysis of the data in Arrhenius representation of the oxygen surface exchange coefficients k_{chem}.

k_{chem}	E_a/kJ mol^{-1}			
	ox **0.10 – 0.15 bar**	**red** **0.15 – 0.10 bar**	**ox** **0.010 – 0.015 bar**	**red** **0.015 – 0.010 bar**
LNCO291 [39]	64 ± 3	65 ± 6	73 ± 8	67 ± 8
LNO	130 ± 4	134 ± 4	128 ± 5	139 ± 10
LNO [91]	135 ± 6	137 ± 6	-	-

The difference in the oxygen exchange coefficients between the Co-free and the Co-substituted lanthanum nickelate becomes smaller at higher temperatures. This is due to the large differences in the activation energies, which are in the range of 64 – 65 kJ mol^{-1} for LNCO and 130 – 137 kJ mol^{-1} for LNO. Kilner and Shaw [32] determined tracer oxygen surface exchange coefficients of LNO and LNCO by isotope exchange depth profile technique coupled with secondary ion mass spectrometry (IEDP-SIMS) and observed the analogous effect. In particular, they state that the activation energies decrease with increasing Co-content, from 124 kJ mol^{-1} at a Ni/Co-ratio of 100:0 to 24 kJ mol^{-1} at a Ni/Co-ratio of 50:50 on the B-site. The same effect of the substitution of Ni with Co was also observed for $Pr_2NiO_{4+\delta}$ (PNO) and cobalt-substituted $Pr_2Ni_{0.9}Co_{0.1}O_{4+\delta}$ (PNCO291) [42]. It is evident that the oxygen surface exchange process is accelerated by cobalt. It is also important to note that the effect of substituting nickel with cobalt is subject to a saturation effect. Munnings et al. [92] demonstrate that increasing the cobalt content beyond 10 % results only in a marginal enhancement in the oxygen exchange kinetics. Furthermore, it can be postulated that an even higher cobalt content may induce thermodynamic instability of the nickelate. For instance, the nickel-free material $La_2CoO_{4+\delta}$ is unstable at temperatures above 700 °C and decomposes into $LaCoO_3$ and La_2O_3. The results obtained in this study, in conjunction with those from the existing literature, indicate that the incorporation of cobalt on the B-site of nickelates results in a change in the surface exchange kinetics. The precise manner in which the interplay between oxygen surface exchange activity and surface chemistry operates remains a subject of investigation, as a definitive conclusion is not yet possible. The activating effect of cobalt is well documented, at least in heterogeneous catalysis, and numerous studies have been carried out on various reactions in the liquid and gaseous state, e.g. [93,94].

The chemical diffusion coefficients of oxygen D_{chem} are presented in *Figure 26* as Arrhenius plots. It can be observed that D_{chem} increases with increasing temperature but, in contrast to k_{chem}, is independent of the oxygen partial pressure. A comparison of the chemical diffusion coefficients of LNCO291 with that of the Co-free material LNO from the literature [91] and from this work reveals that the substitution of nickel with 10 % cobalt has no effect on D_{chem}. The calculated activation energies are also within the same range and therefore agree well (see *Table 7*). The reduction from 0.015 bar to 0.010 bar pO_2 exhibits a slight deviation from the other activation energies, which explains the higher measurement uncertainties at $T \leq 650$ °C and the absence of D_{chem}-values at 600 °C. Due to the higher activation energy of k_{chem} compared to D_{chem}, this is becoming even more prevalent at lower temperatures, which explains the absence of D_{chem}-values at 600 °C in *Figure 26.*

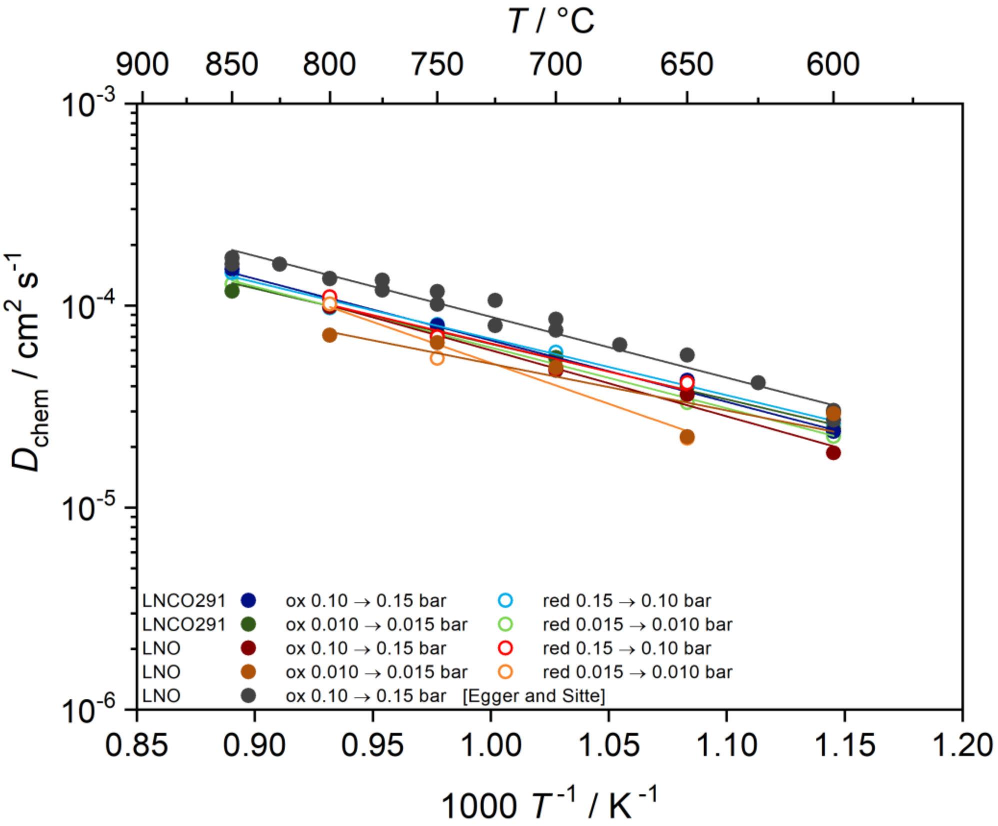

Figure 26 Arrhenius representation of chemical diffusion coefficients D_{chem} of LNCO291 [39] and LNO from this work and from literature [91] at different oxygen partial pressures.

Table 7 Activation energies of LNCO291 and LNO calculated by linear regression analysis of the data in Arrhenius representation of the chemical diffusion coefficients of oxygen D_{chem}.

D_{chem}	E_a/kJ mol^{-1}			
	ox 0.10 – 0.15 bar	**red 0.15 – 0.10 bar**	**ox 0.010 – 0.015 bar**	**red 0.015 – 0.010 bar**
LNCO291 [39]	58 ± 4	54 ± 2	53 ± 3	58 ± 2
LNO	60 ± 4	56 ± 7	54 ± 9	78 ± 14
LNO [91]	58 ± 5	-	-	-

The overall oxygen exchange kinetics of nickelates is frequently dominated by the surface exchange process, rendering the determination of oxygen diffusivities a challenging endeavor. D_{chem} values of LNO by Egger and Sitte [91] (*Figure 26*) could only be determined after depositing a thin layer of silver on the sample, acting as a catalyst for the surface oxygen exchange kinetics. It was not necessary to artificially enhance the oxygen surface exchange kinetics of LNCO291, as the surface exchange rates were sufficiently high to permit the determination of oxygen diffusion coefficients.

The previously calculated thermodynamic factors (see *Table 5*) and the kinetic parameters can be used to calculate the self-surface exchange coefficients k_{O} and the self-diffusion coefficients D_{O} of oxygen according to the following equations:

$$D_{\text{chem}} = D_O \, \gamma_O \tag{5.2}$$

$$k_{\text{chem}} = k_O \, \gamma_O \tag{5.3}$$

The complete dataset of the oxygen exchange kinetics measurements is summarized in *Table 8* including the calculated values of D_{O} and k_{O}.

Table 8 Chemical surface exchange coefficients k_{chem}, self-surface exchange coefficients k_O, self-diffusion coefficients D_O and chemical diffusion coefficients D_{chem}, of LNCO291 [39].

T / °C	**k_{chem} / cm s^{-1}**	**k_{O} / cm s^{-1}**	**D_{chem} / cm^2 s^{-1}**	**D_{O} / cm^2 s^{-1}**
650	2.78×10^{-3}	5.36×10^{-6}	4.26×10^{-5}	8.21×10^{-8}
700	5.22×10^{-3}	1.05×10^{-5}	4.78×10^{-5}	9.66×10^{-8}
750	8.88×10^{-3}	1.87×10^{-5}	7.97×10^{-5}	1.67×10^{-7}
800	1.08×10^{-2}	2.37×10^{-5}	1.07×10^{-4}	2.36×10^{-7}
850	1.24×10^{-2}	2.82×10^{-5}	1.51×10^{-4}	3.45×10^{-7}

Figure 27 presents a comparison of the self-diffusion coefficients of oxygen of LNCO291 with results from the literature. There is a good agreement between the diffusivities reported for LNO by Song et al. [95] and the results of LNCO291 from this work. However, the self-diffusion coefficients of oxygen from Kilner and Shaw [32] for LNCO291 are lower by a factor of 4 - 5. Nevertheless, the activation energies are found to be in close agreement between all data sets.

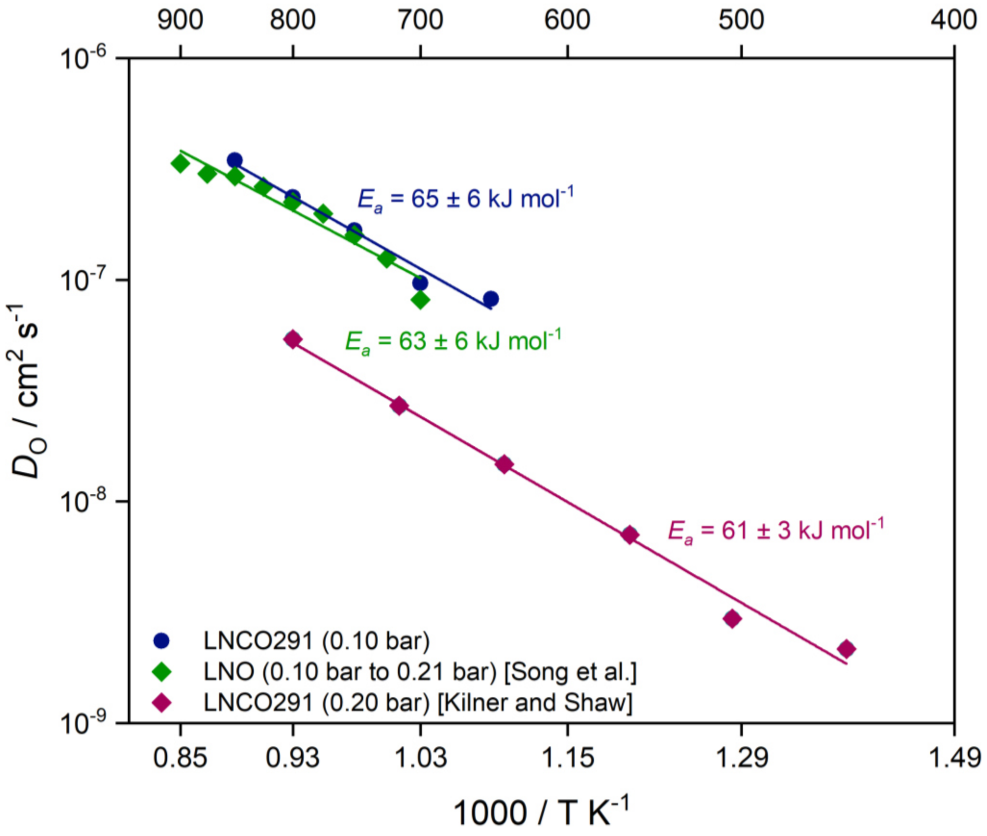

Figure 27 Arrhenius representation of self-diffusion coefficients D_O of oxygen of LNCO291 [32,39] and LNO [95] at different oxygen partial pressures.

It is important to note that the data from Song et al. [95] were determined using dc-conductivity relaxation measurements, in a manner analogous to the LNCO291 data presented in this work. In order to determine the oxygen tracer diffusion coefficients, Kilner and Shaw [32] employed the use of IEDP-SIMS. The cause of the discrepancy between the data obtained from CR-measurements and ^{18}O-tracer experiments remains uncertain.

5.1.6 Ionic conductivity of oxygen

Figure 28 presents results of the ionic conductivity of oxygen σ_i, which were determined using the Nernst-Einstein equation:

$$\sigma_\mathrm{i} = \frac{4\,F^2\,(4+\delta)\,D_\mathrm{O}}{R\,T\,V_\mathrm{m}} \tag{5.4}$$

with the self-diffusion coefficients D_O and the molar volume V_m (V_m = 57.0 cm^3 per mole formula unit for LNCO291 and V_m = 57.2 cm^3 per mole formula unit for LNO [89]) obtained by Rietveld refinement. The values are shown as σ_iT in Arrhenius representation (see *Figure 28*) at 0.10 bar pO$_2$ and the activation energies were calculated again using linear regression.

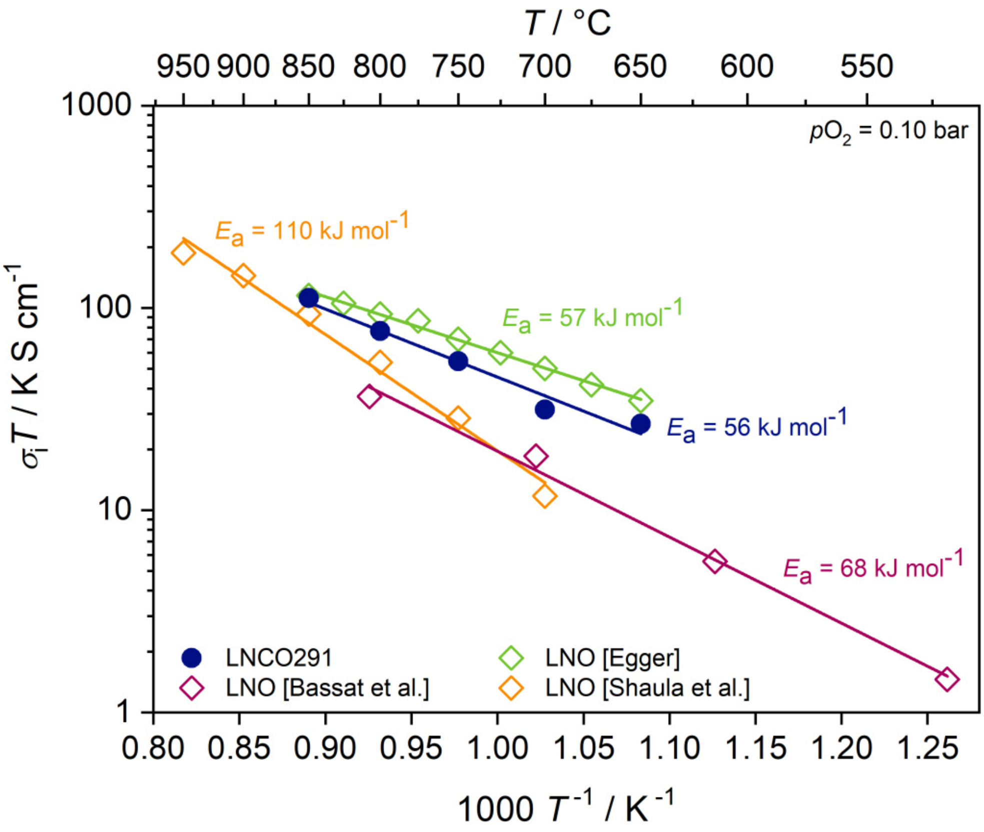

Figure 28 Ionic conductivities of oxygen σ_i and the associated activation energy of LNCO291 [39] in comparison with LNO-values from literature [60,71,96].

The ionic conductivity values of LNCO291 agree well with those of the Co-free material as reported by Egger [60]. Since the oxygen self-diffusion coefficients D_O of LNCO291 are found to be close to those of the Co-free material LNO, and these are included in the Nernst equation, no major difference in ionic conductivity is expected due to Co-substitution. However, when comparing these results with those of σ_i of LNO from the work of Shaula et al. [96], the agreement is not as good. Values are quite close at 850 °C, but due to differences in the activation energies considerable discrepancies in the ionic conductivities arise at lower temperatures. The results of LNO from the research of Bassat et al. [71] are in good agreement with those of Shaula et al. [96] at 700 °C. However, they show a significantly lower activation energy, which in turn is closer to the results of LNCO291 found in this work. The substantial disparity between the ionic conductivities of oxygen and their activation energies may be attributed to differences in the preparation procedure of the samples (e.g. affecting relative densities) or may be a consequence of the different measurement techniques employed. For determining σ_i, Shaula et al. [96] measured the oxygen permeation flux through an LNO membrane. In contrast, Bassat et al. [71] calculated the ionic conductivities, as in this work, from the self-diffusion coefficients of oxygen using the Nernst-Einstein equation. It should therefore be noted that data obtained by using near-equilibrium methods, as in this work, cannot be directly compared with techniques which involve large oxygen activity gradients.

5.2 Effect of surface modification by acid etching

In the following section, the surface modification of the Co-free rare earth nickelate $La_2NiO_{4+\delta}$ (LNO) with acid is discussed regarding the effects on the electronic conductivity and oxygen exchange kinetics.

5.2.1 Electronic conductivity

The electronic conductivity (σ_e) was measured using a linear four-point geometry. The theoretical background of the method is described in *Chapter 3.1.1*.

The electronic conductivity of the bar-shaped sample was measured as a function of temperature and oxygen partial pressure. Within a temperature range of 600 to 800 °C and an oxygen partial pressure of 0.10 bar, the electronic conductivity is between 72 and 92 S cm^{-1}. The results of the electronic conductivity are shown in *Figure 29*.

Similar to LNCO291, the electronic conductivity of LNO declines with rising temperature, indicating a p-type electronic conduction mechanism. This was to be expected from our previous investigations [39,97] and other literature sources dealing with LNO [59,60,90,98].

The impact of etching the sample with 1 M HNO_3 on the electronic conductivity was evaluated. The same bar-shaped sample was subjected to the etching process as described in *Chapter 4.3.2*, after which σ_e was measured at 0.1 bar pO_2 between 600 and 800 °C. The results of the unetched and etched material are compared in *Figure 29*. It can be clearly seen that the surface modification has no impact on the electronic conductivity. This was to be expected, as the conductivity is a bulk property while etching is affecting only the surface. As emphasized in *Chapter 3.1.1* using *Equation* 3.1, the area of the cross-section and the distance between the voltage probes exert a pivotal influence on the electronic conductivity. Neither of these parameters was influenced by etching, since the decrease in thickness was only in the 8 – 10 µm for a 4.68 mm thick sample and since the position of the gold contacts was not changed by etching.

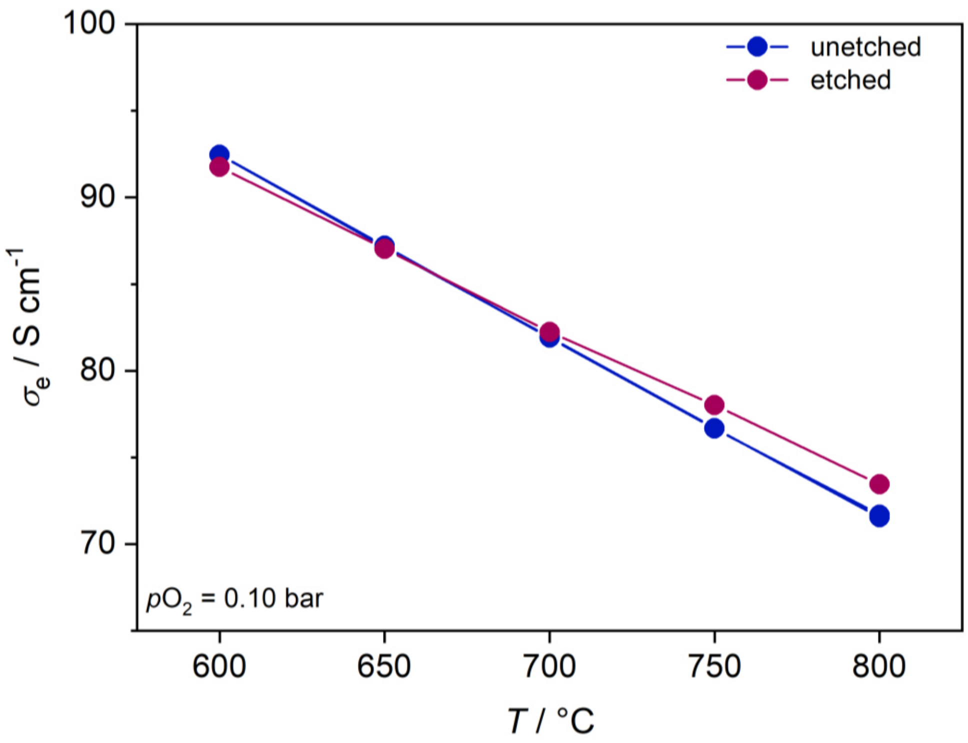

Figure 29 Electronic conductivity σ_e of the unetched and etched LNO sample as a function of temperature at 0.10 bar pO_2. Lines serve as visual guides for the eye.

5.2.2 Oxygen exchange kinetics

The oxygen exchange kinetics of $La_2NiO_{4+\delta}$ (LNO) - especially with regard to surface modification with 1 M HNO_3 - are discussed in this section.

The Arrhenius plot of the surface exchange coefficients k_{chem} of oxygen between 0.10 and 0.15 bar pO_2 and a temperature range between 600 and 800 °C of the unetched and etched samples are presented in *Figure 30*. The values of the unetched bar-sample are in line with those reported in the literature [60,95,98] and the trend, that k_{chem} increases with increasing temperature is also known for materials in this class [42,59]. The calculated activation energies are in good agreement with other published values [60,91].

A comparison of the surface exchange kinetics of oxygen of the unetched (blue) and the etched (red) bar-shaped sample of LNO in this oxygen partial pressure range reveals a clear improvement in the oxygen surface exchange rates of the material after etching with 1 M HNO_3. Moreover, a significant decrease in the activation energies can be observed. The activation energy is reduced to approximately one third of its original value (E_a = 45-46 kJ mol^{-1} for the etched and E_a = 130-134 kJ mol^{-1} for the unetched sample) as a consequence of the surface treatment.

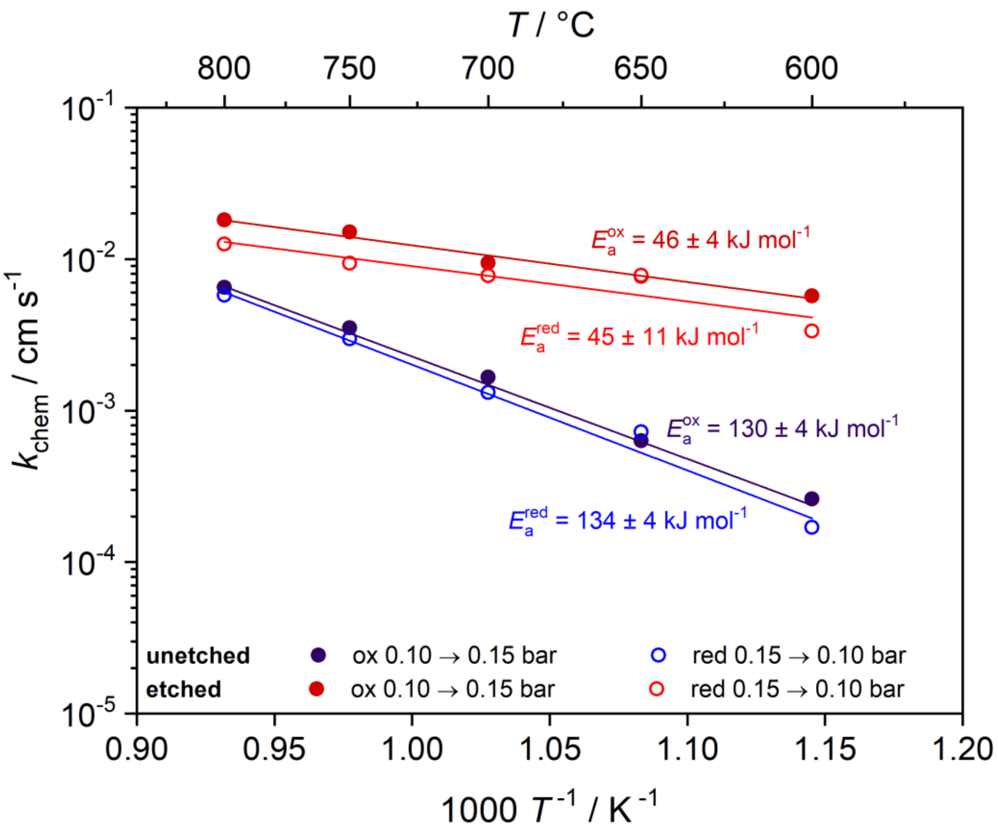

Figure 30 Arrhenius representation of chemical oxygen surface exchange coefficients k_{chem} of the unetched and etched LNO samples between 0.10 and 0.15 bar pO_2.

The chemical diffusion coefficient D_{chem} is depicted in *Figure 31* as a function of temperature and oxygen partial pressure. D_{chem} is temperature-dependent and increases with increasing temperature. This trend has already been observed in rare earth nickelates [39,97].

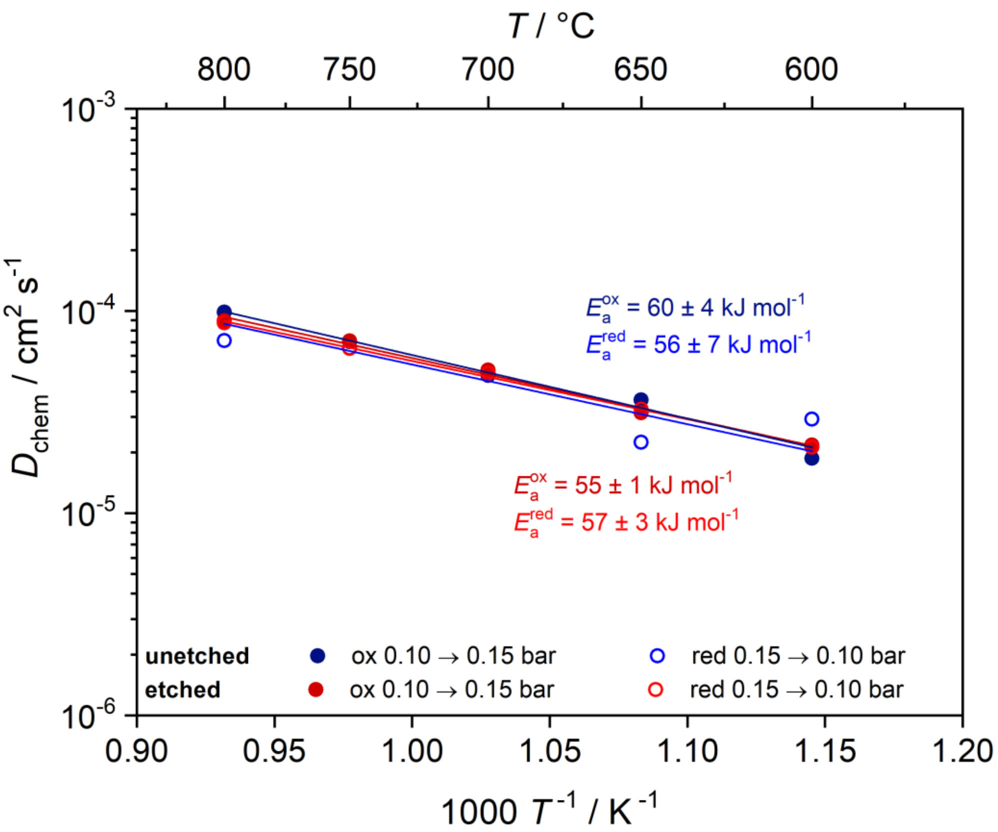

Figure 31 Arrhenius representation of chemical diffusion coefficients D_{chem} of oxygen of the unetched and etched LNO samples between 0.10 and 0.15 bar pO_2.

In contrast to the oxygen surface exchange kinetics, the surface modification has no impact on oxygen diffusion, as the D_{chem}-values and the associated activation energies of the etched and unetched samples are very close. It can be thus reasonably inferred that this is solely a surface phenomenon.

Wu et al. [72] found that a temperature-dependent decomposition process takes place on the surface of LNO, as explained in more detail in *Chapter 3.2.3*. This results in a higher activation energy for the diffusion process on the surface as compared to the bulk. Etching of the sample seems to interfere with this decomposition process as the activation energies are significantly improved. It is therefore necessary to observe the effect at a constant elevated temperature and to look more closely at the surface chemistry. *Figure 32* and *Figure 33* show the evolution of k_{chem} and D_{chem} over 30 days at 600°C and a pO_2 of 0.10 bar.

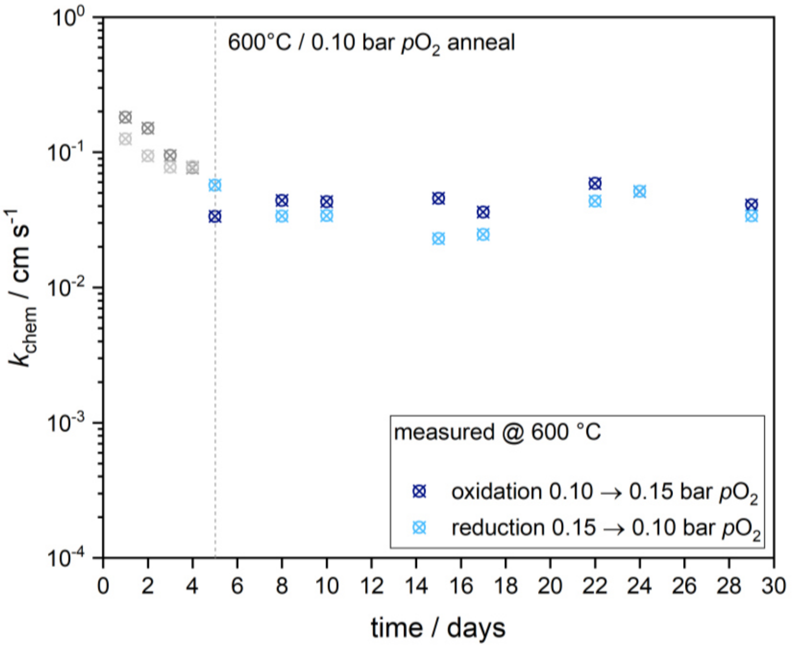

Figure 32 Long-term stability of chemical oxygen surface exchange coefficients k_{chem} of the etched sample at 600 °C and 0.10 bar pO_2. The grey data points on the left side are equivalent to the data points in Figure 30 of the etched sample.

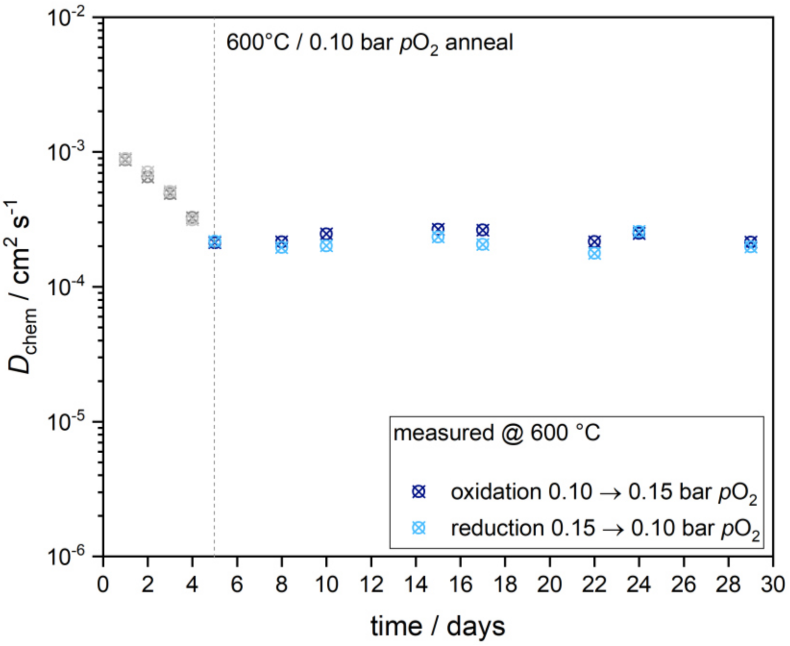

Figure 33 Long-term stability of chemical diffusion coefficients D_{chem} of oxygen of the etched sample at 600 °C and 0.10 bar pO_2. The grey data points on the left side are equivalent to the data points in Figure 31 of the etched sample.

The effect of the surface modification is irreversible, at least at 600 °C. A long-term test at 800 °C is being considered, as Wu et al. [72] also assume a temperature range between 600 and 800 °C for the surface decomposition.

5.2.3 Surface roughness

The results of the electronic conductivity (EC) and conductivity relaxation (CR) measurements clearly demonstrate that the etching of the sample is a surface effect. Consequently, further investigations were required to gain a deeper understanding of this phenomenon. *Figure 34* illustrates the surfaces of the unetched sample (top row) and the etched sample (bottom row), as observed by field-emission scanning electron microscopy (FESEM).

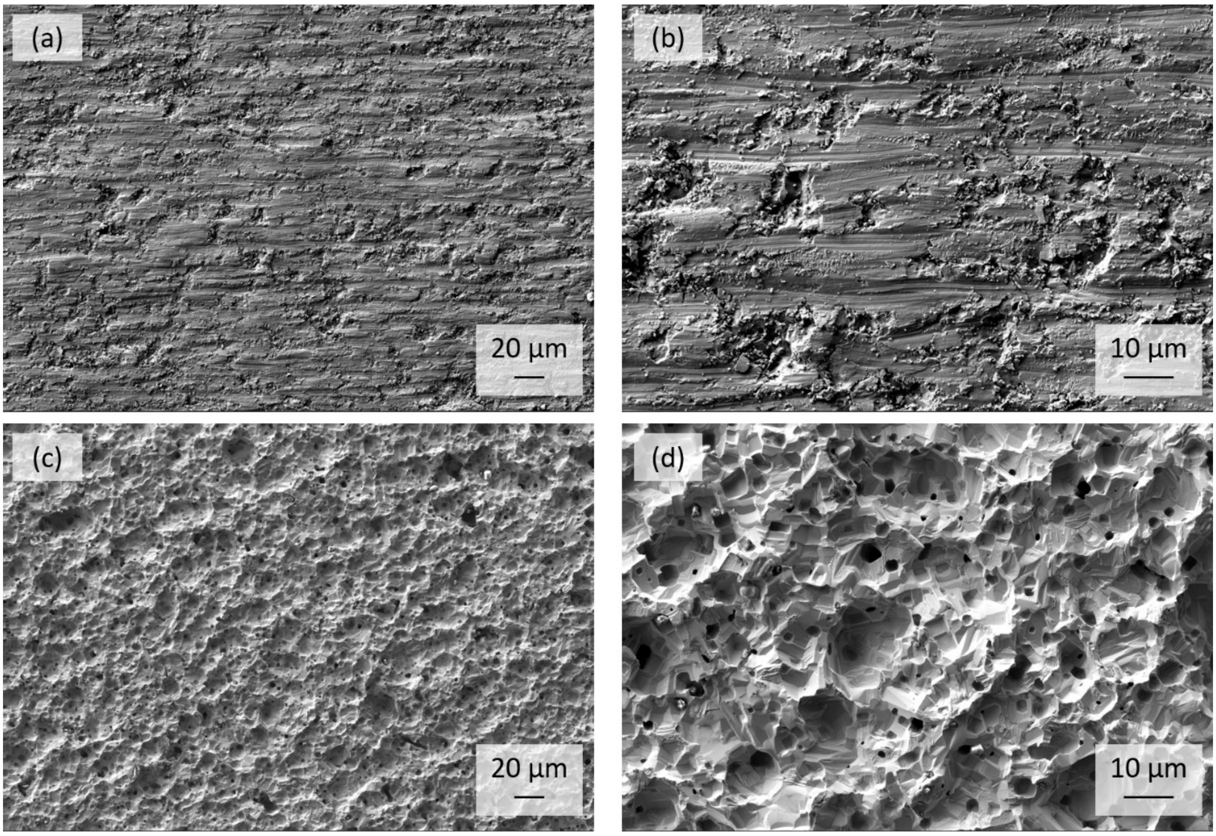

Figure 34 Secondary electron FESEM images of the unetched and unpolished sample surface (a, b) and the etched sample surface (c, d) at different magnifications.

The grooves that can be seen in SEM images of the unetched sample are caused by the diamond wire during cutting. Signs of superficial chipping by the embedded diamond particles can be seen, thereby rendering the surface structure uneven. The etching process results in the uneven removal of the surface, accompanied by the formation of a sponge-like structure in the area close to the surface. Visual comparison of the images suggests an increase in the surface area by the etching process, which might serve as a first explanation for the increase in the surface exchange rates.

In order to pursue this hypothesis further, the surface of the unetched sample and the sample etched with 1.0 M HNO_3 were examined using a laser-scanning microscope (VK-X3000, Keyence). With this technique, the samples were scanned with a laser perpendicular to the sample surface, and a multiple line measurement was taken. It is important to note, however, that not all pores could be completely captured by the laser in this way, as the 90-degree position of the laser relative to the surface of the sample could not capture all pores. The developed interfacial area ratio (*Sdr*) is defined as the percentage of the additional area that is due to the texture in comparison to a perfectly flat definition area [99]. The *Sdr*-value of a perfectly flat surface would therefore be 0.

To obtain representative results, four different areas were analyzed for each sample. In *Figure 35 Altitude color profiles of the unetched* and etched samples used to determine the interfacial area ratio (Sdr). the altitude color profiles of the unetched and etched samples used to determine the interfacial area ratio (*Sdr*) are shown. For the unetched sample, the grooves caused by the diamond wire saw are clearly visible as horizontal stripes. The *Sdr*-value of the unetched sample was used as a reference and compared against the *Sdr*-value of the etched sample. The results are summarized in *Table 9*.

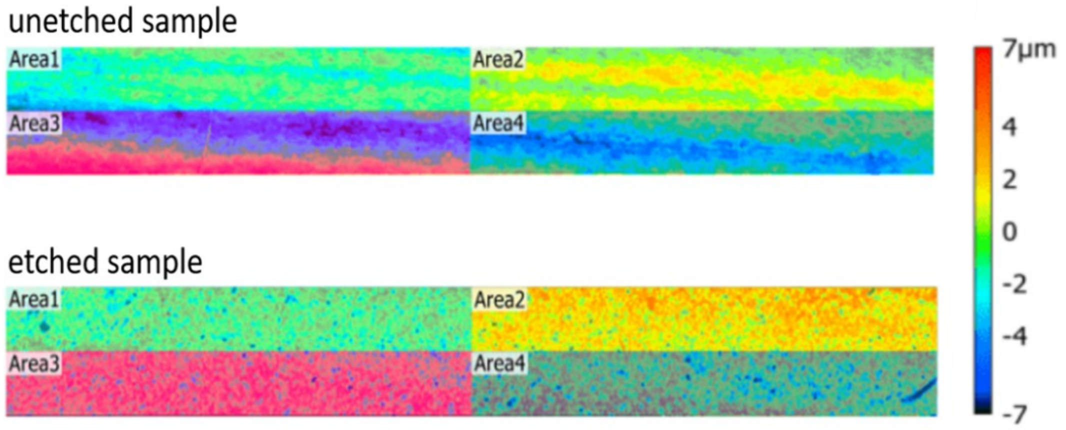

Figure 35 Altitude color profiles of the unetched and etched samples used to determine the interfacial area ratio (Sdr).

Table 9 Values of the developed interfacial area ratio (Sdr) of the unetched and etched samples.

	Area	***Sdr/%***	***average Sdr/%***
unetched sample	1	7.09	5.92 ± 1.48
	2	7.32	
	3	4.70	
	4	4.59	
etched sample	1	40.63	38.37 ± 2.61
	2	40.45	
	3	35.30	
	4	37.11	

Taking the *Sdr*-values into account, etching resulted in an increase in area from 0.528 × 0.529 to 0.607 × 0.608 cm^2. Thus, when considering the increase in surface area from a purely geometric standpoint, an increase in k_{chem} by a factor of approximately 1.3 would be expected, which is much lower than the actual observed enhancement (see *Figure 36*). This is also illustrated in the Arrhenius plot in *Figure 36*, which shows the original values of the chemical oxygen surface exchange coefficient of LNO compared to calculated values resulting from an increased surface area by a factor of 1.3.

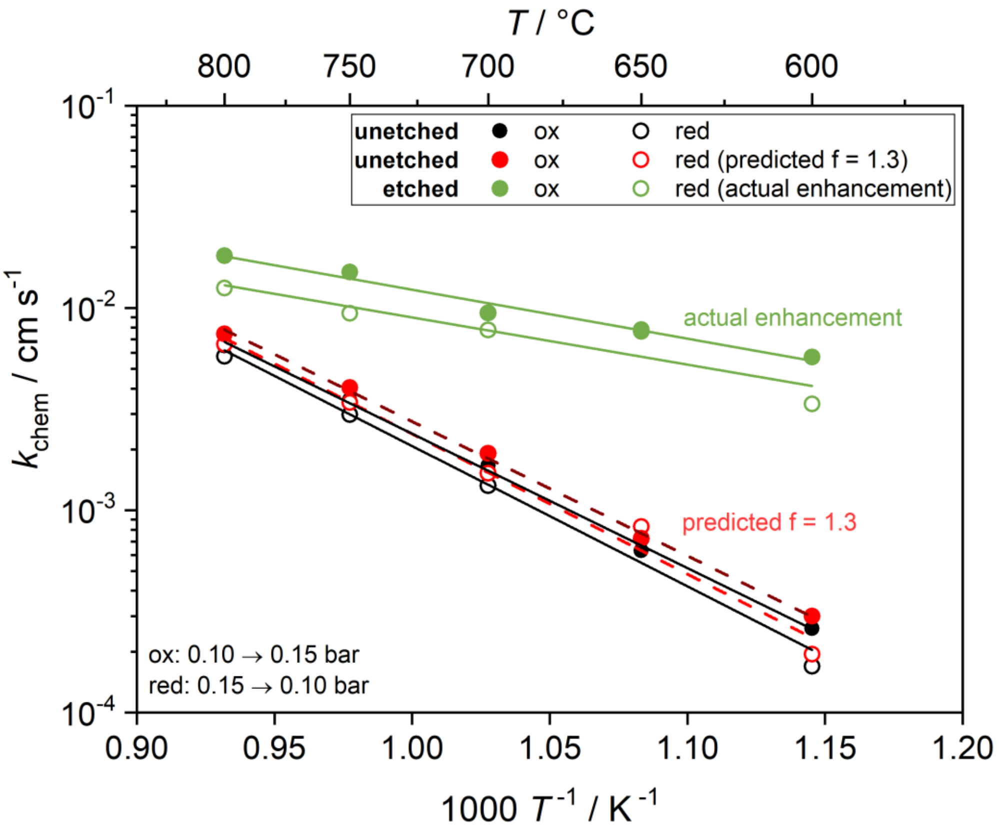

Figure 36 Arrhenius representation of chemical oxygen surface exchange coefficients k_{chem} of the etched and unetched LNO bar-sample between 0.10 and 0.15 bar pO_2 considering the increase in surface area due to etching.

As already mentioned, changes in activation energies of k_{chem} caused by etching (see *Figure 30*) also indicate that the observed effect cannot be attributed solely to an increase in surface area, as this would not change the activation energy. Therefore, the surface chemistry was analyzed in more detail, which is discussed in the following section.

5.2.4 X-ray photoelectron spectroscopy

In order to study the surface properties of LNO, the unetched and etched samples were investigated via X-ray photoelectron spectroscopy (XPS). *Figure 37* shows the X-ray photoelectron spectra of both samples in the Ni3p and La4d region.

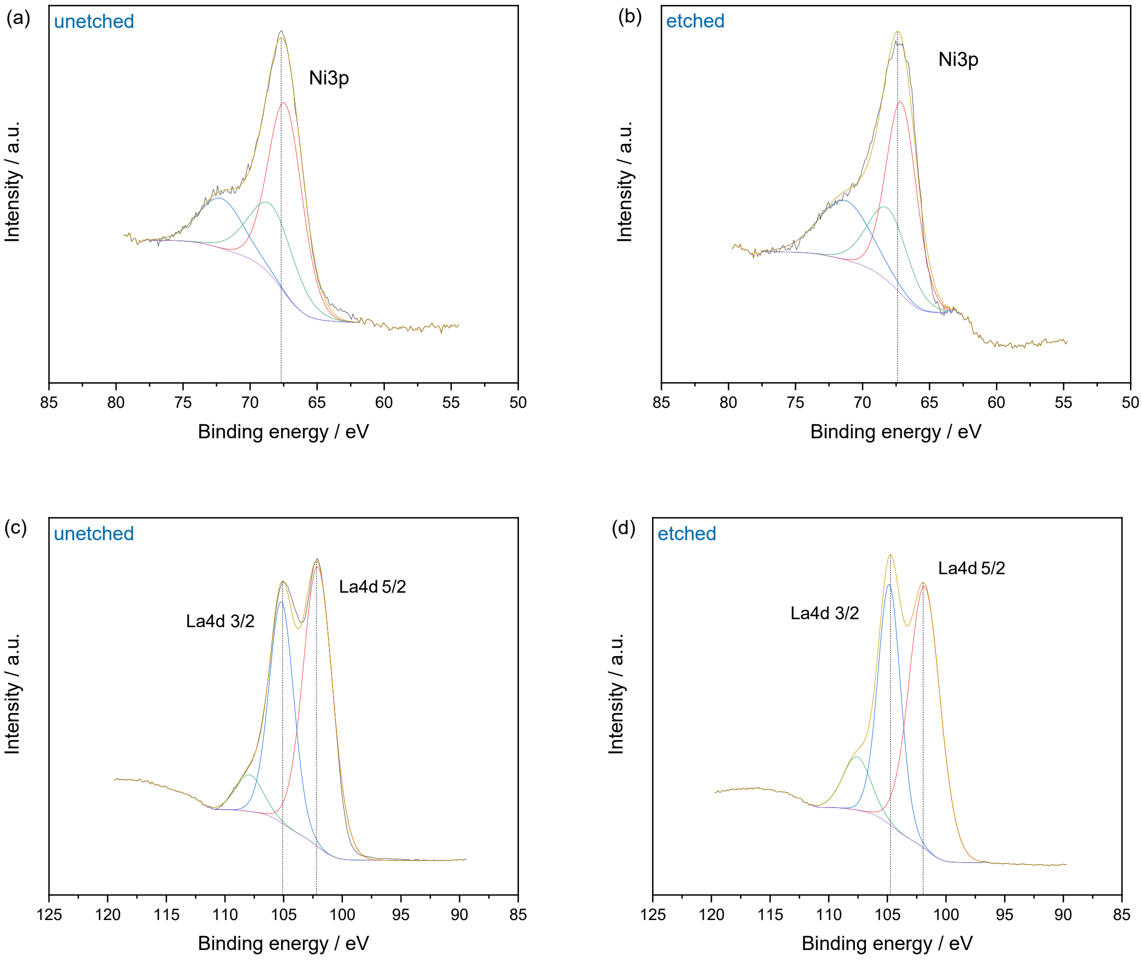

Figure 37 X-ray photoelectron spectra of Ni3p of the unetched (top, left) and the etched LNO sample (top, right) and the spectra of La4d of the unetched (bottom, left) and the etched LNO sample (bottom, right). In figures a) and b) (Ni spectra), the red and green lines correspond to the Ni3p 3/2 (red) and Ni3p 1/2 (blue) orbitals. For fitting a spin-orbit splitting of 1.0 eV an area ratio of 2:1 was used. The green line describes the shakeup peak often observed in Ni3p transition [100]. Figures c) and d) show the La4d region. The red component describes the La4d 5/2 orbital while the blue component describes La4d 3/2. A spin-orbit splitting of 3.1 eV was used for the fit with an area ratio of 3:2 in line with literature [101]. The green component with the highest binding energy could correspond to the formation of surface carbonates in air [102].

Upon examination of the atomic ratio of nickel to lanthanum, it becomes evident that etching results in a reduction of nickel on the surface, thereby creating a Ni-depleted or La-enriched phase. The atomic ratios Ni:O and La:O demonstrate an increase in oxygen content following the surface treatment with 1 M HNO_3. The element ratios are listed in *Table 10*.

Table 10 Atomic ratios of the unetched and etched LNO samples.

	peak area ratio unetched sample	***peak area ratio etched sample***	***change in peak area ratio unetched → etched***
Ni:La	7.88	7.39	-6.32 at.-%
Ni:O	9.63	11.52	+19.61 at.-%
La:O	1.22	1.56	+27.69 at.-%

Figure 38 points out that the O1s signal can be divided into two distinct peaks at approximately 528.7 eV and 531.1 eV. These peaks can be attributed to lattice oxygen (O^{2-}), with the peak at 528.7 eV corresponding to a La_2O_3 phase and the peak at 531.1 eV corresponding to the lattice oxygen in La_2NiO_4 [103–105].

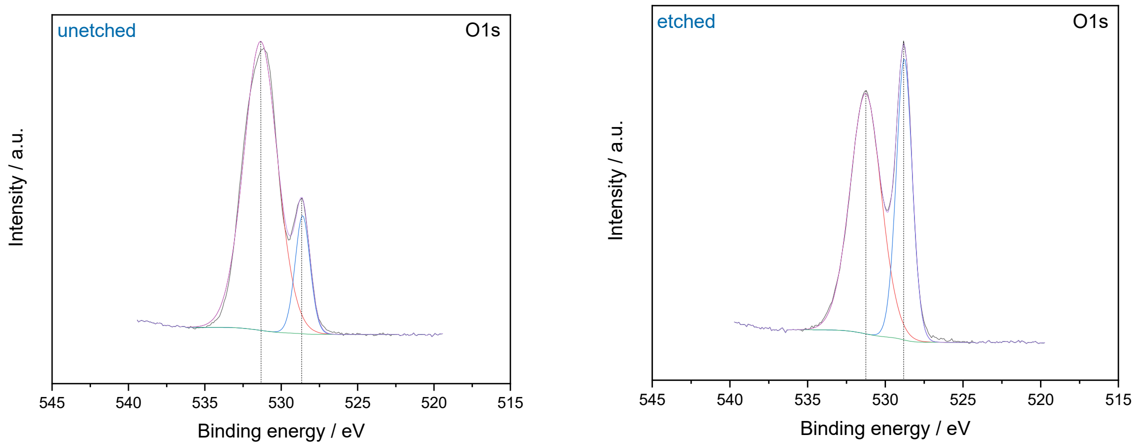

Figure 38 X-ray photoelectron spectra of O1s of the unetched (left) and the etched LNO sample (right) divided into a La_2NiO_4 (red line) and La_2O_3 component (blue line).

The relative content of lattice oxygen in La_2O_3 increases as a result of surface modification and is shown in *Table 11*. The shift towards lower binding energy indicates a lower electron affinity [106].

Table 11 Integrated peak area of the O1s peak divided into a La_2NiO_4 and La_2O_3 component.

O1s	**peak area**	
	unetched sample	**etched sample**
La_2NiO_4	26400	12233
La_2O_3	4781	7313
La_2O_3 in at.-%	**15.3**	**37.4**

5.3 Electrochemical properties

In this section, the investigated materials are discussed in an application-oriented manner. The electrochemical properties of the electrode materials are investigated by *I*-*V*-curves and electrochemical impedance spectroscopy (EIS).

First, it is investigated whether the activating effect of etching can be transferred to porous nickelate-based oxygen electrodes, thus increasing their performance. However, preliminary attempts to etch screen-printed and sintered electrodes turn out to be unsuccessful and result in partial removal or even delamination of the electrode layer [107]. In a next step it is thus attempted to modify the surface composition by means of infiltration.

For this purpose, four symmetrical cells are investigated:

- symmetrical cell #1: LNO-electrode on a CGO-electrolyte substrate
- symmetrical cell #2: LNO-electrode on a CGO-electrolyte substrate
- symmetrical cell #3: LNO-electrode infiltrated with nickel on a CGO-electrolyte substrate
- symmetrical cell #4: LNO-electrode infiltrated with lanthanum on a CGO-electrolyte substrate

As shown by XPS-analysis, etching a bar-shaped sample leads to an increased accumulation of lanthanum on the surface. In this respect, the performance of La-infiltrated electrodes (i.e. cell #4) is of particular interest.

Moreover, the performance of LNCO291 as electrode material is evaluated in a full button cell by means of *I*-*V*-curves in SOEC, solid oxide fuel cell (SOFC), and in reversible solid oxide cell (RSOC) mode. The cell test and the post-test analyses of *Chapter 5.3.2* have already been shown in Eisbacher et al. [108].

5.3.1 Symmetrical cells with $La_2NiO_{4+\delta}$-electrodes

The symmetrical cells were analyzed by means of electrochemical impedance spectroscopy (EIS). In order to compare the results, resistances were normalized with respect to the area of the oxygen electrode and are thus stated as area-specific resistance (ASR) in Ω cm^2. This was done using the following equation for the real part of the impedance.

$$Z'_{ASR} = \frac{1}{2}\,(Z' - R_0)(\frac{d^2\,\pi}{4}) \qquad 5.5$$

The resistance of the electrolyte R_0 was subtracted from the real part Z', and the resulting value was multiplied by the area of a single oxygen electrode (1.33 cm^2 / diameter of electrode is 13 mm for all cells). As the cells are symmetrical and therefore have two identical electrodes, a factor of ½ is applied to obtain the (average) contribution of a single electrode. The ASR is dependent on the temperature and the thickness of the electrolyte l:

$$R_0 = \rho(T)\,\frac{l}{A} = \frac{1}{\sigma(T)}\frac{l}{A} \qquad ASR = R_0\,A = \rho(T)\,l = \frac{l}{\sigma(T)} \qquad 5.6$$

In this context, ρ represents the electrical resistivity, while A denotes the area of the electrode. σ corresponds to the electrical conductivity in S cm^{-1}.

The normalization of the imaginary part Z'' was carried out analogously to the calculation of the area-specific resistance of the real part, after subtracting the purely inductive contribution of the setup (wires).

$$Z''_{ASR} = \frac{1}{2}\,(Z'' - 2\,\pi\,f\,L_0)(\frac{d^2\,\pi}{4}) \qquad 5.7$$

The EIS measurements were conducted between 700 and 850 °C over a frequency range of 10^{-2} to 10^{6} Hz and are depicted in *Figure 39*. To study the extent of degradation of the electrode, each series of measurements was performed thrice with an interval of approximately 24 hours. All impedance spectra were evaluated using the WinFit software (Novocontrol).

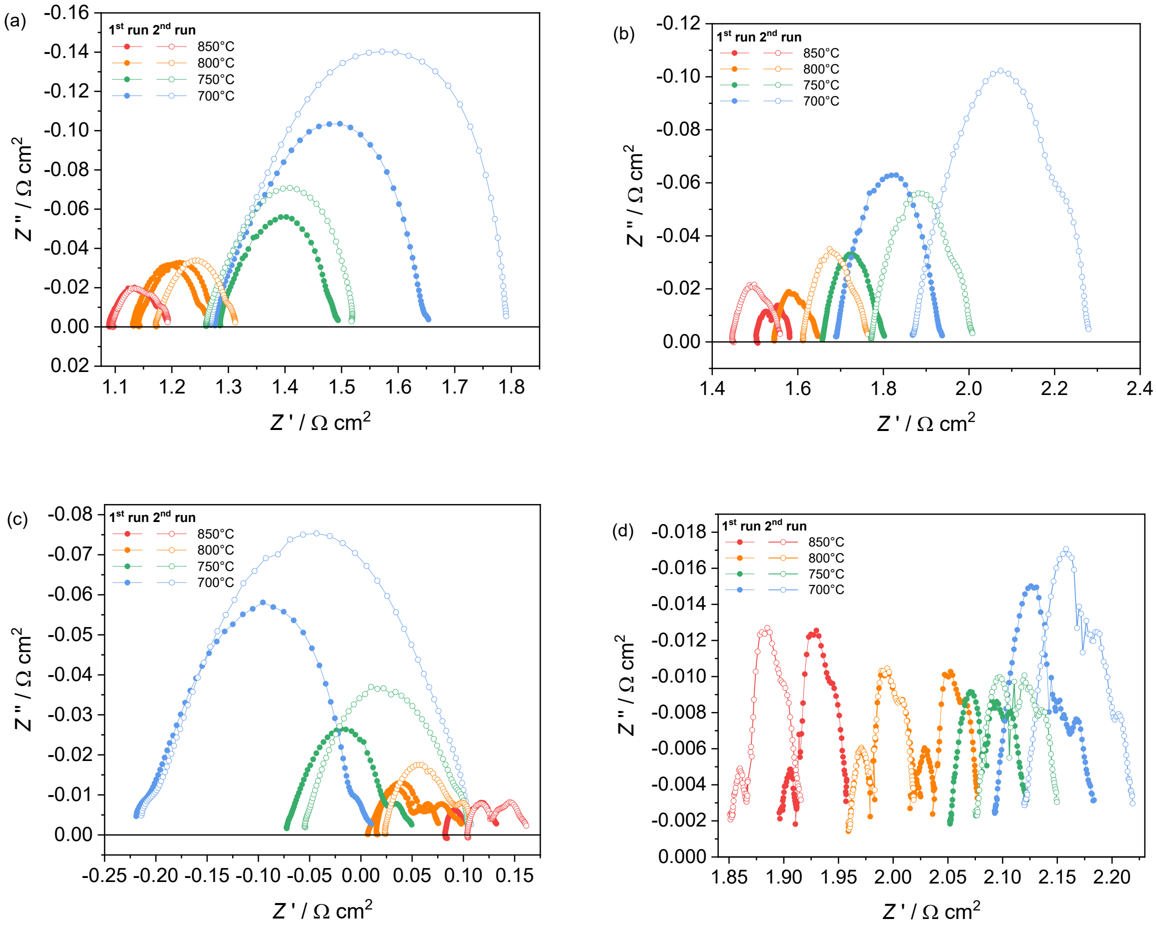

Figure 39 Nyquist plots of EIS data of cells #1-4 (a-d) at different temperatures.

Degradation can be observed for all cells. On the one hand, this is due to an increase in the polarization resistance R_{pol} and, on the other hand, a decrease in the series resistance R_{s} can be observed. The decrease in R_{s} over time might be due to the absence of a current collector layer, as the effect of decreasing R_{s} has also been observed for composite electrodes without current collector [109].

A comparative analysis of the cells is presented in *Figure 40*. *Figure 41* shows values of R_{pol} (left) and R_{s} (right) in Arrhenius representation.

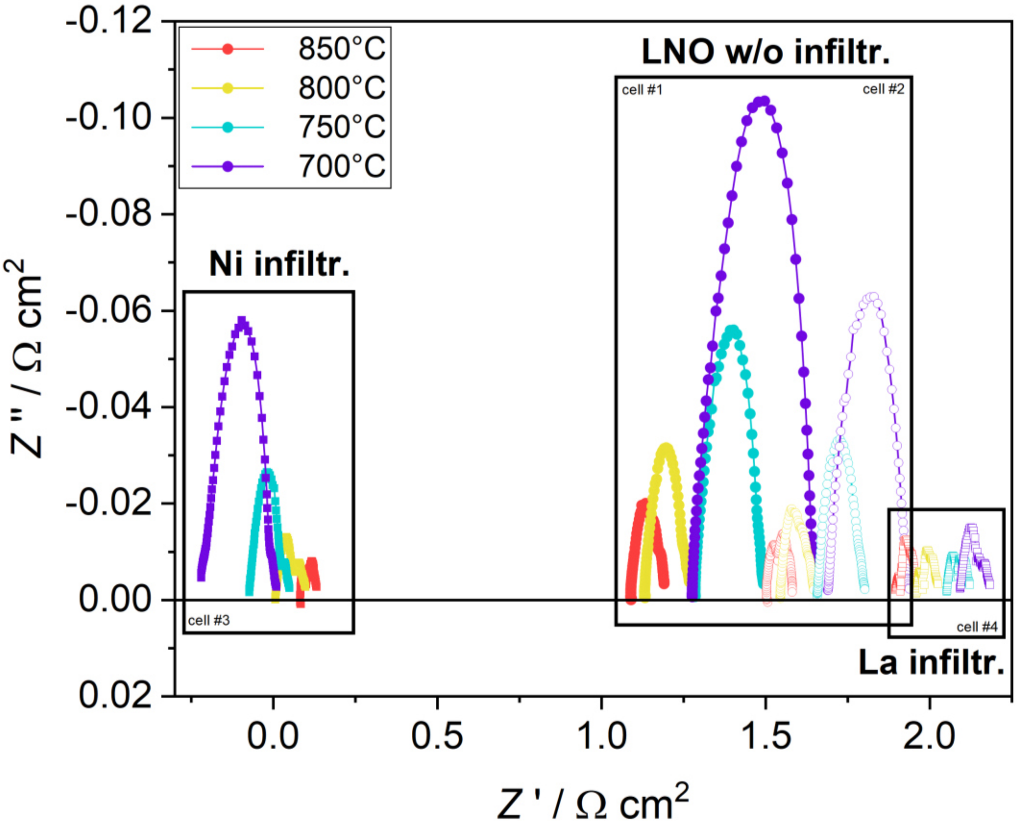

Figure 40 Comparison of the EIS results of cells #1-4 (first run) at different temperatures.

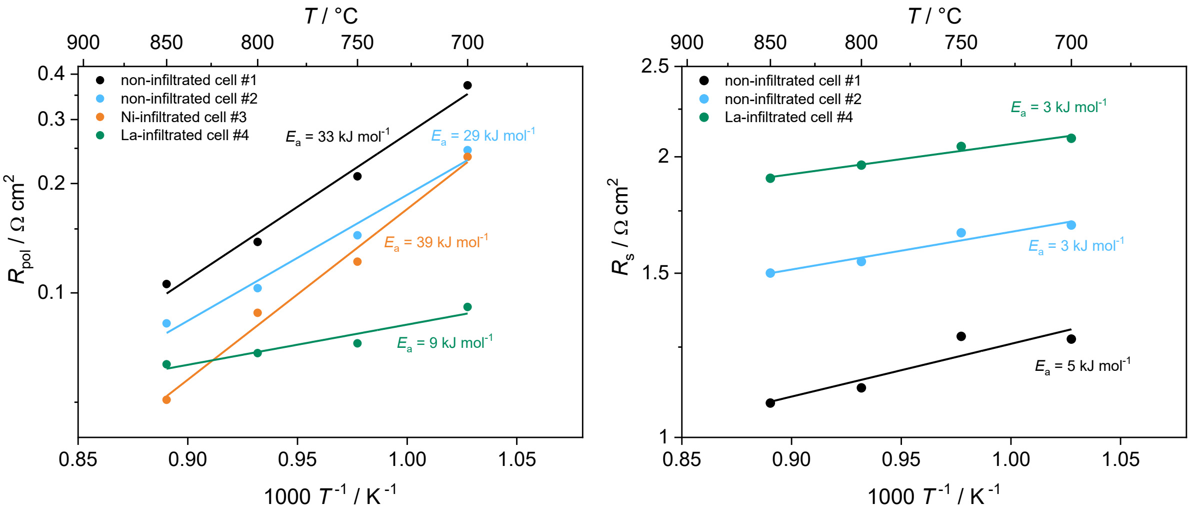

Figure 41 Arrhenius representation of R_{pol} (left) of the symmetrical cells #1-4 (first run) and R_s (right) of the symmetrical cells #1, #2 and #4 (first run). As the logarithm of negative numbers is not defined, it is not possible to provide an Arrhenius representation of R_s for the Ni-infiltrated cell #3.

It can be observed in *Figure 40* that the results of the non-infiltrated cells #1 and #2 differ considerably from each other, despite identical production and sintering procedures. This is indicative of a poor reproducibility, but it is unclear whether this originates from the cell preparation or the setup. In any case, the reproducibility might be improved by the application of a current collection layer with a significantly higher electrical conductivity than the LNO electrode.

When assessing the nickel-infiltrated cell #3, negative values of the real part Z' at temperatures below 800 °C (after subtracting the contribution of the electrolyte) can be noticed, which is of course physically not possible. A tentative explanation for this phenomenon is an effective enlargement of the electrode area resulting from the metal nitrate solution's migration beyond the electrode boundaries onto the electrolyte during infiltration. Since a complete removal of the nitrate solution from the electrolyte substrate was not possible, this area might become electrochemically active after sintering, thus enlarging the effective electrode area and reducing the electrode resistance. The reduction of the R_s with decreasing temperature also appears to be non-physical, but an explanation cannot be provided at this stage.

The impedance spectra of the lanthanum-infiltrated cell #4 feature striking differences when compared to the non-infiltrated cells. In particular, a considerable reduction in the electrode polarization resistance (R_{pol}) is evident, especially at lower temperatures. Moreover, the activation energy of R_{pol} is also significantly reduced by La-infiltration (see *Figure 41*). This agrees perfectly with results from the etching study (see *Chapter 5.2*), which suggest that La-enrichment on the surface strongly enhances the rate and reduces the activation energy of the oxygen surface exchange process – an important step in the overall electrode reaction and captured by R_{pol}. However, the overall electrode performance in dc-operation (corresponding to the low-frequency intercept of the spectra) is very poor for the La-infiltrated electrodes, which is due to a pronounced increase in the ohmic contribution R_s. This, however, might be an artifact arising from poor current collection due to the formation of an insulating layer of lanthanum oxide on the electrode surface by infiltration (see also results from SEM analyses below).

Results from post-test SEM analyses of the cross sections of the cells #1-4 are given in *Figure 42*. It can be seen that the oxygen electrodes show good adhesion to the CGO electrolyte substrate.

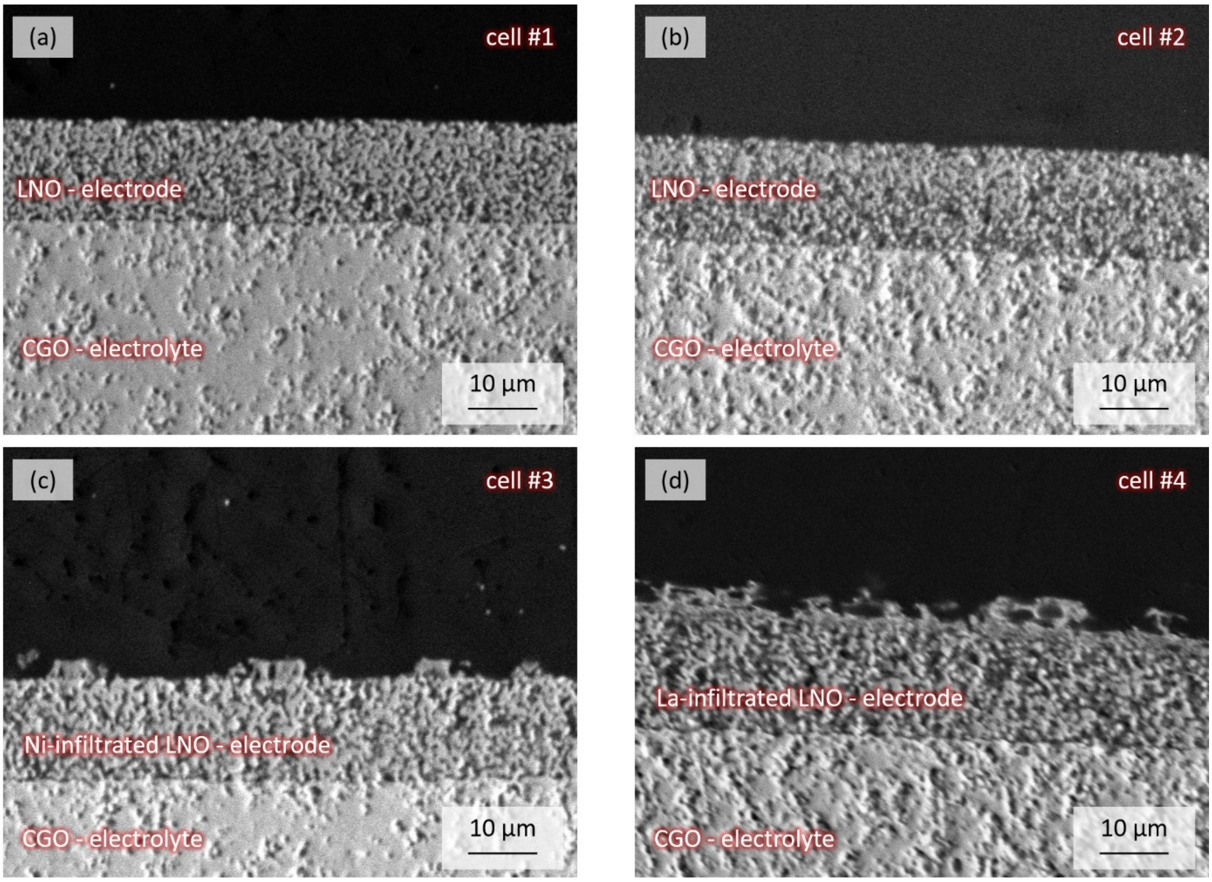

Figure 42 SEM image in BSE mode of the electrode-electrolyte interface. (a) and (b) correspond to the non-infiltrated symmetrical cells #1 and #2. The nickel-infiltrated symmetrical cell #3 is shown in (c) and image (d) corresponds to the lanthanum-infiltrated symmetrical cell #4.

Patches of NiO are visible on the surface of the Ni-infiltrated electrode (cell #3). Agglomerations can be recognized within the electrode, although the SEM images cannot be used to conclude with absolute certainty that there are NiO deposits on the inner surface of the LNO backbone. The presence of nickel oxide on the electrode surface can be discerned through the use of EDX line scans across the cross-section, as demonstrated in *Figure 43*, where it can be seen that there is more nickel (green line) on the electrode surface than in the electrode cross-section.

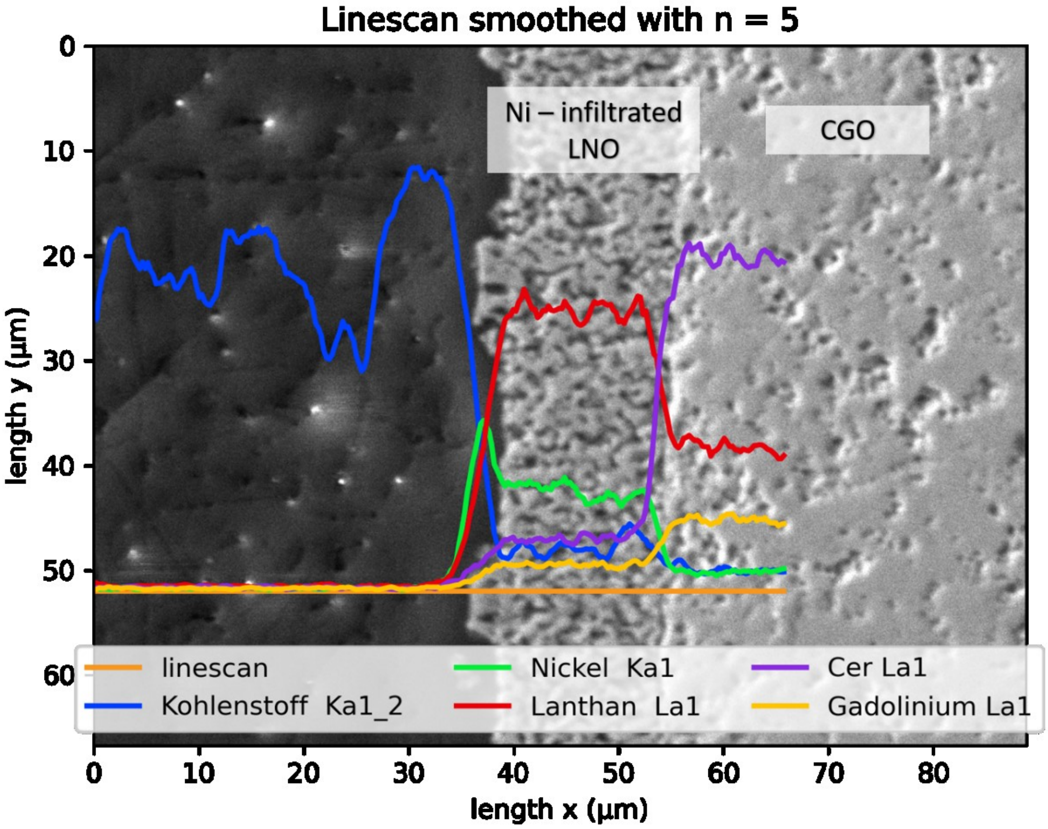

Figure 43 EDX-line scan through the Ni-infiltrated cell #3 along the orange line. The blue line shows carbon, green and red correspond to nickel and lanthanum, respectively. The violet and yellow lines refer to cerium and gadolinium, respectively.

Likewise, lanthanum was deposited on the surface of the La-infiltrated cell #4, as can be seen in *Figure 42d* and *Figure 44*.

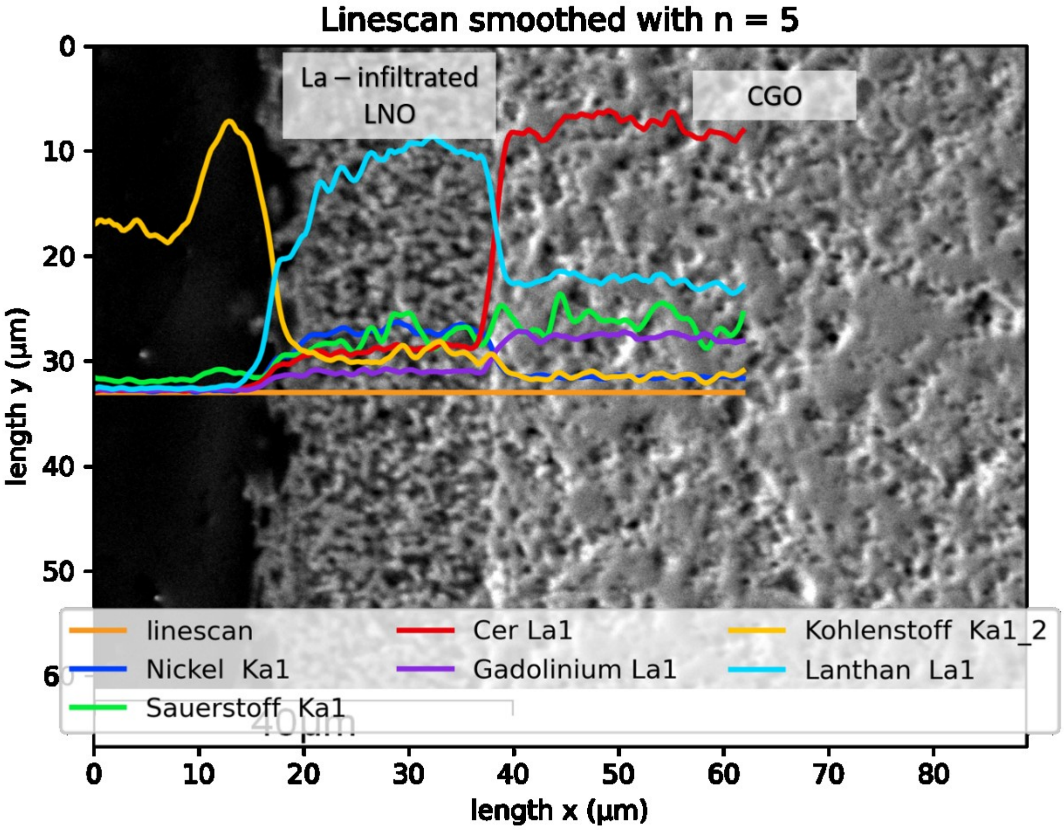

Figure 44 EDX-line scan through the La-infiltrated cell #4, along the orange line. The yellow line shows carbon, dark blue and light blue correspond to nickel and lanthanum, respectively. The red and violet lines show the cerium and gadolinium content, respectively. The oxygen signal is colored green.

Top-view SEM images of the oxygen electrodes of the non-infiltrated cells #1 and #2 in top view (*Figure 45a and b)* display a homogeneous and porous structure across the surface of the electrode. Despite the disparate performance of the cells, no differences could be discerned between the two non-infiltrated cells in the SEM post-test analysis.

In the case of the nickel-infiltrated cell #3 (*Figure 45c*), a furrowed layer is covering the LNO electrode. This layer is likely to be nickel oxide, which has a rather low electronic conductivity even at high temperatures [110]. However, as previously stated, the infiltration step results in enhanced cell performance, indicating successful deposition of nickel oxide on the electrode backbone.

For the La-infiltrated cell #4 (*Figure 45d),* a rather dense layer was formed on the surface of the electrode as a consequence of the infiltration process. This layer consists most likely of lanthanum oxide and appears to be more compact in comparison to the NiO-layer of cell #3. It is to be expected that such layer will impede the exchange of oxygen with the porous electrode structure, which makes the low polarization resistance observed in the impedance spectra of this cell is quite surprising. Lanthanum oxide can be regarded as an electrical insulator [111], a fact supported by the large ohmic contribution in the EIS spectra of the infiltrated cell.

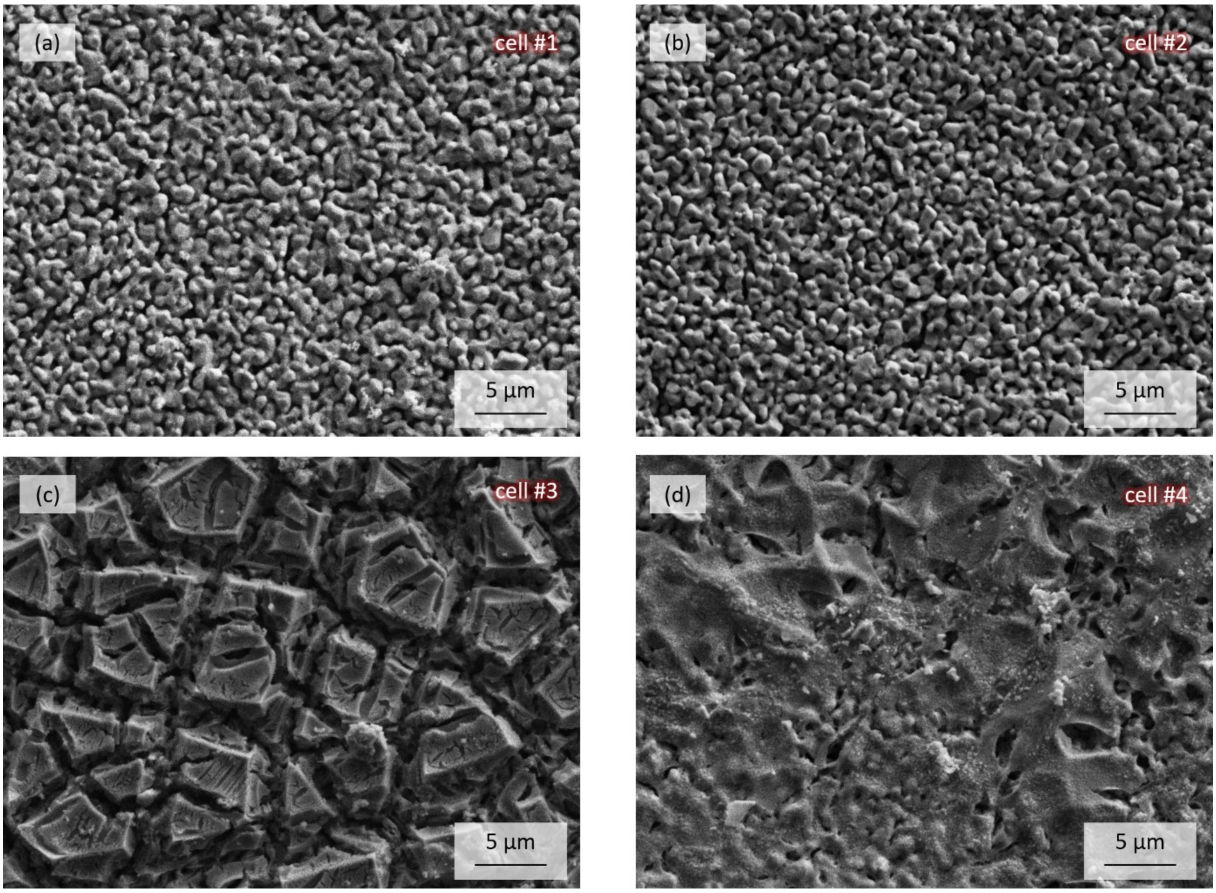

Figure 45 SEM images in SE mode of the LNO electrodes in top view. (a) and (b) correspond to the non-infiltrated symmetrical cells #1 and #2. The nickel-infiltrated electrode of symmetrical cell #3 is shown in (c) and image (d) corresponds to the lanthanum-infiltrated electrode of symmetrical cell #4.

It is important to highlight that the utilization of a dedicated current collection layer is a crucial aspect for future investigations. This approach would guarantee low contact resistance and the effective extraction of electronic current from the active electrode layer of the cell.

5.3.2 ESC-button cell with $La_2Ni_{0.9}Co_{0.1}O_{4+\delta}$-electrode

For the cell preparation, the powder was processed to an ink (65 wt.-% LNCO291) with a commercially available terpineol-based ink vehicle (fuelcellmaterials, USA). The electrode was screen-printed on an electrolyte-supported cell (ESC) substrate provided by Fraunhofer IKTS (Germany). Scandia-stabilized zirconia (ScSZ) was used as electrolyte. To avoid the formation of La-zirconate at the electrode-electrolyte interface, the cell contained a CGO-diffusion barrier layer.

Electrochemical measurements in SOFC, SOEC and RSOC mode were performed with H_2/H_2O mixtures containing between 50 and 90 vol% H_2O. In Figure 46, the *I-V* curves (SOFC, SOEC and RSOC mode) at 800 °C are shown.

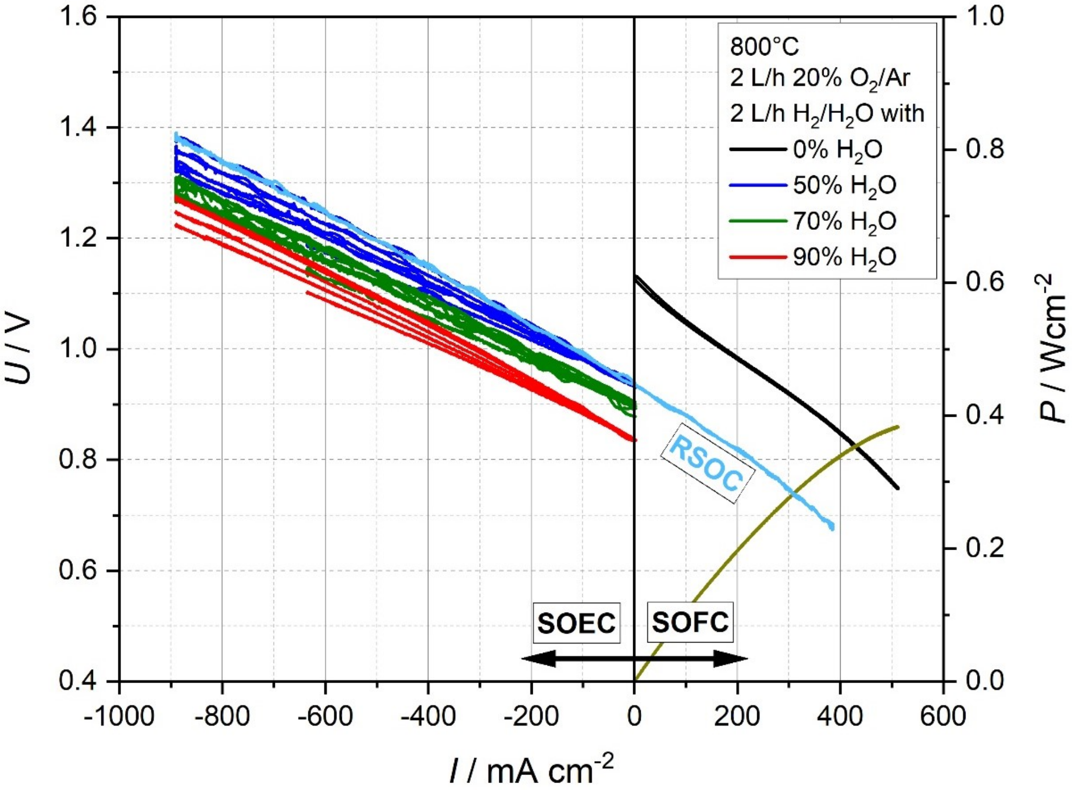

Figure 46 I-V curves (SOFC, SOEC and RSOC mode) and I-P curve corresponding to the SOFC mode of an ESC with LNCO291 oxygen electrode at 800 °C and H_2/H_2O mixtures containing between 50 and 90 vol.-% H_2O [108].

Current densities of up to -900 mA cm^{-2} were applied in SOEC mode, and up to 500 mA cm^{-2} in SOFC operation. At 800 °C and 50 vol% H_2O, the cell behaves completely reversible (RSOC mode). The

ASR (area specific resistance) values were calculated from the *I-V* slopes. The ASR in the electrolyzer mode is lower than in the fuel cell mode (ASR_{SOEC} ~0.50 Ω cm^2 over the whole SOEC range vs. ASR_{SOFC} ~0.6 Ω cm^2 at 400 mA cm^{-2}). It is suggested that at high current densities in SOEC mode a large interstitial oxygen concentration is built up in nickelate electrodes, which may improve the mass transport of oxygen [112,113].

The electrode microstructure is shown in *Figure 47* (left), which gives a top view image of the screen-printed electrode sintered for 2 h at 1100 °C. The electrode has a thickness of approximately 25 µm. The cross-section image of the electrode-electrolyte interface (*Figure 47*, right) confirms good adhesion between both layers.

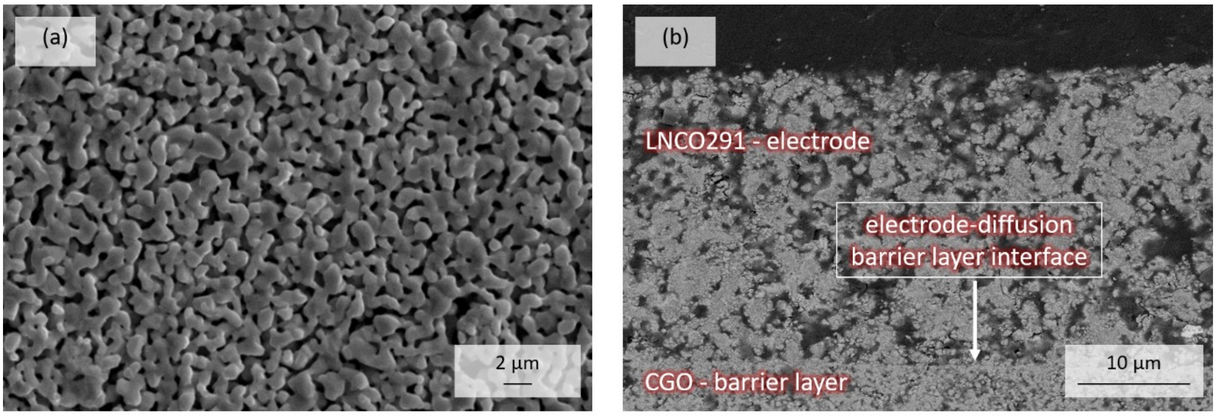

Figure 47 SEM image in SE mode of a screen-printed LNCO291 electrode after sintering for 2 h at 1100 °C in top view (a) and cross-section SEM image in BSE mode of the electrode-diffusion barrier layer interface (b) [108].

Based on the results of the *I-V*-curves and SEM-images, it can be stated that LNCO291 may be considered a promising oxygen electrode material for application in solid oxide cells. However, further investigations into the long-term stability - especially with regard to application in SOECs - should be conducted in future research, as degradation of the oxygen electrode is an important factor in limiting the lifetime of cells and stacks.

6 SUMMARY AND CONCLUSIONS

Within this work, the K_2NiF_4-type rare earth nickelate $La_2NiO_{4+\delta}$ (LNO) was analyzed with regard to fundamental material properties, especially oxygen exchange kinetics and electrochemical properties relevant for application as oxygen electrode in SOECs. The effect of partial substitution of nickel with 10 % cobalt on the B-site (see Eisbacher-Lubensky et al. [39]), as well as the effect of surface modification by acid etching with 1 M HNO_3 were evaluated.

LNO and the cobalt-substituted analogue $La_2Ni_{0.9}Co_{0.1}O_{4+\delta}$ (LNCO291) were synthesized via the citric acid-EDTA sol-gel method. X-ray powder diffraction and Rietveld refinement provided information on phase purity, lattice parameters and atomic positions of both materials.

A comprehensive characterization of the material properties of LNCO291 at varying oxygen partial pressures and temperatures was conducted through the utilization of thermogravimetry and dilatometry, in addition to electronic conductivity and dc-conductivity relaxation measurements. The thermal expansion coefficient of LNCO291 ranges between 13.4×10^{-6} and 14.0×10^{-6} K^{-1} within the oxygen partial pressure range $0.001 \leq pO_2/\text{bar} \leq 1$ between 100 and 900 °C. The values are in good agreement with those of LNO. With regard to the application in SOCs, however, it is of particular importance that the TECs match those of the common solid electrolyte materials used in SOCs, which is the case here. The oxygen non-stoichiometry is significantly increased by the substitution of nickel with 10 % cobalt. The ionic conductivity of the oxygen in LNCO291 was calculated using the Nernst-Einstein equation. A comparison of the values of LNCO291 with those of LNO reveals a good degree of agreement between the two sets of results. Furthermore, the self-surface exchange coefficient and the self-diffusion coefficient of oxygen were determined using the thermodynamic factor of oxygen and the oxygen exchange kinetic parameters. These results are also consistent with those reported in the literature for the Co-free rare earth nickelate. It is important to note, however, that the literature data obtained using the analogue measurement technique is consistent with the present results, in contrast to data determined using other measurement techniques.

The investigation of the chemical diffusion coefficients of oxygen indicates that neither the substitution of nickel with 10 % cobalt nor the surface modification with acid exerts any influence on D_{chem}. The situation is different with regard to the surface exchange coefficient of oxygen k_{chem}. Both LNCO291 and the etched LNO demonstrate enhanced surface exchange kinetics. As shown in *Figure 48*, the effects lead to higher k_{chem} values and reduce the activation energy.

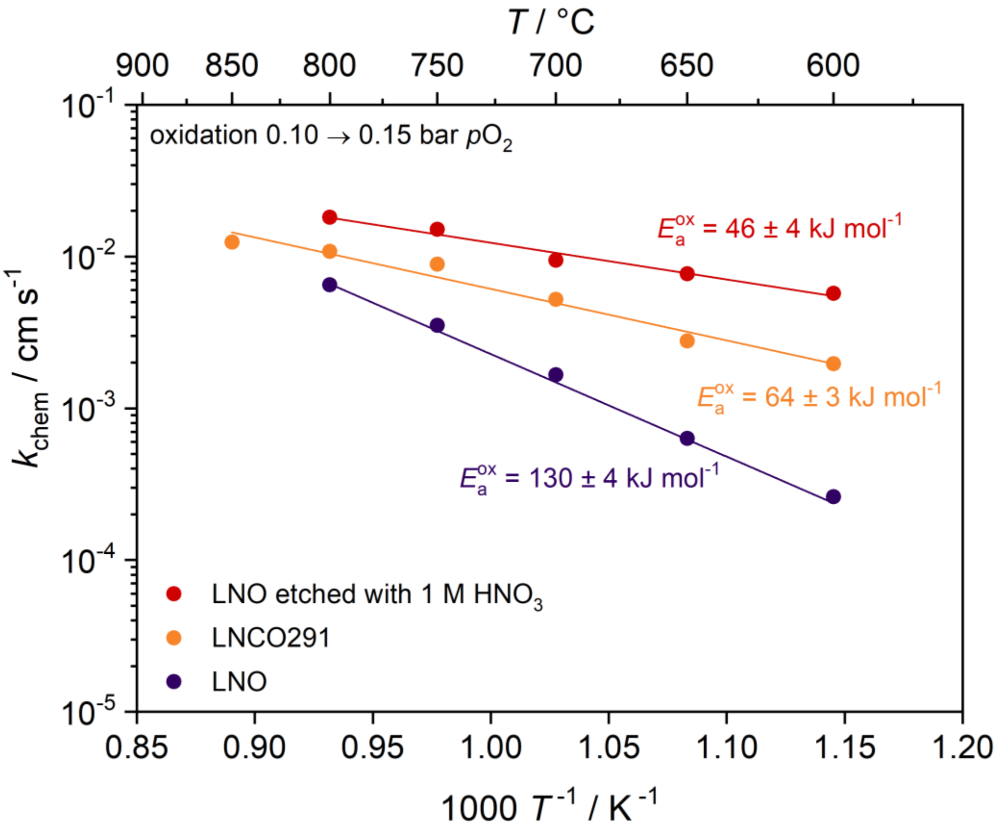

Figure 48 Comparison of the surface exchange coefficients k_{chem} of LNCO291 (yellow) [39], LNO (blue) and LNO etched with 1 M HNO_3 (red) as a function of temperature at 0.10 – 0.15 bar pO_2. The activation energies were calculated by linear regression analysis of the data in Arrhenius representation.

In evaluating the two effects, it is important to note that the surface modification with HNO_3 has the additional benefit of further improving the surface exchange kinetics. This is evidenced by a higher value for k_{chem}, as well as an even lower activation energy (LNCO291: E_a = 64 kJ mol^{-1}; LNO etched with 1 M HNO_3: E_a = 46 kJ mol^{-1}). In order to rule out the possibility that the significant enhancement in oxygen exchange kinetics is solely attributable to the increase in the surface area through etching, the surface roughness was assessed. The findings indicated, however, that this variable is not a primary determinant. In order to obtain deeper insights into the surface chemistry, the unetched and etched LNO was also analyzed using X-ray photoelectron spectroscopy. The results indicate the formation of a nickel-depleted phase, presumably La_2O_3, on the surface. Further investigations of the surface with high lateral resolution, for example transmission electron microscopy (TEM), could provide additional insights.

The electronic conductivity of LNCO291 between 600 and 850 °C at an oxygen partial pressure of 0.10 bar lies between 58 and 70 S cm^{-1}, which is lower than that of LNO. The surface treatment, however, has no influence on the values of the electronic conductivity, as illustrated in *Figure 49*.

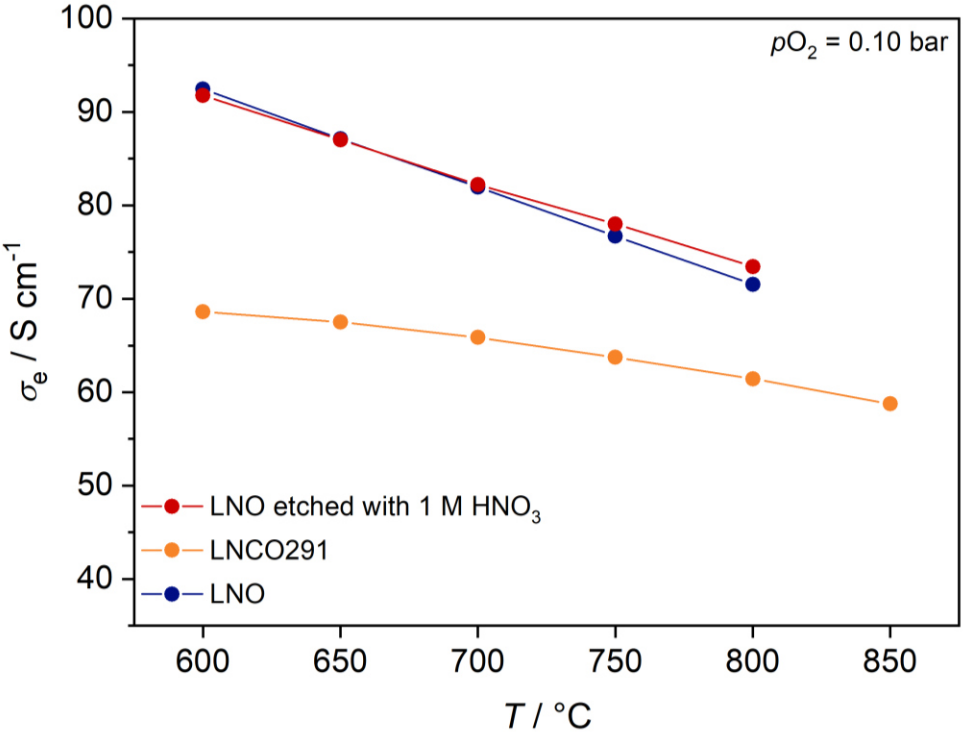

Figure 49 Comparison of the electronic conductivity σ_e of LNCO291 (yellow) [39], LNO (blue) and LNO etched with 1 M HNO_3 (red) as a function of temperature at 0.10 bar pO_2. Lines serve as visual guides for the eye.

Furthermore, symmetrical cells were produced with sol-gel wet infiltrated LNO electrodes to assess their viability as oxygen electrodes in SOECs via EIS. The tests carried out showed that infiltration with nickel resulted in an enhancement in cell performance. An infiltration test with lanthanum showed the opposite trend. Finally, it should be noted that the use of a dedicated current collector layer is imperative in future investigations, as it would ensure low contact resistance and efficient extraction of the electronic current from the active electrode layer of the cell. This is especially important for electrode materials with moderate electronic conductivity, such as nickelates. In order to facilitate future work, it is also essential to gain a more comprehensive understanding of the infiltration technique itself and further optimize the infiltration procedure. The utilization of templates for wet infiltration may prevent the solution from spilling over onto the electrolyte, thus coating some parts of the electrolyte substrate with poorly defined layers which can influence the cell performance. Alternatively, the diameter of the electrode could be increased, thus leaving a smaller fraction of the electrolyte substrate open for contamination with the infiltration solution. Infiltration in a vacuum could facilitate the absorption of the stock solution into the porous structure, which would result in a more even distribution and enhanced adhesion of the infiltration material.

An LNCO291 oxygen electrode, which was applied to an ESC button cell, demonstrated excellent adhesion to the electrolyte, as well as promising performance in SOEC, SOFC and RSOC mode [108]. Therefore, LNCO291 may be considered a promising material for application as an oxygen electrode material in solid oxide cells. Further results of rare earth nickelates, which were analyzed in the context of the dissertation, demonstrated that the substitution of nickel with 10 % cobalt on the B-site leads to an improvement in cell performance [108].

7 REFERENCES

7.1 Literature

[1] Ibrahim H., Ilinca A., Perron J., Energy storage systems - characteristics and comparisons, Renewable and Sustainable Energy Reviews 12 (2008) 1221–1250. https://doi.org/10.1016/j.rser.2007.01.023.

[2] Ni M., Leung M., Leung D., Technological development of hydrogen production by solid oxide electrolyzer cell (SOEC), International Journal of Hydrogen Energy 33 (2008) 2337–2354. https://doi.org/10.1016/j.ijhydene.2008.02.048.

[3] Garche J., Jürissen L., Applications of fuel cell technology: status and perspectives, Electrochemical Society Interface 24 (2015) 39–43. https://doi.org/10.1149/2.F02152if.

[4] Hansen J. B., Solid oxide electrolysis - a key enabling technology for sustainable energy scenarios, Faraday discussions 182 (2015) 9–48. https://doi.org/10.1039/c5fd90071a.

[5] Ebbesen S. D., Jensen S. H., Hauch A., Mogensen M. B., High temperature electrolysis in alkaline cells, solid proton conducting cells, and solid oxide cells, Chemical Reviews 114 (2014) 10697–10734. https://doi.org/10.1021/cr5000865.

[6] Wolf S. E., Winterhalder F. E., Vibhu V., de Haart L. G. J., Guillon O., Eichel R.-A., Menzler N., Solid oxide electrolysis cells – current material development and industrial application, Journal of Materials Chemistry A (2023). https://doi.org/10.1039/D3TA02161K.

[7] Zheng Y., Wang J., Yu B., Zhang W., Chen J., Qiao J., Zhang J., A review of high temperature co-electrolysis of H_2O and CO_2 to produce sustainable fuels using solid oxide electrolysis cells (SOECs): advanced materials and technology, Chemical Society Reviews 46 (2017) 1427–1463. https://doi.org/10.1039/c6cs00403b.

[8] Golkhatmi S. Z., Asghar M. I., Lund P. D., A review on solid oxide fuel cell durability: latest progress, mechanisms, and study tools, Renewable and Sustainable Energy Reviews 161 (2022) 112339. https://doi.org/10.1016/j.rser.2022.112339.

[9] Lenser C., Udomsilp D., Menzler N. H., Holtappels P., Fujisaki T., Kwati L., Matsumoto H., Sabato A. G., Smeacetto F., Chrysanthou A., Molin S., Solid oxide fuel and electrolysis cells, advanced ceramics for energy conversion and storage (2020) 387–547. https://doi.org/10.1016/B978-0-08-102726-4.00009-0.

[10] Wehrle L., Schmider D., Dailly J., Banerjee A., Deutschmann O., Benchmarking solid oxide electrolysis cell-stacks for industrial power-to-methane systems via hierarchical multi-scale modelling, Applied Energy 317 (2022) 119143. https://doi.org/10.1016/j.apenergy.2022.119143.

[11] Tucker M. C., Progress in metal-supported solid oxide fuel cells: a review, Journal of Power Sources 195 (2010) 4570–4582. https://doi.org/10.1016/j.jpowsour.2010.02.035.

[12] Zhu B., Albinsson I., Andersson C., Borsand K., Nilsson M., Mellander B.-E., Electrolysis studies based on ceria-based composites, Electrochemistry Communications 8 (2006) 495–498. https://doi.org/10.1016/j.elecom.2006.01.011.

[13] Mahato N., Banerjee A., Gupta A., Omar S., Balani K., Progress in material selection for solid oxide fuel cell technology: a review, Progress in Materials Science 72 (2015) 141–337. https://doi.org/10.1016/j.pmatsci.2015.01.001.

[14] Singhal S. C. K., Kendall K., High temperature SOFCs: fundamentals design and applications, Elsevier, 2003. https://doi.org/10.1016/B978-1-85617-387-2.X5016-8. 1856173879.

[15] Kröger F. A., Stieltjes F. H., Vink H. J., Thermodynamics and formulation of reactions involving imperfections in solids, Philips Research Reports 14 (1959) 557–601.

[16] Zhao T. S., Ni M., Solid oxide fuel cells: From materials to system modeling, RSC Publishing, Cambridge, 2013. https://doi.org/10.1039/9781849737777. 978-1-84973-654-1.

[17] Eguchi K., Hatagishi T., Arai H., Power generation and steam electrolysis characteristics of an electrochemical cell with a zirconia- or ceria-based electrolyte, Solid State Ionics 86-88 86-88 (1996) 1245–1249. https://doi.org/10.1016/0167-2738(96)00295-0.

[18] Prakash S. B., Kumar S. S., Aruna S. T., Properties and development of Ni/YSZ as an anode material in solid oxide fuel cell: a review, Renewable and Sustainable Energy Reviews (2014) 149–179. https://doi.org/10.1016/j.rser.2014.04.043.

[19] Shaikh S. P. S., Muchtar A., Somalu M. R., A review on the selection of anode materials for solid-oxide fuel cells, Renewable and Sustainable Energy Reviews (2015) 1–8. https://doi.org/10.1016/j.rser.2015.05.069.

[20] Bidrawn F., Kim G., Corre G., Irvine J. T. S., Vohs J. M., Gorte R. J., Efficient reduction of CO_2 in a solid oxide electrolyzer, Electrochemical and Solid-State Letters 11 (2008) B167. https://doi.org/10.1149/1.2943664.

[21] Suzuki T., Awano M., Jasinki P., Petrovsy V., Anderson H., Composite (La, Sr)MnO_3–YSZ cathode for SOFC, Solid State Ionics 177 (2006) 2071–2074. https://doi.org/10.1016/j.ssi.2005.12.016.

[22] Kong W., Zhang M., Han Z., Zhang Q., A theoretical model for the triple phase boundary of solid oxide fuel cell electrospun electrodes, Applied Sciences 9 (2019) 493. https://doi.org/10.3390/app9030493.

[23] Ishihara T. (Ed.), Perovskite oxide for solid oxide fuel cells, Springer-Verlag US, Boston, MA, 2009. https://doi.org/10.1007/978-0-387-77708-5.

[24] Shao Z., Tadé M. O. (Eds.), Intermediate-temperature solid oxide fuel cells: Materials and Applications, Springer, Berlin, Heidelberg, 2016. https://doi.org/10.1007/978-3-662-52936-2.

[25] Bucher E., Sitte W., Defect chemical analysis of the electronic conductivity of strontium-substituted lanthanum ferrite, Solid State Ionics 173 (2004) 23–28. https://doi.org/10.1016/j.ssi.2004.07.047.

[26] Preis W., Bucher E., Sitte W., Oxygen exchange kinetics of $La_{0.4}Sr_{0.6}FeO_{3-\delta}$ by simultaneous application of conductivity relaxation and carrier gas coulometry, Solid State Ionics 175 (2004) 393–397. https://doi.org/10.1016/j.ssi.2003.12.045.

[27] Simner S. P., Shelton J. P., Anderson M. D., Stevenson J. W., Interaction between La(Sr)FeO_3 SOFC cathode and YSZ electrolyte, Solid State Ionics 161 (2003) 11–18. https://doi.org/10.1016/S0167-2738(03)00158-9.

[28] Y. Cheng, Oh T.-S., Wilson R., Gorte R. J., Vohs J. M., An investigation of LSF-YSZ conductive scaffolds for infiltrated SOFC cathodes, Journal of The Electrochemical Society 164 (2017) F525-F529. https://doi.org/10.1149/2.0531706jes.

[29] Ullmann H., Trofimenko N., Tietz F., Stöver D., Ahmad-Khanlou A., Correlation between thermal expansion and oxide ion transport in mixed conducting perovskite-type oxides for SOFC cathodes, Solid State Ionics 138 (2000) 79–90. https://doi.org/10.1016/S0167-2738(00)00770-0.

[30] Armstrong E. N., Duncan K. I., Oh D .J., Weaver J. F., Wachsman E. D., Determination of surface exchange coefficients of LSM, LSCF, YSZ, GDC constituent materials in composite SOFC cathodes, Journal of The Electrochemical Society (2011) 492–499.

[31] Beez A., Yin X., Menzler N. H., Spatschek R., Bram M., Insight into the reaction mechanism of $(La_{0.58}Sr_{0.40})(Co_{0.20}Fe_{0.80})O_{3-\delta}$ cathode with volatile chromium species at high current density in a solid oxide fuel cell stack, Journal of The Electrochemical Society 164 (2017) 3028–3034. https://doi.org/10.1149/2.0051710jes.

[32] Kilner J. A., Shaw C.K.M., Mass transport in $La_2Ni_{1-x}Co_xO_{4+\delta}$ oxides with the K_2NiF_4 structure, Solid State Ionics 154-155 (2002) 523–527. https://doi.org/10.1016/S0167-2738(02)00506-4.

[33] Egger A., Schrödl N., Gspan C., Sitte W., $La_2NiO_{4+\delta}$ as electrode material for solid oxide fuel cells and electrolyzer cells, Solid State Ionics 299 (2017) 18–25. https://doi.org/10.1016/j.ssi.2016.10.002.

[34] Chauveau F., Mougin J., Bassat J. M., Mauvy F., Grenier J. C., A new anode material for solid oxide electrolyser: the neodymium nickelate $Nd_2NiO_{4+\delta}$, Journal of Power Sources 195 (2010) 744–749. https://doi.org/10.1016/j.jpowsour.2009.08.003.

[35] Montenegro-Hernández A., Vega-Castillo J.E., Caneiro A., Mogni L., Effects of neodymium doping on oxygen reduction activity in $Pr_{2-x}Nd_xNiO_{4+\delta}$ cathodes, Solid State Ionics 347 (2020) 115093. https://doi.org/10.1016/j.ssi.2019.115093.

[36] Antonova E. P., Khodimchuk A. V., Tropin E. S., N.M. Porotnikova, Farlenkov A. S., Vlasov M. I., Ananyev M. V., Influence of modifying additives on electrochemical performance of $La_2NiO_{4+\delta}$-based oxygen electrodes, Solid State Ionics 346 (2020) 115215. https://doi.org/10.1016/j.ssi.2019.115215.

[37] Vibhu V., Vinke I. C., Eichel R.-A., de Haart L. G. J., Cobalt substituted $Pr_2Ni_{1-x}Co_xO_{4+\delta}$ (x = 0, 0.1, 0.2) oxygen electrodes: impact on electrochemical performance and durability of solid oxide electrolysis cells, Journal of Power Sources 482 (2021) 228909. https://doi.org/10.1016/j.jpowsour.2020.228909.

[38] Vibhu V., Vinke I. C., Eichel R.-A., Bassat J.-M., de Haart L. G. J., $La_2Ni_{1-x}Co_xO_{4+\delta}$ (x = 0.0, 0.1 and 0.2) based efficient oxygen electrode materials for solid oxide electrolysis cells, Journal of Power Sources 444 (2019) 227292. https://doi.org/10.1016/j.jpowsour.2019.227292.

[39] Eisbacher-Lubensky S., Egger A., Sitte W., Bucher E., Oxygen exchange and transport properties of the first-order Ruddlesden-Popper phase $La_2Ni_{0.9}Co_{0.1}O_{4+\delta}$, Solid State Ionics 397 (2023) 116255. https://doi.org/10.1016/j.ssi.2023.116255.

[40] Bucher E., Gspan C., Hofer F., Sitte W., Sulphur poisoning of the SOFC cathode material $La_{0.6}Sr_{0.4}CoO_{3-\delta}$, Solid State Ionics 238 (2013) 15–23. https://doi.org/10.1016/j.ssi.2013.03.007.

[41] Bucher E., Yang M., Sitte W., In situ investigations of the chromium-induced degradation of the oxygen surface exchange kinetics of IT-SOFC cathode materials $La_{0.6}Sr_{0.4}CoO_{3-\delta}$ and $La_{0.58}Sr_{0.4}Co_{0.2}Fe_{0.8}O_{3-\delta}$, Journal of Electrochemical Society 159 (2012) B592–B596. https://doi.org/10.1149/2.027206jes.

[42] Berger C., Bucher E., Egger A., Strasser A.T., Schrödl N., Gspan C., Hofer J., Sitte W., Synthesis and characterization of the novel K_2NiF_4-type oxide $Pr_2Ni_{0.9}Co_{0.1}O_{4+\delta}$, Solid State Ionics 316 (2018) 93–101. https://doi.org/10.1016/j.ssi.2017.12.024.

[43] Tong X:, Zhou F., Yang S., Zhong S., Wei M., Liu Y., Performance and stability of Ruddlesden-Popper $La_2NiO_{4+\delta}$ oxygen electrodes under solid oxide electrolysis cell operation conditions, Ceramics International 43 (2017) 10927–10933. https://doi.org/10.1016/j.ceramint.2017.05.130.

[44] Yan A., Maragou V., Arico A., Cheng M., Tsiakaras P., Investigation of a $Ba_{0.5}Sr_{0.5}Co_{0.8}Fe_{0.2}O_{3-\delta}$ based cathode SOFC II. The effect of CO_2 on the chemical stability, Applied Catalysis B: Environmental 76 (2007) 320–327. https://doi.org/10.1016/j.apcatb.2007.06.010.

[45] Dudley G. J., Steele B.C.H., Theory and practice of a powerful technique for electrochemical investigation of solid solution electrode materials, Journal of Solid State Chemistry 1979 (1980) 233–247.

[46] Dünwald H., Wagner C., Methodik der Messung von Diffusionsgeschwindigkeiten bei Lösungsvorgängen von Gasen in festen Phasen, Zeitschrift für Physikalische Chemie B24 (1934) 53–58.

[47] Mosleh M., Søgaard M., Hendriksen P. V., Kinetics and mechanisms of oxygen surface exchange on $La_{0.6}Sr_{0.4}FeO_{3-\delta}$ thin films, Journal of The Electrochemical Society 156 (2009) B441-B457. https://doi.org/10.1149/1.3062941.

[48] Adler S. B., Factors governing oxygen reduction in solid oxide fuel cell cathodes, Chemical Reviews 104 (2004) 4791–4843. https://doi.org/10.1021/cr020724o.

[49] Bouwmeester H. J. M., Kruidhof H., Burggraaf A. J., Importance of the surface exchange kinetics as a rate limiting step in oxygen permeation through mixed-conducting oxides, Solid State Ionics 72 (1994) 185–194. https://doi.org/10.1016/0167-2738(94)90145-7.

[50] Den Otter M. W., Bouwmeester H. J. M., Boukamp B. A., Verweij H., Reactor flush time correction in relaxation experiments, Journal of Electrochemical Society 148 (2001) J1-J6. https://doi.org/10.1149/1.1337604.

[51] Mougin J., Hydrogen Production by High-Temperature Steam Electrolysis, in: Subramani V., Basile A., Veziroğlu T. N. (Eds.), Compendium of hydrogen energy: Volume 1: Hydrogen production and purification, Woodhead Publishing, Cambridge, UK, 2015, pp. 225–251. https://doi.org/10.1016/C2014-0-02671-8.

[52] Garche J. (Ed.) (Ed.), Encyclopedia of electrochemical power sources, Elsevier Academic Press, Amsterdam, 2009.

[53] Kaur G. (Ed.), Solid oxide fuel cell components, Springer International Publishing, Cham, 2016. https://doi.org/10.1007/978-3-319-25598-9.

[54] Sitte W., Merkle R., High-temperature electrolysis: from fundamentals to applications, IOP Publishing, 2023. https://doi.org/10.1088/978-0-7503-3951-3. 978-0-7503-3951-3.

[55] Macdonald D. D., Reflections on the history of electrochemical impedance spectroscopy, Electrochimica Acta 51 (2006) 1376–1388. https://doi.org/10.1016/j.electacta.2005.02.107.

[56] Barsoukov E., Macdonald J. R., Impedance spectroscopy: theory, experiment, and applications, John Wiley & Sons, Inc., 2018. https://doi.org/10.1002/9781119381860. 9781119074083.

[57] Ruddlesden S. N., Popper P., New compounds of the K_2NiF_4 type, Acta Crystallographica 10 (1957) 538–539. https://doi.org/10.1107/S0365110X57001929.

[58] Ruddlesden S. N., Popper P., The compound $Sr_3Ti_2O_7$ and its structure, Acta Crystallographica 11 (1958) 54–55. https://doi.org/10.1107/S0365110X58000128.

[59] Tarutin A. P., Lyagaeva J. G., Medvedev D. A., Bi L., Yaremchenko A. A., Recent advances in layered $Ln_2NiO_{4+\delta}$ nickelates: fundamentals and prospects of their applications in protonic ceramic fuel and electrolysis cells, Journal of Materials Chemistry A 9 (2021) 154–195. https://doi.org/10.1039/D0TA08132A.

[60] Egger A., Rare earth nickelates as cathodes for solid oxide fuel cells. PhD-thesis. Montanuniversitaet Leoben, Austria, 2013.

[61] Riedel M., Heddrich M. P., Friedrich K. A., Experimental analysis of the co-electrolysis operation under pressurized conditions with a 10 layer SOC stack, Journal of The Electrochemical Society 167 (2020) 24504. https://doi.org/10.1149/1945-7111/ab6820.

[62] Shannon R.D., Revised effective ionic radii and systematic studies of interatomic distances in halides and chalcogenides, Acta Crystallographica A 32 (1976) 751–766. https://doi.org/10.1107/S0567739476001551.

[63] Tamura H., Hayashi A., Ueda Y., Phase diagram of $La_2NiO_{4+\delta}$ ($0 \leq \delta \leq 0.18$), Physica C (1993) 83–88. https://doi.org/10.1016/0921-4534(93)90636-5.

[64] Jorgensen J. D., Dabrowski B., Shiyou P., Richards D. R., Hinks D. G., Structure of the interstitial oxygen defect in $La_2NiO_{4+\delta}$, Physical Review B 40 (1989) 2187–2199. https://doi.org/10.1103/PhysRevB.40.2187.

[65] Aspera S. M., Sakaue M., Wungu T. D. K., Alaydrus M., Linh T. P. T., H. Kasai, M. Nakanishi, T. Ishihara, Analysis of structural and electronic properties of Pr_2NiO_4 through first-principles calculations, Journal of Physics Condensed matter an Institute of Physics journal 24 (2012) 405504. https://doi.org/10.1088/0953-8984/24/40/405504.

[66] Boehm E., Bassat J.-M., Dordor P., Mauvy F., Grenier J.-C., Stevens P., Oxygen diffusion and transport properties in non-stoichiometric $Ln_{2-x}NiO_{4+\delta}$ oxides, Solid State Ionics 176 (2005) 2717–2725. https://doi.org/10.1016/j.ssi.2005.06.033.

[67] Kuterbekov K. A., Bekmyrza K. Zh., Aidarbekov N. K., Nikonov A. V., Pavzderin N. B., Khrustov V. R., Semenova I. V., Medvedev A. I., Gyrdasova O. I., Effect of the cobalt content on properties of $La_2Ni_{1-x}Co_xO_{4+\delta}$, Solid State Ionics 363 (2021) 115594. https://doi.org/10.1016/j.ssi.2021.115594.

[68] Vibhu V., Vinke I. C., Eichel R.-A., Bassat J.-M., de Haart L.G.J. de, Cobalt substituted lanthanide nickelates ($Ln_2Ni_{1-x}Co_xO_{4+\delta}$ Ln = La, Pr; x =0, 0.1, 0.2) as high performance oxygen electrodes for solid oxide cells, Electrochemical Society Transactions 91 (2019) 1327–1339. https://doi.org/10.1149/09101.1327ecst.

[69] Naumovich E. N., Patrakeev M. V., Kharton V. V., Yaremchenko A. A., Logvinovich D. I., Marques F. M. B., Oxygen nonstoichiometry in $La_2Ni(M)O_{4+\delta}$(M = Cu, Co) under oxidizing conditions, Solid State Sciences 7 (2005) 1353–1362. https://doi.org/10.1016/j.solidstatesciences.2005.08.005.

[70] Amow G., Whitfield P. S., Davidson I. J., Hammond R. P., Munnings C. N., Skinner S. J., Structural and sintering characteristics of the $La_2Ni_{1-x}Co_xO_{4+\delta}$ series, Ceramics International 30 (2004) 1635–1639. https://doi.org/10.1016/j.ceramint.2003.12.164.

[71] Bassat J.-M., Odier P., Villesuzanne A., Marin C., Pouchard M., Anisotropic ionic transport properties in $La_2NiO_{4+\delta}$ single crystals, Solid State Ionics 167 (2004) 341–347. https://doi.org/10.1016/j.ssi.2003.12.012.

[72] Wu J., Pramana S. S., Skinner S. J., Kilner J. A., Horsfield A. P., Why Ni is absent from the surface of $La_2NiO_{4+\delta}$?, Journal of Materials Chemistry A 3 (2015) 23760–23767. https://doi.org/10.1039/C5TA03759J.

[73] Skinner S. J., Characterisation of $La_2NiO_{4+\delta}$ using in-situ high temperature neutron powder diffraction, Solid State Sciences 5 (2003) 419–426. https://doi.org/10.1016/S1293-2558(03)00050-5.

[74] Druce J., Téllez H., Burriel M., Sharp M. D., Fawcett L. J., Cook S. N., McPhail D. S., Ishihara T., Brongersma H. H., Kilner J. A., Surface termination and subsurface restructuring of perovskite-based solid oxide electrode materials, Energy & Environmental Science 7 (2014) 3593–3599. https://doi.org/10.1039/C4EE01497A.

[75] Druce J., Ishihara T., Kilner J. A., Surface composition of perovskite-type materials studied by low energy ion scattering (LEIS), Solid State Ionics 262 (2014) 893–896. https://doi.org/10.1016/j.ssi.2013.09.010.

[76] Burriel M., Wilkins S., Hill J. P., Muñoz-Márquez M. A., Brongersma H. H., Kilner J. A., Ryan M. P., Skinner S. J., Absence of Ni on the outer surface of Sr doped La_2NiO_4 single crystals, Energy & Environmental Science 7 (2014) 311–316. https://doi.org/10.1039/C3EE41622D.

[77] Wu K.-T., Téllez H., Druce J., Burriel M., Yang F., McComb D.W., Ishihara T., Kilner J. A., Skinner S. J., Surface chemistry and restructuring in thin-film $La_{n+1}Ni_nO_{3n+1}$ (n = 1, 2 and 3) Ruddlesden–Popper oxides, Journal of Materials Chemistry A 5 (2017) 9003–9013. https://doi.org/10.1039/C7TA01781B.

[78] Bruker AXS Topas V5, General profile and structure analysis software for powder diffraction data: user`s manual, Karlsruhe, Germany, 2014.

[79] Sharma R. K., Cheah S.-K., Burriel M., Dessemond L., Bassat J.-M., Djurado E., Design of $La_{2-x}Pr_xNiO_{4+\delta}$ SOFC cathodes: a compromise between electrochemical performance and thermodynamic stability, Journal of Materials Chemistry A 5 (2017) 1120–1132. https://doi.org/10.1039/C6TA08011A.

[80] Amow G., Whitfield P. S., Davidson L. J., Hammond R. P., Munnings C., Skinner S., Structural and physical property trends of the hyperstoichiometric series, $La_2Ni_{(1-x)}Co_xO_{4+\delta}$, MRS Online Proceedings Library 755 (2003) 347–352. https://doi.org/10.1557/PROC-755-DD8.10.

[81] Rice D. E., Buttrey D. J., An X-ray diffraction study of the oxygen content phase diagram of $La_2NiO_{4+\delta}$, Journal of Solid State Chemistry 105 (1993) 197–210. https://doi.org/10.1006/jssc.1993.1208.

[82] Kharton V. V., Kovalevsky A. V., Avdeev M., Tsipis E. V., Patrakeev M. V., Yaremchenko A. A., Naumovich E. N., Frade J. R., Chemically induced expansion of $La_2NiO_{4+\delta}$-based materials, Chemistry of Materials 19 (2007) 2027–2033. https://doi.org/10.1021/cm070096x.

[83] Amow G., Davidson I., Skinner S., A comparative study of the Ruddlesden-Popper series, $La_{n+1}Ni_nO_{3n+1}$ (n=1, 2 and 3), for solid-oxide fuel-cell cathode applications, Solid State Ionics 177 (2006) 1205–1210. https://doi.org/10.1016/j.ssi.2006.05.005.

[84] Kharton V. V., Yaremchenko A. A., Naumovich E. N., Research on the electrochemistry of oxygen ion conductors in the former Soviet Union. II. Perovskite-related oxides, Journal of Solid State Electrochemistry 3 (1999) 303–326. https://doi.org/10.1007/s100080050161.

[85] Kuhn M., Hashimoto S., Sato K., Yashiro K., Mizusaki J., Oxygen nonstoichiometry, thermo-chemical stability and lattice expansion of $La_{0.6}Sr_{0.4}FeO_{3-\delta}$, Solid State Ionics 195 (2011) 7–15. https://doi.org/10.1016/j.ssi.2011.05.013.

[86] Tietz F., Thermal expansion of SOFC materials, Ionics 5 (1999) 129–139. https://doi.org/10.1007/BF02375916.

[87] Patrakeev M. V., Naumovich E. N., Kharton V. V., Yaremchenko A. A., Tsipis E.V., Nunez P., Frade J.R., Oxygen nonstoichiometry and electron-hole transport in $La_2Ni_{0.9}Co_{0.1}O_{4+\delta}$, Solid State Ionics 176 (2005) 179–188. https://doi.org/10.1016/j.ssi.2004.06.003.

[88] Flura A., Dru S., Nicollet C., Vibhu V., Fourcade S., Lebraud E., Rougier A., Bassat J.-M., Grenier J.-C., Chemical and structural changes in $Ln_2NiO_{4+\delta}$ (Ln=La, Pr or Nd) lanthanide nickelates as a function of oxygen partial pressure at high temperature, Journal of Solid State Chemistry 228 (2015) 189–198. https://doi.org/10.1016/j.jssc.2015.04.029.

[89] Jeon S.-Y., Choi M.-B., Im H.-N., Hwang J.-H., Song S.-J., Oxygen ionic conductivity of $La_2NiO_{4+\delta}$ via interstitial oxygen defect, Journal of Physics and Chemistry of Solids 73 (2012) 656–660. https://doi.org/10.1016/j.jpcs.2012.01.006.

[90] Yaremchenko A. A., Kharton V. V., Patrakeev M. V., Frade J. R., p-Type electronic conductivity, oxygen permeability and stability of $La_2Ni_{0.9}Co_{0.1}O_{4+\delta}$, Journal of Materials Chemistry 13 (2003) 1136–1144. https://doi.org/10.1039/b300357d.

[91] Egger A., Sitte W., Enhanced oxygen surface exchange of $La_2NiO_{4+\delta}$ by means of a thin surface layer of silver, Solid State Ionics 258 (2014) 30–37. https://doi.org/10.1016/j.ssi.2014.01.038.

[92] Munnings C. N., Skinner S., Amow G., Whitfield P., Davidson I. J., Oxygen transport in the $La_2Ni_{1-x}Co_xO_{4+\delta}$ system, Solid State Ionics 176 (2005) 1895–1901. https://doi.org/10.1016/j.ssi.2005.06.002.

[93] Hwang J., Rao R. R., Giordano L., Katayama Y., Yu Y., Shao-Horn Y., Perovskites in catalysis and electrocatalysis, Science (2017) 751–756. https://doi.org/10.1126/science.aam7092.

[94] Badruzzaman A., Yuda A., Ashok A., Kumar A., Recent advances in cobalt based heterogeneous catalysts for oxygen evolution reaction, Inorganica Chimica Acta 511 (2020) 119854. https://doi.org/10.1016/j.ica.2020.119854.

[95] Song J., Ning D., Boukamp B., Bassat J.-M., Bouwmeester H. J. M., Structure, electrical conductivity and oxygen transport properties of Ruddlesden–Popper phases $Ln_{n+1}Ni_nO_{3n+1}$ (Ln = La, Pr and Nd; n = 1, 2 and 3), Journal of Materials Chemistry A 8 (2020) 22206–22221. https://doi.org/10.1039/D0TA06731H.

[96] Shaula A. L., Naumovich E. N., Viskup A. P., Pankov V. V., Kovalevsky A. V., Kharton V. V., Oxygen transport in $La_2NiO_{4+\delta}$: assessment of surface limitations and multilayer membrane architectures, Solid State Ionics 180 (2009) 812–816. https://doi.org/10.1016/j.ssi.2009.01.005.

[97] Egger A., Eisbacher-Lubensky S., Sampl K., Subotić V., Hochenauer C., Sitte W., Bucher E., Pr- and Co-substitution in rare earth nickelates: application as SOEC air electrodes, Fuel Cells 23 (2023) 387–398. https://doi.org/10.1002/fuce.202300037.

[98] Schrödl N., Long-term stability of $Ln_2NiO_{4+\delta}$-type SOFC/SOEC-air electrode materials in the presence of volatile chromium and silicon species. PhD-thesis. Montanuniversitaet Leoben, Austria, 2019.

[99] Townsend A., Pagani L., Scott P. J., Blunt L., Introduction of a surface characterization parameter Sdr_{prime} for analysis of re-entrant features, Journal of Nondestructive Evaluation (2019). https://doi.org/10.1007/s10921-019-0573-x.

[100] Mansour A. N., Nickel monochromated Al Kα XPS spectra from the physical electronics model 5400 spectrometer, Surface Science Spectra 3 (1994) 221–230. https://doi.org/10.1116/1.1247750.

[101] Rojas M. L., Fierro J. L. G., Tejuca L. G., Bell A. T., Preparation and characterization of $LaMn_{1-x}Cu_xO_{3+\lambda}$ perovskite oxides, Journal of Catalysis 124 (1990) 41–51.

[102] Li J. P. H., Zhou X., Pang Y., Zhu L., Vov E. I., Cong L., van Bavel A. P., Li S., Yang Y., Understanding of binding energy calibration in XPS of lanthanum oxide by in situ treatment, Physical Chemistry Chemical Physics 21 (2019) 22351–22358. https://doi.org/10.1039/c9cp04187g.

[103] Howng W.-Y., Thorn R. J., Investigation of the electronic structure of $La_{1-x}(M^{2+})_xCrO_3$, Cr_2O_3 and La_2O_3 by X-ray photoelectron spectroscopy, Journal of Physical Chemistry Solids 41 (1980) 75–81.

[104] Xu X., Chen Y., Zhou W., Zhu Z., Su C., Liu M., Shao Z., A perovskite electrocatalyst for efficient hydrogen evolution reaction, Advanced Materials 28 (2016) 6442–6448. https://doi.org/10.1002/adma.201600005.

[105] Liu C., Chen D., Tang Q., Abuelgasim S., Xu C., Luo J., Zhao Z., Abdalazeez A., Zhang R., Hydrogen-rich syngas production from acetic acid as bio-oil model compound: effect of intermediate phases (La_2NiO_4, La_2O_3 and Ni) of $LaNiO_3$ catalyst, Journal of the Energy Institute 112 (2024) 101492. https://doi.org/10.1016/j.joei.2023.101492.

[106] Luo Y., Wang X., Qian Q., Chen Q., Studies on B sites in Fe-doped $LaNiO_3$ perovskite for SCR of NO_x with H_2, International Journal of Hydrogen Energy 39 (2014) 15836–15843. https://doi.org/10.1016/j.ijhydene.2014.07.135.

[107] Plattner J., Charakterisierung und Optimierung von $La_2Ni_{0.8}Co_{0.2}O_{4+\delta}$ als Luftelektrodenmaterial in Festoxid-Zellen. Master's Thesis. Montanuniversitaet Leoben, Austria, 2023.

[108] Eisbacher S., Egger A., Bucher E., Subotić V., Hochenauer C., Sitte W. (Eds.), $La_2Ni_{0.9}Co_{0.1}O_{4+\delta}$ – a Sr free air electrode with fast oxygen exchange kinetics for SOECs, SOFCs, and RSOCs, 14th European SOFC & SOE Forum B1401 (2020) Lucerne, Switzerland.

[109] Sharma R. K., Djurado E., Functionally graded and homogeneous composites of $La_2NiO_{4+\delta}$ and $La_{n+1}Ni_nO_{3n+1}$ (n = 2 and 3) solid oxide fuel cell cathodes, Journal of Materials Chemistry A 5 (2017) 22277–22287. https://doi.org/10.1039/C7TA06245A.

[110] Williams L., Prasad A. R., Sowmya P., Joseph A., Characterization and temperature dependent dc conductivity study of bio templated nickel oxide nanoparticles (NiO) and their composites using polyaniline (PANI), Materials Chemistry and Physics 242 (2020) 1–6. https://doi.org/10.1016/j.matchemphys.2019.122469.

[111] Uma M., Balaram N., Sekhar Reddy P. R., Janardhanam V., Rajagopal Reddy V., Yun H.-J., Lee S.-N., Choi C.-J., Structural, chemical and electrical properties of Au/La_2O_3/n-GaN MIS junction with a high-k lanthanum oxide insulating layer, Journal of Electronic Materials 48 (2019) 4217–4225. https://doi.org/10.1007/s11664-019-07193-8.

[112] Laguna-Bercero M. A., Monzón H., Larrea A., Orera V. M., Improved stability of reversible solid oxide cells with a nickelate-based oxygen electrode, Journal of Materials Chemistry A 4 (2016) 1446–1453. https://doi.org/10.1039/C5TA08531D.

[113] Virkar A. V., Transport through mixed proton, oxygen ion and electron/hole conductors: analysis of fuel cells and electrolyzer cells using Onsager equations, International Journal of Hydrogen Energy 37 (2012) 12609–12628. https://doi.org/10.1016/j.ijhydene.2012.05.118.

7.2 Tables

7.3 Figures

8 APPENDIX

8.1 Publications

Parts of this thesis were published in the following papers:

Peer-reviewed publications

Paper I

Title: Oxygen exchange and transport properties of the first-order Ruddlesden-Popper phase $La_2Ni_{0.9}Co_{0.1}O_{4+\delta}$

Authors: Sarah Eisbacher-Lubensky, Andreas Egger, Werner Sitte, Edith Bucher

Journal: Solid State Ionics

Year of publication: 2023

DOI: 10.1016/j.ssi.2023.116255

Contribution of the Authors: Sarah Eisbacher-Lubensky: Investigation, Visualization, Validation, Writing - original draft.

Andreas Egger: Investigation, Writing - review & editing.

Werner Sitte: Writing - review & editing.

Edith Bucher: Writing - review & editing.

Paper II

Title: Pr- and Co-substitution in rare earth nickelates: Application as SOEC air electrodes

Authors: Andreas Egger, **Sarah Eisbacher-Lubensky**, Kathrin Sampl, Vanja Subotić, Christoph Hochenauer, Edith Bucher

Journal: Fuel Cells

Year of publication: 2023

DOI: 10.1002/fuce.202300037

Contribution of the Authors: Andreas Egger: Conceptualization, Methodology, Validation, Formal analysis, Investigation, Writing – Original Draft, Visualization

Sarah Eisbacher-Lubensky: Formal analysis, Investigation, Writing – Review and Editing

Kathrin Sampl: Formal analysis, Investigation

Vanja Subotić: Resources, Writing – Review and Editing

Christoph Hochenauer: Resources, Writing – Review and Editing, Funding acquisition

Edith Bucher: Conceptualization, Resources, Writing – Review and Editing, Supervision, Funding acquisition

Non-peer reviewed publication

Proceedings paper (Paper III)

- **Title:** $La_2Ni_{0.9}Co_{0.1}O_{4+\delta}$ - a Sr-free air electrode with fast oxygen exchange kinetics for SOECs, SOFCs, and RSOCs
- **Authors: Sarah Eisbacher**, Andreas Egger, Edith Bucher, Vanja Subotić, Christoph Hochenauer, Werner Sitte
- **Conference:** 14th European SOFC & SOE Forum 2020
- **Year of publication:** 2020

Parts of this thesis were presented at the following conferences:

Oral presentations

14th European SOFC & SOE Forum

- **Title:** $La_2Ni_{0.9}Co_{0.1}O_{4+\delta}$: A Sr-free air electrode with fast oxygen exchange kinetics for SOECs, SOFCs and RSOCs
- **Authors: Sarah Eisbacher-Lubensky**, Andreas Egger, Edith Bucher, Vanja Subotić, Christoph Hochenauer, Werner Sitte
- **Date:** October 20th - October 23rd 2020 in Lucerne (Switzerland)

45th International Conference and Expo on Advanced Ceramics and Composites

- **Title:** Fundamental material properties of the strontium-free SOC air electrode material $La_2Ni_{0.9}Co_{0.1}O_{4+\delta}$
- **Authors: Sarah Eisbacher-Lubensky**, Andreas Egger, Edith Bucher, Werner Sitte
- **Date:** February 9th - February 12th 2021 (virtual conference)

7. GÖCH-Symposium

- **Title:** Oxygen exchange and transport properties of the first-order Ruddlesden-Popper phase $La_2Ni_{0.9}Co_{0.1}O_{4+\delta}$
- **Authors: Sarah Eisbacher-Lubensky**, Andreas Egger, Edith Bucher
- **Date:** September 28th - September 29th 2023 in Vienna (Austria)

Poster presentations

18. Österreichische Chemietage

- **Title:** Synthesis and electrochemical characterization of the first-order Ruddlesden-Popper phase $La_2Ni_{0.9}Co_{0.1}O_{4+\delta}$
- **Authors: Sarah Eisbacher**, Nina Schrödl, Andreas Egger, Edith Bucher, Werner Sitte
- **Date:** September 24th - September 27th 2019 in Linz (Austria)

Spring Meeting of the European Materials Research Society (E-MRS)

- **Title:** Synthesis and fundamental characterization of the first order Ruddlesden-Popper nickelate $La_2Ni_{0.9}Co_{0.1}O_{4+\delta}$
- **Authors: Sarah Eisbacher**, Andreas Egger, Edith Bucher, Werner Sitte
- **Date:** May 31st - June 4th 2021 in Strasbourg (France)

8.2 Declaration of usage of artificial intelligence

Topic	Usage	Tool / Version	Notes
Spelling improvement	6 %	DeepL Write (Beta)	Translation, improving linguistic readability.